Fully Integrated Electronic-Biophotonic System-on-Chip for Real-Time Label-Free Molecular Sensing

Christos Adamopoulos
Vladimir Stojanovic, Ed.

Electrical Engineering and Computer Sciences
University of California, Berkeley

Technical Report No. UCB/EECS-2023-241
http://www2.eecs.berkeley.edu/Pubs/TechRpts/2023/EECS-2023-241.html

December 1, 2023

Fully Integrated Electronic-Biophotonic System-on-Chip for Real-Time Label-Free Molecular Sensing

by

Christos Georgios Adamopoulos

A dissertation submitted in partial satisfaction of the

requirements for the degree of

Doctor of Philosophy

in

Electrical Engineering and Computer Sciences

in the

Graduate Division

of the

University of California, Berkeley

Committee in charge:

Professor Vladimir Stojanovic, Chair
Professor Ali Niknejad
Associate Professor Mekhail Anwar
Professor Panos Patatoukas

Fall 2021

Fully Integrated Electronic-Biophotonic System-on-Chip for Real-Time Label-Free Molecular Sensing

Abstract

Fully Integrated Electronic-Biophotonic System-on-Chip for Real-Time Label-Free Molecular Sensing

by

Christos Georgios Adamopoulos

Doctor of Philosophy in Electrical Engineering and Computer Sciences

University of California, Berkeley

Professor Vladimir Stojanovic, Chair

Label-free miniaturized optical sensors can have a tremendous impact on highly sensitive and scalable Point-of-Care (PoC) diagnostics by monitoring in real-time molecular interactions without any labels. However, current biophotonic platforms are limited by complex optical and external readout equipment, precluding their use in a PoC setting. In this research, we aim to address this challenge by developing a first of its kind fully integrated electronic-photonic real-time label-free molecular sensor utilizing micro-ring resonators (MRRs) co-integrated with on-chip electronics in a high volume advanced electronic process. This technology will reduce cost and enable self-contained and miniaturized Point-of-Care devices that are needed in healthcare applications.

This thesis introduces an arrayed electronic-photonic system-on-chip (EPSoC) in GlobalFoundries (GF) 45nm RFSOI with 60 5µm radius MRRs connected to on-chip receivers, approaching a limit of detection (LoD) equivalent to a single 140nm viral particle. In order to deliver multiple fluidic solutions and enable multi-analyte sensing, we propose an efficient packaging strategy for fabricating multi-channel microfluidic networks interfacing with mm-scale chips. Leveraging co-integration of planar MRRs with on-chip receivers, we eliminate the need for a tunable laser and external readout equipment by shifting the requirements of resonance tuning and readout processing to the electronic domain. To further enhance the LoD we propose a dual-ring phase-based sensing architecture, boosting the system's sensitivity by $3.7x$ compared to intensity-based single MRR schemes. The inherent intrinsic limitations of MRRs due to environmental variations are addressed with an on-chip differential scheme using sensing and reference rings to cancel common mode errors. We demonstrate the sensing capabilities of the EPSoC by monitoring in real-time binding events of proteins and nanoparticles, unlocking the door towards self-contained fully integrated Lab-on-Chip (LoC) photonic sensors for PoC applications.

To my family

Contents

List of Figures

List of Tables

Acknowledgments

During my PhD at Berkeley, I was extremely lucky and fortunate to be surrounded by a great advisor, amazing professors and wonderful colleagues and friends.

I would first like to thank my advisor, Professor Vladimir Stojanovic, for providing me with enormous support and help during my graduate studies and for giving me the opportunity to love research. I would like to thank him for his great technical guidance, his patience and for being a constant source of inspiration to me. Vladimir has not only been an amazing advisor but he is also a role model in life.

I would also like to thank my co-advisors, Professor Mekhail Anwar and Professor Ali Niknejad, for their great guidance during my research. Apart from the very helpful technical discussions we had, I would like to thank them for their valuable advice about research and life in general. Professor Anwar's visionary ideas have inspired my research and kept me motivated every single day in my PhD. Additionally, I was extremely lucky to collaborate with Professor Niknejad. I want to thank him for his generous support throughout my studies and especially during the first years when I needed it the most.

I would also like to thank Professor Patatoukas for the great discussions we've had and for serving on my thesis committee.

A special thanks goes to my undergraduate advisors and mentors in Greece, Professor Paul Sotiriadis and Dr. Iason Vasiliou, who motivated me to apply to Berkeley and work on circuits and systems.

I would like to thank all my labmates in the ISG group for making my PhD a memorable experience. When I joined the group, I was fortunate enough to be mentored by some great researchers and friends. I would like to thank Krishna Settaluri, Sajjad Moazeni, Sen Lin and Taehwan Kim for their patience and for helping me throughout my first tapeouts. Special thanks to Nandish Mehta who is the best and most hard-working analog designer I've met. His help and support during my PhD has really helped me understand the value of research.

I would also like to thank Pavan Bhargava for his significant contribution to all the research projects of this group. His high-impact work has been key to the success of this research and I would like to express my gratitude for always being available to answer any kind of question I had.

The work in this thesis would not be possible without the help of one of my greatest mentors and friends, Sidney Buchbinder. I would like to thank him for the many hours he spent with me on this research and for always being interested and ready to help.

A big thanks also goes to John Wright for his immense help in my first tapeout. I would also like to thank Ali Ameri, Sashank Krishnamurthy, Zhongkai Wang, Matthew Anderson, Sina Alamouti and Meraj Ghanbari for all the great memories we had in BWRC, especially during prelim exam preparation.

During my PhD, I was also fortunate enough to mentor one of the brightest undergraduate students at Berkeley, Asmay Gharia. Asmay has enormously contributed to the success of this project and I would like to thank him for his immense help.

I would also like to thank all the members of the administrative staff in BWRC and EECS department, for their continuous support and assistance. A special thanks goes to Candy Corpus, Mikaela Briggs and Shirley Salanio for their help and patience.

I wish to thank the Greek squad of Berkeley for being like a family to me. Special thanks to Harry Andreadis, Fotis Iliopoulos, Georgios Moschidis, Vrettos Moulos, Georgios Patsakis and Panagiotis Zarkos for all the memories we've had so far and for providing everlasting friendships. They were a continuous source of fun and I will really miss our coffee breaks at Caffe Strada.

A special thanks also goes to Villy Karaly for being a great companion over the last years.

I would like to thank Christos Vezyrtzis for the technical discussions we've had so far and for being a great friend. His experience and valuable advice was a source of motivation for me and made me work harder to accomplish my goals.

I wish to thank my friends in Greece: Spyros Kalyvas, Mikelis Kitromilides, Philip Lazos, Dimitris Kazantzis, Konstantinos Anagnostopoulos, Kostantinos Pappelis, Themis Mavrogordatos and many others. A special thanks goes to Katerina Balta for her great support and for believing in me.

I also want to thank my cousins Areti, Antonis, Panagiotis, Pavlos, my aunt Tania, my uncles Dimitris and Giannis and my grandmother for their love, support and for being an amazing family to me.

I owe my deepest heartfelt gratitude to Benedikt, my sister Ellie and George Kramps for always being there for me and for making me happy everyday. Ellie has always been an inspiration and a role model in my life. Her ability to think outside the box has helped me continue my graduate studies and overcome any obstacle I faced.

Finally and foremost, I want to thank my parents, Marilena and Giorgos, and my sister Ellie, for their endless love and unwavering support throughout my whole life. I want to thank them for their patience and for believing in me. Their unending love always reminds that they will be there for me, no matter what. This work is dedicated to them.

Support: This work was supported in part by the NIH/NHLBI under award number U54HL119893. I also want to thank the Ayar Labs, the BNC at UCB, Santec, and the Berkeley Wireless Research Center for support.

Chapter 1

Introduction

Evanescent field optical sensors based on resonant photonic structures have shown increasing promise in monitoring label-free molecular interactions. However, full integration of the biophotonic sensors together with an on-chip readout and control processing system in a high volume SOI process remains an unmet need. This technology will reduce cost and enable self-contained and miniaturized Point-of-Care devices that are needed in healthcare applications. In this thesis, we aim to address these challenges by introducing a fully integrated electronic-photonic biosensing System-on-Chip (SoC) in a high volume advanced CMOS-SOI process. Taking advantage of co-integration of planar MRRs with on-chip electronics, we eliminate the need for a tunable laser and external readout equipment by shifting the requirements of resonance tuning and readout processing to the electronic domain. At the same time, by combining the inherent sensitivity of MRRs as biosensing devices and integrating multiple rings into a chip-scale array-based architecture, we enable key sensing capabilities in label-free molecular sensing. This paves the path towards miniaturized, highly scalable and portable photonic Lab-on-Chip systems for Point of Care applications. In this introductory chapter, we will first present the main motivation of this research and outline an overview of the thesis contributions.

1.1 Motivation

Immediate and widely accessible Point of Care (PoC) diagnostic technology is the key for halting rapidly and potentially spreading fatal pathogens. A multiparametric, highly scalable, portable and sensitive biosensing platform monitoring complex dynamic molecular parameters will transform our ability to diagnose a disease early and understand its progress by providing accurate, multidimensional and on-demand information on the infection [1, 2]. Current label-based biosensing techniques [3, 4] fall short in 3 key areas: (1) they require well-regulated clinical laboratories, precluding deployment in point-of-care settings, (2) require a time-consuming labeling process delaying results, and (3) capable of measuring only a snapshot in time, they are unable to provide real-time information of molecular interac-

tions such as binding kinetics or dynamic changes in target molecule concentration – key for continuous monitoring of critical parameters in dynamic living systems. Therefore, a label-free sensing approach is critically needed. In this technology, instead of labeling the analyte of interest, we rely on the label-free binding events between the target molecules and their receptors, which induce a change in one of the intrinsic physical properties of the sensing transducer.

In this research we focus on Refractive Index (RI) sensing which has proven to play a key role in various fields, ranging from environmental and water quality monitoring to label-free molecular sensing. By leveraging the small footprint and high sensitivity of optical transducers, RI biophotonic sensors have shown increasing promise over the last decade in monitoring real-time label-free molecular interactions. Optical-based sensing platforms using interferometric devices [5–10] and micro-ring resonators (MRRs) [11–16] have made significant strides towards the label-free detection of molecular concentrations, ranging from µM to the fM regime [11]. However, the passive nature of current platforms cannot provide a compact – ideally on-chip – readout processing system, thus hindering the development of highly portable LoC systems. These limitations result in systems that still heavily rely on complex optics and external readout equipment for precise optical scanning and highly sensitive readout processing, precluding both mass production and miniaturization towards point-of-care (PoC) testing and remaining confined to special laboratory settings [1–3].

In this thesis, we address these challenges by introducing the world's first fully integrated electronic-photonic label-free sensor with nanophotonic micro-ring resonators and electronics on the same chip of a high volume CMOS 45nm advanced electronic process. The deep integration of planar nanophotonic sensors with on-chip electronics unlocks the door towards smart, wholly integrated, scalable and miniaturized lab-on-chip devices capable of capturing the molecular dynamics in real-time, as illustrated in Fig. 1.1.

To overcome the aforementioned limitations of passive photonic systems, we effectively shift the cumbersome requirements for complex optics into the electronic domain by introducing several key innovations:

First, we eliminate the need for a tunable laser by relying on single wavelength schemes enabled by the on-chip electronic control of planar MRRs, therefore allowing co-packaging of simplistic low cost light sources that can ultimately be co-packaged in the same LoC platform. By relying on integrated heaters driven by on-chip electronics and embedded in the design of the ring, we can actively tune the ring's resonance and therefore match it to the single wavelength of a light source without the need to sweep its wavelength. Additionally, the active control of the ring's resonance enables calibration and reset of the MRR back to its nominal resonance, therefore providing a wide dynamic range limited only by the intrinsic saturation of the rings from its full coverage with molecules.

Second, we replace the bulky external readout equipment with on-chip low noise highly sensitive electronic receivers connected to the MRRs. By leveraging the deep integration of circuits with photonics, we design sensitive CMOS receivers to process the optical information once it is converted in the electronic domain through on-chip ring-based photodetectors. The high speed nature of on-chip electronics combined with the single wavelength scheme

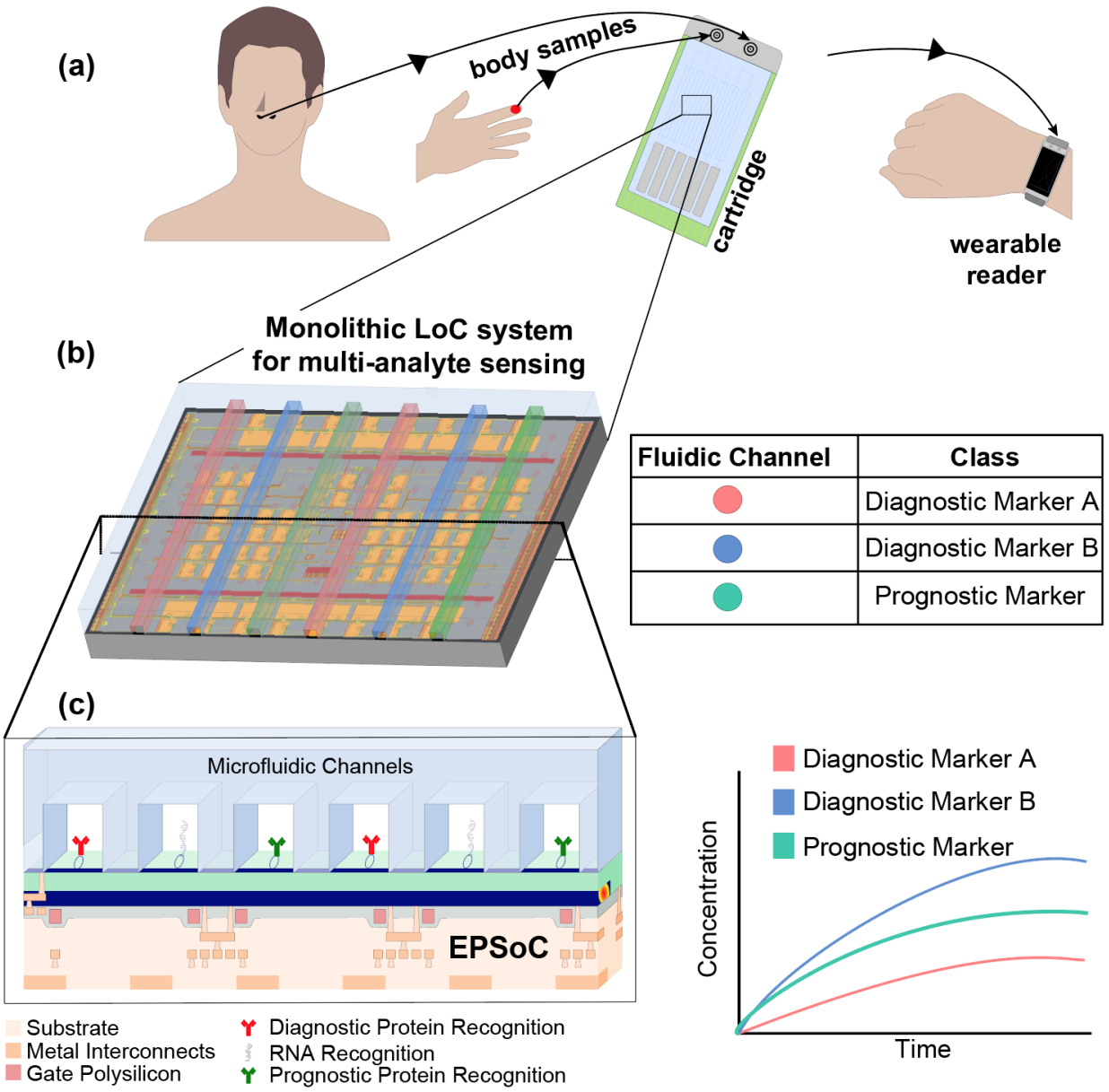

Figure 1.1: Overview of the fully integrated PoC platform for multi-molecular sensing. (a) Body samples are loaded on a cartridge, which plugs into a wearable device. (b) Different molecules run through multiple fluidic channels, co-packaged on a monolithic electronic-photonic Lab-on-Chip system. (c) Each channel of the fluidic network attached to the EPSoC has photonic sensors functionalized with different biorecognition molecules. Multi-analyte detection provides unique fingerprints of disease progression over time.

also offers a unique opportunity to drastically increase the speed of measurement compared to prior work. Multiple data points can be obtained between consecutive binding events – particularly during slow molecular kinetics in the order of seconds – therefore offering the additional advantage of signal averaging which suppresses white noise sources from electronics and photonics and enhances the SNR and sensitivity.

We further enhance the system's sensing performance by introducing various photonic detection schemes using the amplitude and phase information of the ring. To address the inherent limitations of MRRs due to environmental drift, we use an on-chip differential common mode cancellation scheme, comprised of sensing and reference rings. In order to further suppress ambient large RI changes, we implement an on-chip tuning controller that locks the MRR at the desired point of operation.

In this research, by leveraging the deep integration of 10µm MRRs with on-chip receivers, we develop a highly scalable arrayed EPSoC, co-packaged with multi-channel microfluidics for monitoring molecular dynamics. By demonstrating real-time molecular kinetics for the first time in a fully integrated electronic photonic SoC, we unlock the door towards multiplexed real-time biophotonic sensing in a monolithic high volume, commercial and disposable platform.

1.2 Thesis Organization

The remainder of this thesis is organized as follows:

In Chapter 2, we initially provide an overview of the main photonic label-free transducers and discuss their advantages and limitations. The main focus of this research has been on resonant photonic structures and specifically micro-ring resonators (MRRs). We, therefore, first analyze the basic structure of an MRR, introduce its key characteristics and define the photonic sensitivity of the transducer. We then explore and present different MRR-based photonic sensing schemes. These can be categorized into amplitude and phase-based sensing architectures. Starting from the simple topology of single-ring amplitude-based detection, we analyze and optimize the sensitivity of the scheme. We then present phase detection architectures, thus leveraging both the amplitude and phase information of the ring and enhancing the overall sensitivity of the photonic system.

The main bottleneck towards the large-scale commercialization of biophotonic platforms is the need for a tunable laser and off-chip expensive readout equipment. We address this problem by proposing a key breakthrough technology that allows direct integration of photonic resonators with high yield state-of-the-art on-chip electronics. In Chapter 3, we introduce the fully integrated electronic-photonic 45nm RFSOI process and investigate the capability of label-free biosensing in this platform. After describing the process, we characterize and simulate the intrinsic sensitivity of the platform using Lumerical. Preliminary proof-of-concept passive results are then presented for both bulk and molecular sensing, establishing the label-free biosensing performance of the process. Parts of this chapter are presented in the following references:

- Adamopoulos, Christos, et al. "Electronic-Photonic Platform for Label-Free Biophotonic Sensing in Advanced Zero-Change CMOS-SOI Process." CLEO: QELS_Fundamental Science. Optical Society of America, 2019.

One of the challenges in miniaturized photonic-based LoC systems is the simultaneous electronic, photonic and fluidic coupling. Real-time monitoring of various biomarkers requires delivery of multiple fluidic samples to µm-scale ring sensor footprints in mm-scale chips. This creates several challenges in terms of cost and complexity in fabricating miniaturized microfluidic packages with a large number of channels. In Chapter 4, we propose an efficient way of prototyping multi-layer and multi-channel fluidic networks using 3D printed molds. A detailed packaging strategy is demonstrated, ensuring multi-fluidic coupling while allowing electronic and photonic coupling. This work is presented in the following reference:

- Adamopoulos, Christos, et al. "Microfluidic Packaging Integration with Electronic-Photonic Biosensors Using 3D Printed Transfer Molding." Biosensors 10.11 (2020): 177.

In Chapter 5, we introduce a first of its kind fully integrated electronic-biophotonic SoC for real-time, label-free molecular sensing. The key architectural features enabling highly scalable sensing arrays in drastically miniaturized monolithic systems are presented. Integrated heaters and on-chip electronics unlock the door towards single wavelength laser diodes by actively tuning the ring's resonance and at the same time provide a low noise on-chip readout processing system, thus eliminating the need for external equipment. Additionally, different photonic MRR-based architectures provide the capability of multi-analyte sensing by leveraging both the amplitude and phase information of the ring. In this chapter, we provide a detailed analysis of the sensing transducer, readout circuitry and system architecture. The packaging strategy allowing multi-channel electronic-photonic and µ-fluidic coupling is also outlined, focusing on the board design. Finally, the design methodology and top level integration strategy for implementing this complex electronic-photonic system is analyzed. Parts of this chapter are presented in:

- Adamopoulos, Christos, et al. "Fully Integrated Electronic–Photonic Biosensor for Label-Free Real-Time Molecular Sensing in Advanced Zero-Change CMOS-SOI Process." IEEE Solid-State Circuits Letters 4 (2021): 198-201.

- Adamopoulos, Christos, et al. "Lab-on-Chip for Everyone: Introducing an Electronic-Photonic Platform for Multiparametric Biosensing Using Standard CMOS Processes." IEEE Open Journal of the Solid-State Circuits Society (2021).

In Chapter 6, we present the experimental results of the electronic-photonic SoC. First we demonstrate and characterize the electronic performance of the receiver without any light. Next, the electronic-photonic performance is evaluated. The sensitivity of different photonic sensing schemes is measured and the functionality of the on-chip tuning controller

locking the ring's resonance is demonstrated. Additionally, we highlight the significance of the differential sensing scheme suppressing ambient common mode variations and the Limit of Detection is determined. The last part of this chapter presents real-time molecular sensing for the first time in a monolithic electronic-photonic process. The versatility of this biophotonic SoC is demonstrated by detecting binding events of both <10nm proteins and >100nm nanoparticles. This work includes the following references:

- Adamopoulos, Christos, et al. "Fully Integrated Electronic–Photonic Biosensor for Label-Free Real-Time Molecular Sensing in Advanced Zero-Change CMOS-SOI Process." IEEE Solid-State Circuits Letters 4 (2021): 198-201.
- Adamopoulos Christos, et al. "Fully Integrated Electronic-Photonic Biosensor for Label-Free Molecular Sensing in Advanced Zero-Change CMOS-SOI Process," in Conference on Lasers and Electro-Optics, OSA Technical Digest (Optical Society of America, 2021), paper JM4D.3.
- Adamopoulos, Christos, et al. "Fully Integrated Electronic-Photonic Sensor for Label-Free Refractive Index Sensing in Advanced Zero-Change CMOS-SOI Process." 2021 IEEE Custom Integrated Circuits Conference (CICC). IEEE, 2021.

We conclude this thesis by summarizing the key results and outline several paths for improving the sensing performance in next chip generations. Finally, we propose future opportunities and applications using fully integrated electronic-biophotonic SoCs, paving the path towards an implantable vision.

Chapter 2

Label-Free Biosensing with Silicon Photonics

Silicon photonics is an emerging label-free sensing technology offering several advantages in terms of size and sensitivity. Due to its compatibility with CMOS processes, complex chip-scale photonic systems can be fabricated integrating multiple biophotonic sensors for multiplexed sensing. The silicon on insulator technology allows a high confinement of the optical mode. However, the evanescent tail of the electric field interacts with the cladding environment, thus creating a unique opportunity for sensing any RI changes. In this chapter the operating evanescent sensing principle will be presented. Next, an overview of existing label-free optical transducers is provided before focusing on a widely used photonic structure, the micro-ring resonator (MRR). The key design parameters are analyzed and the photonic sensitivity of the ring sensor is optimized. Finally, apart from amplitude-based sensing, we also describe and analyze ring-based phase detection structures. The sensitivity of a Ring-Assisted Mach Zhender Interferometer (RAMZI) is analyzed and phase modulation techniques are presented to further lower the LoD.

2.1 Evanescent Field Sensing

The sensing principle of label-free photonic sensing is based on the evanescent field of the optimal mode propagating through the waveguide. Figure 2.1 illustrates the cross-section of the waveguide.

The waveguide is functionalized with receptor-biorecognition molecules that are specific to the target analytes of interest. The optical mode extends beyond the waveguide boundaries and decays exponentially in the cladding environment within a length of hundreds of nanometers, called evanescent field length. The interaction between the evanescent tail of the optical mode and the target molecules binding to the receptors results in a local change of the RI and a change of the effective index of the optical mode, n_{eff}. Depending on the type of the photonic transducer, this change embedding the molecular binding information

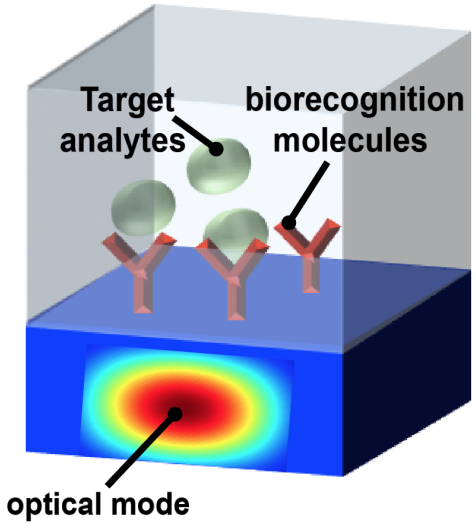

Figure 2.1: Overview of the Evanescent Field sensing principle. Molecular binding events alter locally the RI at the sensing interface, inducing a change of the effective index.

can be translated to other types of signal. As intuitively expected, the less confined the optical mode is inside the waveguide, the stronger the interactions with molecules will be, thus resulting in a larger Δn_{eff}.

2.2 Optical Label-Free Transducers

Advances in label-free nanophotonic molecular sensing have made significant strides, employing a wide range of highly sensitive optical transducers [17–19]. By relying on the evanescent sensing principle of a simple waveguide structure [20, 21], remarkable progress has been achieved to optimize the waveguide geometry tailored towards sensing applications and maximize the sensitivity of different photonic sensing architectures [13, 14, 22]. The goal of evanescent field sensing is to increase the interaction between the optical mode and the target molecules, by propagating a less confined mode inside the waveguide.

Interferometric transducers, which rely on the splitting of the light into two waveguide structures used as the sensing and reference elements, have reported *LoDs* that correspond to <pM molecular concentrations [5–10,23,24], at the cost however of large sensing structures and therefore large chip area. Figure 2.2 illustrates the basic structure of an MZI topology.

Input light of a fixed wavelength is split into two waveguide arms, a sensing and a reference waveguide. The sensing arm is functionalized with receptors while the reference arm introduces a reference phase offset. The electric fields of the two waveguides are then recombined and an output intensity is produced, given by the following expression:

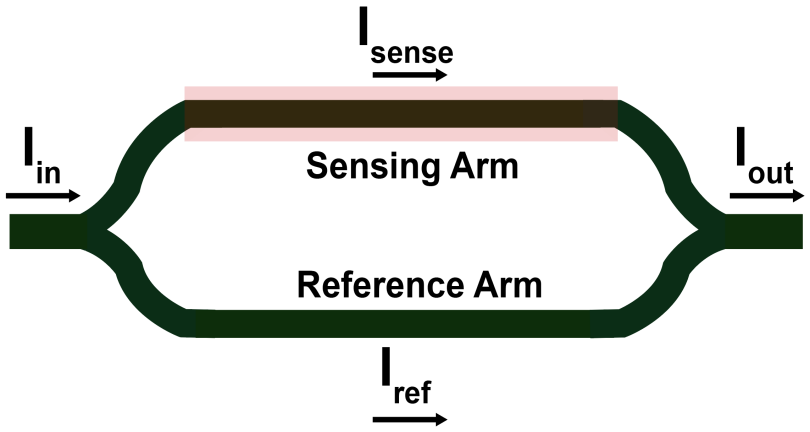

Figure 2.2: MZI Structure.

$$I_{out} = I_{sense} + I_{ref} + 2I_{sense}I_{ref}cos(\delta\phi_{sense} + \phi_{offset}), \tag{2.1}$$

where I_{sense} and I_{offset} is the light intensity of the sensing and reference waveguide respectively, $\delta\phi_{sense}$ is the phase difference between the two arms induced from molecular binding and ϕ_{offset} is a phase offset from any imbalance between the two arms. The change of the effective index induced from molecular binding events in the sensing arm is translated into a phase change $\delta\phi_{sense}$, given by:

$$\delta\phi_{sense} = \frac{2\pi\Delta n_{eff}L}{\lambda_o}, \tag{2.2}$$

where L is the waveguide's length and λ_o is the light's wavelength. This indicates the dependence of sensitivity on the waveguide's length, thus requiring large footprints and complicating the capability of multiplexed biosensing using scalable arrays of multiple sensors. Additionally, the sinusoidal nature of the output response requires operation at the quadrature point to maximize sensitivity.

The dependence of sensitivity on the waveguide's length can be circumvented through the use of resonant-based sensors which rely instead on the sharpness of their resonant spectrum expressed by the quality factor Q of the transducer [25]. The quality factor of a resonator represents the number of roundtrips a photon undergoes within the resonant cavity before it is lost to the surrounding medium. Therefore, resonators with large quality factors demonstrate a sharper resonant spectrum and thus increased sensitivity. Additionally, their small footprint, enables the design of multiple highly compact miniaturized resonant sensors on the same chip, creating highly scalable arrays for multiplexed sensing.

Numerous resonant-based biosensors have been introduced over the last years monitoring real-time molecular kinetics [26], [12], [11], [13, 14, 16, 22, 27, 28]. Advancements in both the ring waveguide geometry as well as the photonic platforms have significantly pushed

the boundaries of the limit of detection and have paved the path towards ultra sensitive molecular detection. By combining more sensitive waveguide structures, sub-wavelength and slot waveguide MRR devices have been demonstrated [13, 14, 22], achieving a larger intrinsic sensitivity at the cost, however, of a lower quality factor.

Despite the significant promise of these efforts, most of the focus has been on optimizing the sensitivity of the optical structures resulting in complex optics – in some occasions non planar [26] – therefore precluding their fabrication in a high volume commercial process.

The prior work on resonant sensing devices relies on sweeping a bulky tunable light source interrogating the resonant photonic sensors, therefore setting a limit on the speed of the measurement which is restricted by the sweeping rate of the laser. Additionally, another major bottleneck towards the large scale commercialization of passive photonic platforms is the need for an off-chip bulky readout equipment processing the optical information, therefore precluding miniaturization of the LoC platform.

2.3 MRR-based Label-Free Sensing

MRRs have been the driving force of Silicon Photonic-based label-free sensing. The basic structure of a ring resonator is illustrated in Fig. 2.3 and is comprised of a bus waveguide coupled to a circular waveguide. When the wavelength of the input light is such that the round-trip phase shift accumulated around the ring is an integer multiple of 2π, the ring is said to be on resonance. In this condition, destructive interference occurs at the thru-port of the ring, and the power circulating inside the ring is maximized [25]. At off-resonant wavelengths, more power is transmitted to the thru port, resulting in the Lorentzian shaped transmission spectrum of Fig. 2.4.

MRR-based sensors detect the modulation of their resonant wavelength induced from molecular binding events. Key for this modulation is the interaction between the evanescent tail of the optical mode and molecules, which in turn results in a change of the effective index, Δn_{eff}. In label-free biosensing, molecular binding events on the functionalized chip surface alter locally the RI at the sensing interface and manifest as a change in the effective index n_{eff} of the mode, which depends on the RI of the surrounding materials.

Since a micro-ring is on resonance when its optical round-trip length is equal to an integer multiple of the light's wavelength, we can write:

$$\lambda_{res} = \frac{n_{eff} L}{m}, \tag{2.3}$$

where n_{eff} is the effective index of the mode, L is the ring circumference and m is the resonance order, which represents the integer number of times the wavelength fits in the optical round trip length $n_{eff}L$.

The ring spectrum consists of multiple resonances separated by a wavelength pitch, defined as Free Spectral Range (FSR). This wavelength spacing between consecutive resonances is inversely proportional to the ring's circumference. FSR can be written as:

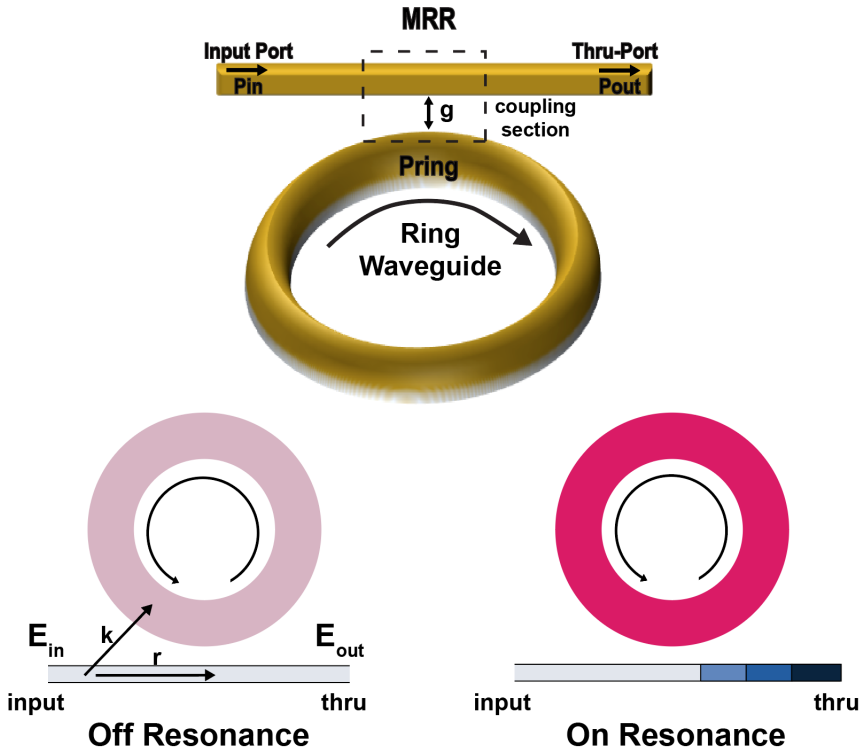

Figure 2.3: A MRR consists of a bus coupled to a looped waveguide. The ring can be on or off resonance depending on the ratio of the wavelength λ to the optical round trip length $n_{eff}L$.

$$FSR = \frac{{\lambda_{res}}^2}{n_g L}, \tag{2.4}$$

where group dispersion is taken into account through the group index, n_g. In all prior work, where a tunable laser sweeps across the whole Lorentzian spectrum to capture the shift, the dynamic range is limited by the resonant spacing of the FSR.

The thru port transfer function of an MRR can be defined as the ratio of the transmitted to the incident field of the bus waveguide [25]. It can be derived as:

$$t = \frac{E_{out}}{E_{in}} = e^{i(\pi+\theta)} \frac{a - re^{-i\theta}}{1 - rae^{i\theta}}, \tag{2.5}$$

where r is the self coupling coefficient of the ring, $\theta = \frac{2\pi}{\lambda_o} n_{eff} L$ is the round trip phase offset at a laser's wavelength λ_o, and $a = e^{\frac{-a_{\text{pow}} L}{2}}$ is the single-pass amplitude transmission, where a_{pow} is the power attenuation coefficient. By squaring eq. (2.5), the power transmission T_n can be given by:

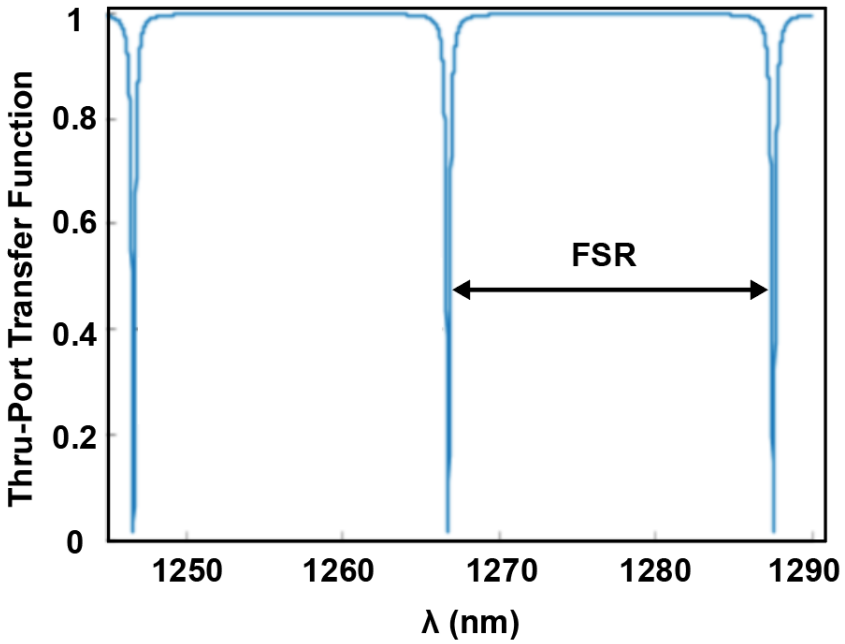

Figure 2.4: The spectrum of a MRR consists of multiple resonances separated by the Free Spectral Range (FSR).

$$T_n = t^2 = \frac{a^2 - 2arcos(\theta) + r^2}{1 - 2arcos(\theta) + (ar)^2}. \tag{2.6}$$

The sensitivity of a MRR depends on the slope of its Lorentzian spectrum, described by the quality factor Q. The larger the quality factor of the ring is the longer the lifetime of the photon will be, resulting in stronger interactions with the cladding environment. Translating its physical meaning into the spectrum domain, a large Q corresponds to a steeper Lorentzian shape.

Quality factor Q is expressed as the ratio of the resonant wavelength λ_{res} to the MRR's Full Width at Half Maximum ($FWHM$), which represents the bandwidth of the ring, as shown in Fig. 2.5. Therefore, we can write:

$$FWHM = \frac{(1-ar){\lambda_{res}}^2}{\pi n_g L\sqrt{ar}}; Q = \frac{\lambda_{res}}{FWHM} = \frac{\pi n_g L\sqrt{ar}}{(1-ar)\lambda_{res}}. \tag{2.7}$$

From eq. (2.7), we understand that Q scales linearly with the ring radius as long as the propagation losses are not dominating. The spectrum in Fig. 2.5 shows a ring at critical coupling. During this condition, the coupled power ($\sqrt{1-r^2}P_{in}$) is equal to the power loss inside the ring. At critical coupling, the power at the thru port is zero. For a self coupling coefficient $r < a$ the ring is overcoupled, whereas for $r > a$ the ring is in the undercoupled

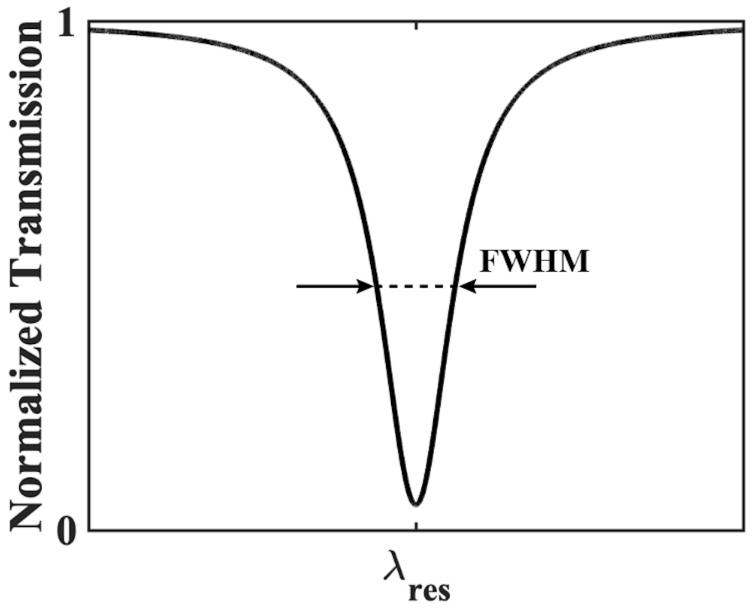

Figure 2.5: The quality factor Q of a ring affects the slope of the resonance shape.

regime. A more detailed analysis for optimizing the MRR's sensitivity will be derived in the next section.

The resonance shape has a strong impact on the MRR's sensitivity. In contrast to a low Q MRR, a wavelength shift in a higher Q ring results in a larger variation of the transmission coefficient at a fixed wavelength and a larger power fluctuation at the thru port and the ring waveguide. However, in order to estimate the overall sensitivity of the photonic transducer, we also need to take into account the intrinsic sensitivity of the process, which relates the wavelength shift to the environmental variation of interest. Therefore, two different types of sensitivities can be defined. First, using eq. (2.3) and taking into account dispersion [29] the intrinsic sensitivity can be given by:

$$S_{int} = \frac{\partial \lambda}{\partial X} = \frac{\partial n_{eff}}{\partial X} \frac{\lambda_{res}}{n_g}, \tag{2.8}$$

where X represents a molecular binding event. This type of sensitivity describes the amount of wavelength shift $\Delta\lambda$ in a MRR that results from a single molecule binding on the surface of the ring. This event affects the effective index n_{eff} of the ring's waveguide, which in turn results to a wavelength shift. The intrinsic sensitivity of the platform can be characterized using optical mode simulations, as shown in Chapter 3.

With the MRR operating at a fixed input wavelength, any resonant shift results in a power fluctuation in the looped and bus waveguides respectively, as shown in Fig. 2.6b. For intensity detection sensing schemes, we define a photonic sensitivity metric, S_{phot}, as the

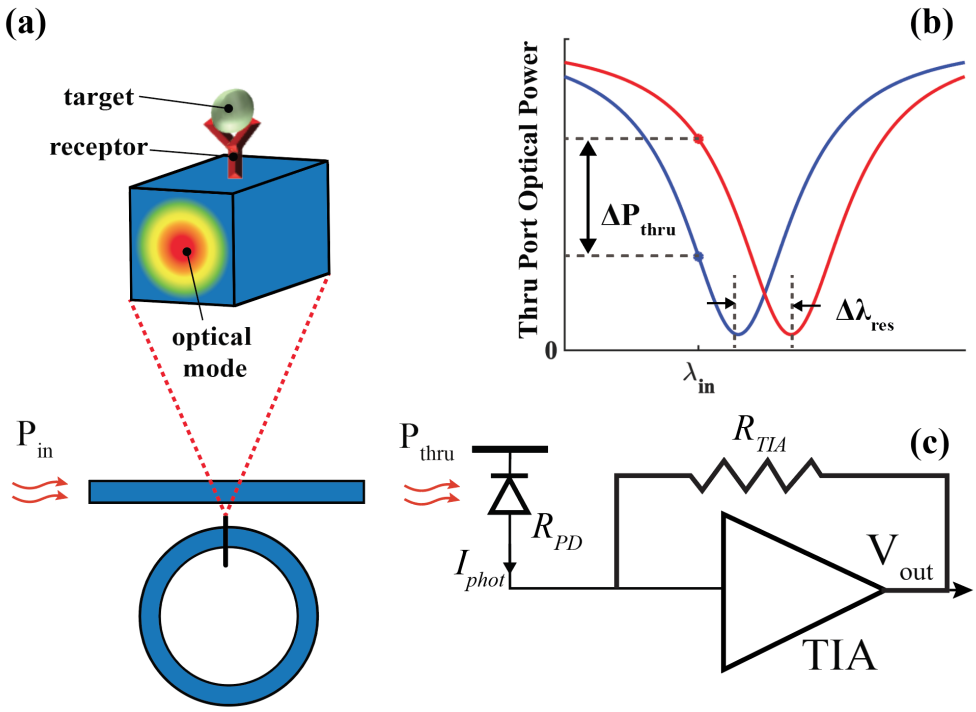

Figure 2.6: Sensing principle of operation in MRR-based systems: (a) Molecular binding events alter the confinement of the optical mode propagating in the Si waveguide, inducing a change in the effective index, Δn_{eff}. (b) Δn_{eff} results in a resonant shift of the ring, $\Delta\lambda_{res}$. Operating at fixed wavelength, λ_o, the shift in resonance induces a fluctuation in the transmitted optical power, ΔP_{thru} . (c) A photodetector and a TIA convert the optical signal to the electronic domain.

amount of change in the transmitted optical power per induced resonant shift:

$$S_{phot} = \frac{\partial P_{thru}}{\partial \lambda_{res}} \approx P_{thru}\frac{1}{FWHM} = P_{thru}\frac{Q}{\lambda_{res}}, \tag{2.9}$$

where P_{thru} is the transmitted optical power, Q is the quality factor of the micro-ring resonator, and we have assumed full extinction (i.e. critical coupling) and operation around a linear region close to the maximum slope point. As intuitively expected, resonators with lower losses and hence higher quality factors have proportionately higher photonic sensitivity.

Finally, in order to process the optical sensing signal, a photodetector with responsivity R_{PD}, and a transimpedance amplifier (TIA) with gain R_{TIA} convert the optical information into the electrical domain, as illustrated in Fig. 2.6c.

The *total sensitivity*, S_{tot} of this transduction chain can be defined as:

$$S_{tot} = \frac{\partial V_{out}}{\partial X} = \frac{\partial \lambda_{res}}{\partial X}\frac{\partial P_{thru}}{\partial \lambda_{res}} R_{PD} R_{TIA} \approx S_{int} S_{phot} R_{PD} R_{TIA}. \tag{2.10}$$

One of the most critical Figures of Merit (FoM) in a biosensor is the Limit of Detection (LoD), which describes the minimum measurable quantity that can be detected by the transducer. This sensitivity analysis combined with the noise limitations will determine the LoD of the system.

The LoD depends on the minimum resolvable wavelength shift and the overall sensitivity, previously defined. In order to define an LoD that does not depend on the measurement setup, it can be assumed that the minimum resolvable wavelength shift is equal to the $FWHM$ of the ring. A ring with a large quality factor has a smaller $FWHM$, and thus a smaller minimum resolvable shift. This simplified description of the LoD can written as:

$$LoD = \frac{FWHM}{S_{int}} = \frac{\lambda_{res}}{QS_{int}}. \tag{2.11}$$

It can be observed that a boost in the LoD is achieved by increasing S_{int}. One way to do this is by further exposing the evanescent field in the cladding environment [30]. Additionally, utilization of high quality factor MRRs is another knob that can enhance the LoD through S_{phot}. A sharper resonant slope creates a larger fluctuation in the transmitted or circulating power of the ring for a given resonant wavelength shift, thus resulting in a smaller minimum resolvable wavelength shift. However, the designer must be aware to not adversely impact the intrinsic sensitivity, while striving to increase Q.

2.4 MRR-based Sensing Architectures

A number of publications have proposed label-free biophotonic sensing based on resonant photonic structures. However, all of these techniques utilize passive photonic chips and devices and rely on complex external equipment and tunable lasers for precise optical optical spectrum scanning. This in turn limits the rate and accuracy at which measurements can be taken, and leaves the Q-factor of the photonic device as the only parameter through which a higher fidelity resolution can be achieved - striving towards a single molecule binding event detection. Optical spectrum curve fitting is used to enhance the resolution allowing a minimum resolvable wavelength lower than the linewidth of the laser source. The dynamic range of this interrogation scheme is equal to the FSR of the ring.

Specifically, the tunable laser technique listed in prior work, performs multiple scans of the whole thru-port transfer function and uses least-squares fitting to estimate the amount of wavelength shift and therefore the change in index of refraction and the rate of molecular binding. Due to limited speed of the tunable lasers, these techniques take minutes to perform a single estimation, and cannot perform a lot of averaging due to a limited number of data points that can be acquired in that time interval. As such, the method solely relies on the Q factor of the resonator and the intrinsic sensitivity as the means to improving the fidelity of the measurement. With Q factors of less than 100,000, these systems have a resolution several orders of magnitude coarser than needed for single molecule detection. Second, the

system has a narrow dynamic range since the sensitivity is tied to the scanning time, while the concentration of the target molecules determines the binding rate.

An alternative method of detecting molecular binding events is achieved by monitoring the optical power circulating inside the ring waveguide at a fixed wavelength λ_o, opening the door to low cost, single wavelength laser diodes. Operating at a fixed bias point of the Lorentzian spectrum, the MRR's resonant shift decreases the power circulating inside the ring waveguide, creating an amplitude and phase change of the MRR's electric field, indicative of the amount of resonant shift, as illustrated in Fig. 2.6b. Additionally, fixed wavelength schemes eliminate the need for sweeping the Lorentzian spectrum of the ring and thus accelerate the measurement speed by sampling multiple measurement points in a given time frame. This capability offers the advantage of significant post-averaging, therefore enhancing the SNR by mitigating the effect of white noise sources.

In the following sections, intensity and phase MRR-based sensing architectures will be reviewed and analyzed in terms of their sensitivity. Starting from the intensity-based single MRR sensing scheme, the normalized photonic sensitivity will be optimized. In order to leverage the phase information of the ring, phase detection architectures will be introduced and compared to the single-MRR scheme.

2.4.1 Intensity Detection

Monitoring the intensity fluctuations, induced by a resonant shift at a fixed wavelength, eliminates the need for a tunable laser and enables the use of more simplistic light sources. Additionally, it accelerates the measurement speed by collecting multiple measurements within a given fixed time frame.

As described in previous sections, any molecular interactions occurring at the top of the sensor result in a change of the effective index n_{eff} of the mode and a resonant shift, $\Delta\lambda$. This wavelength shift leads to a power fluctuation at the thru port of the MRR. At the same time, the change of the effective index creates a change in the round trip phase offset θ of the electric field inside the ring waveguide.

In order to evaluate the sensitivity of a single MRR, we examine the scenario of monitoring the power fluctuations at the thru port of the ring. From eq. (2.6) the output power is given by:

$$P_{out} = T_n P_{in} = t^2 P_{in} = \frac{a^2 - 2arcos(\theta) + r^2}{1 - 2arcos(\theta) + (ar)^2} P_{in}. \tag{2.12}$$

A change in the n_{eff} results in a round trip phase change $\delta\theta$. By taking the derivative of P_{out} in terms of θ and normalizing it to the input power P_{in}, the normalized sensitivity S_{norm} of a single MRR can be written as:

$$S_{norm} = \frac{\partial P_{out}}{\partial \theta P_{in}} = 2t\frac{\partial t}{\partial \theta}. \tag{2.13}$$

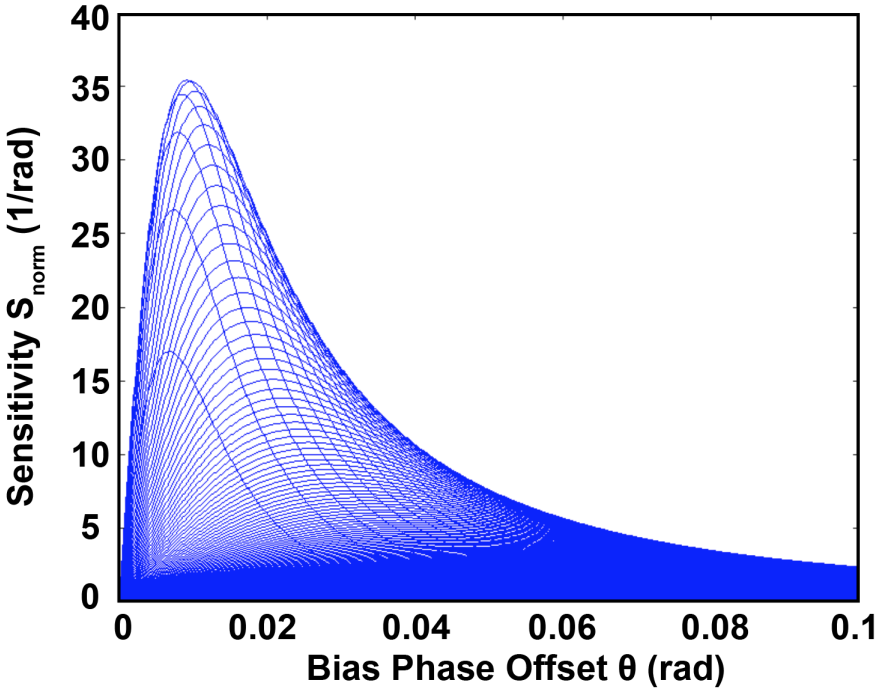

Figure 2.7: Normalized sensitivity of a single ring for a varying bias phase offset θ and self coupling coefficient r.

The slope of the Lorentzian depends on the self coupling coefficient r and the bias point θ at which the MRR is operating. Having these two design parameters as tuning knobs, the resonant shape can be optimized by maximizing the slope for the optimal θ and r.

A numerical evaluation of the normalized sensitivity is implemented. In this analysis, the power attenuation coefficient is assumed to be 3.45 $\frac{1}{cm}$. As a first step, the self coupling coefficient of the ring is swept over a wide range covering all coupling modes of the MRR. Figure 2.7 illustrates the normalized sensitivity *vs* θ for self coupling coefficient values ranging from 0.7 to 0.99. Each curve corresponds to a different value of self coupling coefficient r. The optimal bias point corresponds to approximately 10mrad off-resonance round trip phase offset. For this $\theta_{optimal}$, r is swept again in the range of $[0.7 - 0.99]$, as shown in Fig. 2.9. The maximum sensitivity is obtained for a value of $r > r_{critical}$ which indicates that optimal operation of the ring occurs in the undercoupled regime. However, this direct intensity detection scheme does not employ any phase information of the electric field at the output port of the MRR.

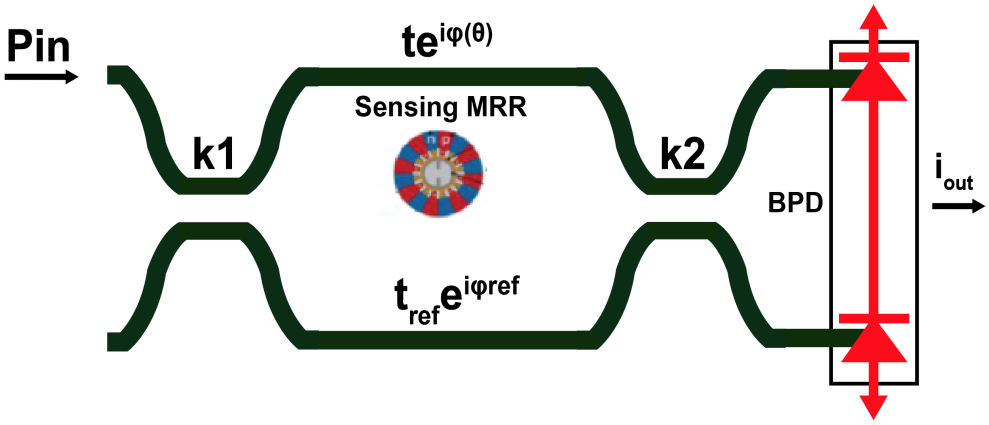

Figure 2.8: A Ring Assisted Mach Zhender Interferometer.

2.4.2 RAMZI Phase Detection

A resonant shift induced from molecular binding events results in a change in the amplitude and phase of the electric field of the MRR. Detecting phase instead of amplitude has received increased interest over the last decade due to its superior sensitivity compared to intensity based schemes [31–33]. Here, we describe the operation of Ring Assisted Mach Zhender Interferometer (RAMZI), shown in Fig. 2.8, and compare its sensing performance with a single MRR scheme.

Light of wavelength λ is coupled into the input port of the device and is split by a coupler with a power coupling ratio k_1 into a sensing and a reference arm. The sensing arm consists of a MRR exposed to the environmental changes while the reference arm is used for offset calibration. The two arms are then recombined by a second coupler of a splitting ratio k_2. P_3 and P_4 is the power at the output ports of the coupler. In this scheme, the power difference dP_{out} is detected. This is achieved by using a Balanced Photodetector (BPD) configuration, shown in Fig. 2.8. where the output current signal is proportional to the power difference $P_3 - P_4$, which depends on both the amplitude and phase slope of the output electric field of the MRR.

In order to analyze the performance of the RAMZI, the sensitivity needs first to be defined and optimized similarly to a single ring. Based on the analysis from [33] the sensitivity S_{norm} normalized to the input power P_{in} is given by:

$$S_{norm} = -(4Acos(\phi_{ref} - \phi(\theta)) + 2Bt(\theta))t'(\theta) - 4Asin(\phi_{ref} - \phi(\theta))t(\theta)\phi'(\theta) \quad (2.14)$$

$$A = \sqrt{k_1 k_2 (1-k_1)(1-k_2)} \quad (2.15)$$

$$B = k_1 + 2k_2 - 2k_1 k_2 - 1, \quad (2.16)$$

where θ is the ring's round trip phase shift, $\phi(\theta)$ is the output phase transfer function of the

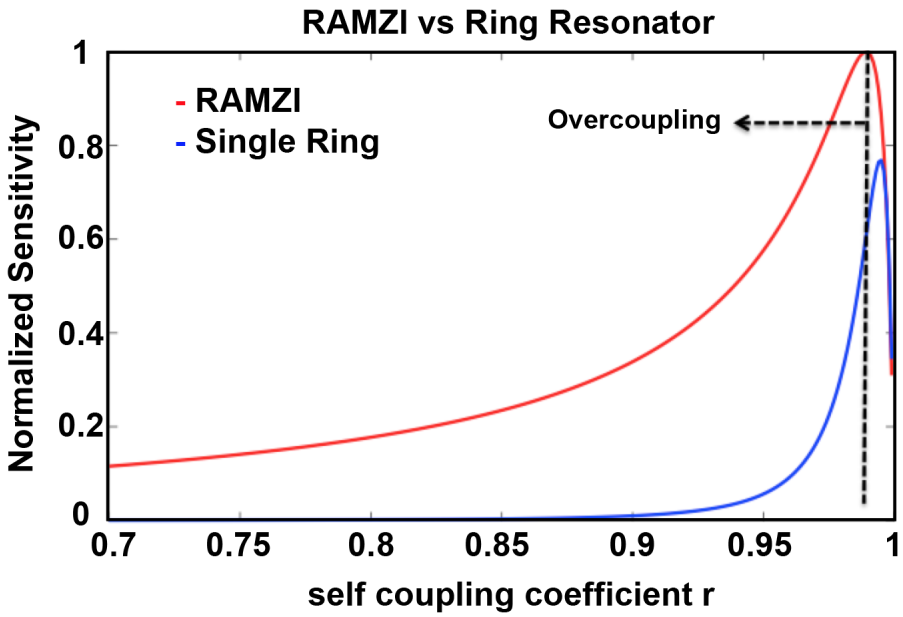

Figure 2.9: Normalized sensitivity for a varying self coupling coefficient r of a ring and a RAMZI at their optimal bias point θ_{opt}.

ring and ϕ_{ref} is the offset phase shift from the reference arm. The amplitude coefficient t_{ref} of the reference waveguide is assumed to be equal to 1.

Optimization of the RAMZI structure includes more tuning knobs compared to a single MRR. First, the power splitting ratio of the input and output coupler can be optimized. By taking the derivative of S_{norm} in terms of k_1 and k_2 the optimal splitting ratio can be found to be $k_1 = k_2 = 0.5$ [33]. In order to maximize S_{norm}, we need to optimize for θ and r. Both design parameters are swept in a wide range similar to the single ring analysis. First, the optimal bias phase point is determined by sweeping θ for different values of r. The maximum absolute sensitivity is found to be on resonance. For that bias point, the self coupling coefficient is then swept in the same range of $[0.7 : 0.999]$. Fig. 2.9 presents the optimized normalized sensitivity of a single ring and a RAMZI. It can be observed that for a RAMZI structure the optimal slope occurs on resonance at critical coupling ($r = r_{critical}$), whereas for a ring the maximum sensitivity is found to be in the undercoupling region. In the overcoupling regime, the RAMZI structure can be much more sensitive than a single MRR [33].

2.4.3 Phase Modulation Techniques

RAMZI-based structures produce a low frequency intensity-based signal at the output, embedding both amplitude and phase information of the MRR. In order to mitigate the effect

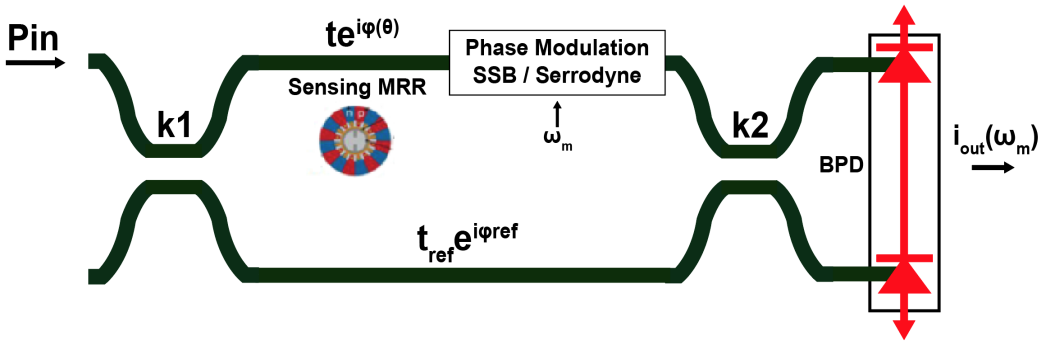

Figure 2.10: RAMZI structure combined with phase modulation. Elimination of one of the sidebands using an SSB or a serrodyne modulation scheme results in a phase modulated photocurrent, thus mitigating the effect of low frequency electronic noise.

of low frequency noise sources and enhance the overall sensing performance, two phase modulation techniques are presented.

As shown in Fig. 2.10, light of wavelength λ entering the sensing arm is first phase shifted from a sensing MRR due to the targeted molecular interactions. The electric field is then phase modulated by an SSB (Single Sideband) or a Serrodyne modulator. Both of these architectures eliminate one sideband allowing a phase-modulated photocurrent after the balanced photodetector. The nature of this signal ensures higher robustness to any power fluctuations of the laser or mechanical vibrations in the fiber to chip interface. At the same time, modulating the electric field allows low frequency noise suppression, thus mitigating the effect of low frequency noise.

Figure 2.11 shows the basic architecture of an SSB modulator. It consists of two nested Mach Zhender Modulators (MZM), driven by two orthogonally ($\Delta\phi = \frac{\pi}{2}$) sine waves. The modulated electric field at the output of the upper MZM is given by:

$$E_A = \frac{E_{in}}{\sqrt{2}} e^{\frac{2\pi n_0 L_{arm}}{\lambda}} cos(\frac{\pi S}{S_\pi} cos(\omega_m t)) cos(\omega_0 t), \tag{2.17}$$

where S is the modulation signal, L_{arm} is the length of the Mach Zhender Modulator's (MZM) arm, n_0 is the nominal effective index of the waveguide without any modulation, ω_m and ω_0 are the modulation and carrier frequency respectively and S_π is the signal needed for a π phase shift. It should be noted that depending on the type of modulation, the driving signal S can take various forms. As an example, we can consider two different types of modulation, electro-optic and thermo-optic. In the first case, a voltage changes n_{eff} based on the electro-optic effect [34], whereas in thermo-optic modulation the power P_{heat} heating the waveguide modulates n_{eff} based on the thermo-optic coefficient of the materials. Assuming that a first order approximation of the effective index is given by $n_{eff} = n_0 + pS$, where p is the modulation efficiency, S_π can be derived as follows:

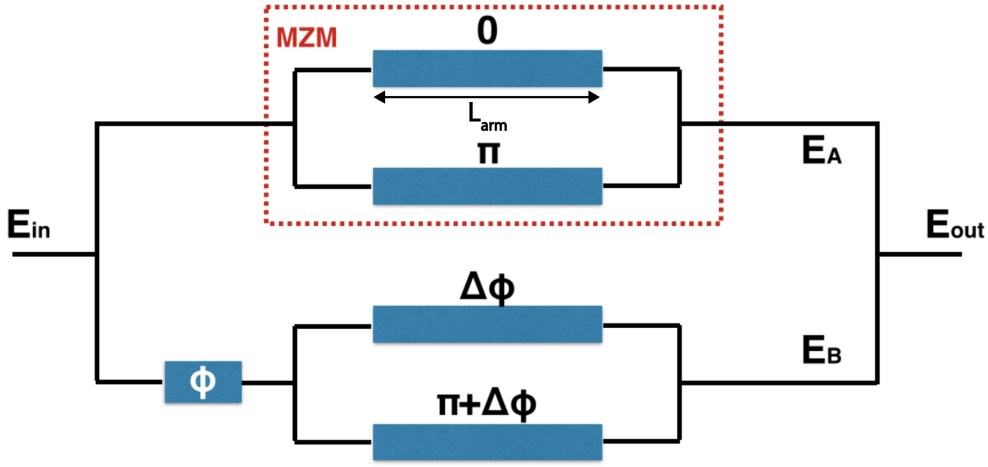

Figure 2.11: A Single Sideband Modulator.

$$S_\pi = \frac{\lambda}{2pL_{arm}}. \tag{2.18}$$

If the modulation signal S consists of a dc and an ac component we can write:

$$S = S_{dc} + s_{am}cos(\omega_m t) \tag{2.19}$$

$$E_A = \frac{E_{in}}{\sqrt{2}}cos(\frac{\pi S_{dc}}{S_\pi} + \frac{\pi s_{am}}{S_\pi}cos(\omega_m t))cos(\omega_0 t + \frac{2\pi n_0 L_{arm}}{\lambda}) \tag{2.20}$$

$$E_B = \frac{E_{in}}{\sqrt{2}}cos(\frac{\pi S_{dc}}{S_\pi} + \frac{\pi s_{am}}{S_\pi}cos(\omega_m t + \Delta\phi))cos(\omega_0 t + \frac{2\pi n_0 L_{arm}}{\lambda} + \phi), \tag{2.21}$$

where $\Delta\phi = \frac{\pi}{2}$ since the two MZMs are driven orthogonally and ϕ is the phase offset in the bottom arm of the SSB. By combining the output fields E_A and E_B we can derive the following expression for the output field E_{out}:

$$\begin{aligned} E_{out} = {} & \frac{E_{in}}{2}J_1(\frac{\pi s_{am}}{S_\pi})(cos(\omega_m t)cos(\omega_0 t + \frac{2\pi n_0 L_{arm}}{\lambda}) \\ & + cos(\omega_m t + \Delta\phi)cos(\omega_0 t + \frac{2\pi n_0 L_{arm}}{\lambda} + \phi)) + \text{higher order terms}, \end{aligned} \tag{2.22}$$

where J_1 is the 1^{st} order Bessel function and E_{in} is the input electric field. If the phase offset ϕ in the bottom arm is $\frac{\pi}{2}$ or $-\frac{\pi}{2}$ then one of the two sidebands, $\omega_0 + \omega_m$ or $\omega_0 + \omega_m$ is eliminated. The output photocurrent i_{out} after the balanced photodetector of Fig. 2.10 is then given by:

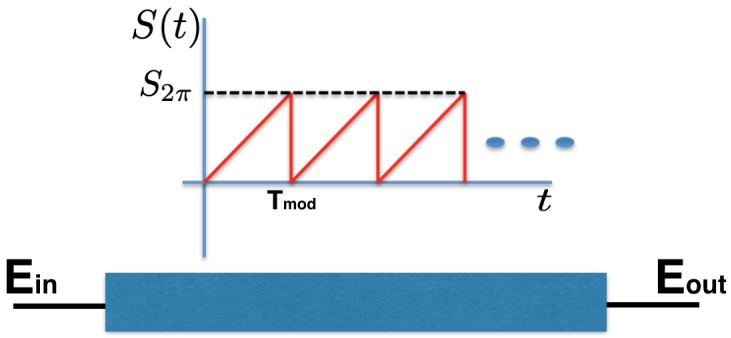

Figure 2.12: A Serrodyne Modulator driven by a sawtooth waveform with a peak value of $S_{2\pi}$.

$$i_{out} = R_{PD}P_{in}f(k_1, k_2)cos(\omega_m t + \delta\phi_{sense} + \phi_{offset}), \tag{2.23}$$

where R_{PD} is the responsivity of the balanced PD, $f(k_1, k_2)$ is a function of the input and output coupler splitting ratio, $\delta\phi_{sense}$ and ϕ_{offset} are the sensing and offset phase shifts respectively and P_{in} is the laser's input power. As we can observe, the detected current signal is a phase modulated current that embeds the phase changes from the molecular interactions inside the phase of the sinewave. This is achieved from the SSB by eliminating one of the sidebands. One of the main characteristics of an ideal SSB is the perfect cancellation of one sideband regardless of the modulation depth of the MZMs. However, several non-idealities depending on the modulation scheme (AM-PM distortion in electro-optic modulation) can degrade the SR. One of the main disadvantages of an SSB scheme is the increased harmonic power for decreasing modulation depth resulting to a large insertion loss. Let h_i be the harmonic power of the i^{th} tone, $\omega_0 + i\omega_m$. Based on the Bessel expansion analysis, the ratio between different harmonic tones can be found analytically. If we assume a driving modulation signal $S = S_{dc} + S_{am}cos(2\pi f_m t)$, we can write:

$$\frac{h_1}{h_{n_{even}}} = \frac{sin(\frac{\pi S_{dc}}{S_\pi})J_1(\frac{\pi S_{am}}{S_\pi})}{cos(\frac{\pi S_{dc}}{S_\pi})J_{n_{even}}(\frac{\pi S_{am}}{S_\pi})}\frac{h_1}{h_{n_{odd}}} = \frac{J_1(\frac{\pi S_{am}}{S_\pi})}{J_{n_{odd}}(\frac{\pi S_{am}}{S_\pi})}. \tag{2.24}$$

As previously derived, the even harmonics including the carrier frequency can be eliminated for a dc component equal to $S_{dc} = \frac{S_\pi}{2}$.

An alternative architecture to the SSB scheme is serrodyne modulation. One of the advantages of this scheme is the lower level of complexity, since the core structure consists of a single phase shifter. The key principle is the modulation of the phase shifter by a sawtooth waveform (2.12), resulting in a linearly increasing phase in the time domain and therefore a frequency shift equal to the modulation frequency, $\frac{1}{T_{mod}}$.

The peak value of the sawtooth waveform is equal to $S_{2\pi}$. Therefore, the linear segment of the driving signal can be written as:

$$S(t) = \frac{S_{2\pi}}{T_{mod}} t. \tag{2.25}$$

The electric field at the output of the phase shifter can be given by:

$$\begin{aligned} E_{out} &= E_{in} e^{\frac{2\pi n_0 L_{arm}}{\lambda}} cos(\omega_0 t + \frac{2\pi p L_{arm}}{\lambda} S(t)) = \\ & E_{in} e^{\frac{2\pi n_0 L_{arm}}{\lambda}} cos(\omega_0 t + \frac{\pi}{S_\pi} S(t)) = \\ & E_{in} e^{\frac{2\pi n_0 L_{arm}}{\lambda}} cos(\omega_0 t + \frac{2\pi}{T_{mod}} t). \end{aligned} \tag{2.26}$$

One of the critical aspects of serrodyne modulation is the peak value of the sawtooth waveform. In the ideal case, a $S_{2\pi}$ is required in order to perfectly cancel one of the sidebands. However, being able to generate a full $S_{2\pi}$ is not always a trivial task, mainly because it can lead to unrealistically lengthy components for an integrated system. Another challenge we need to face in a serrodyne modulation scheme is the finite fall time of the sawtooth waveform due to the limited bandwidth of the driver generator. The effect of these non-idealities can affect the Sideband Suppression Ratio (SR).

2.5 Summary

In this chapter, an overview of the main photonic label-free transducers was initially provided. Despite the low *LoDs* achieved with MZI structures, their large footprints do not facilitate the design of densely packed arrays for multiplexed sensing. This challenge is addressed using highly miniaturized resonant transducers, which instead rely a sharp resonant spectrum. One of the most widely used photonic transducers, the MRR, was presented and its key characteristics and photonic sensitivity were analyzed. Next, amplitude and phase photonic architectures were optimized in terms of their sensitivity. Starting from an intensity-based single-MRR scheme, more sensitive phase-based sensing schemes were also analyzed, thus enhancing the overall sensitivity of the photonic system.

Chapter 3

CMOS 45RFSOI as a Biophotonic Platform

Co-integration of nanophotonic sensors with state of the art electronics in a high volume and low cost commercial monolithic platform will create a breakthrough towards self contained, affordable PoC photonic sensors. Instead of relying on bulky optical and electronic equipment for optical scanning and readout processing, co-integrated electronics can unlock the door to low cost single λ laser diodes and on-chip processing of the optical signal embedding the molecular information. To achieve this, we rely on the zero-change integration of photonic components in a high volume, advanced electronic process node (GF 45nm RF-SOI CMOS) [35].

3.1 Monolithic Electronic-Photonic Process

The chip cross-section is illustrated in Fig. 3.1. As a first step, after the flip-chip packaging of the die on a PCB we fully etch the Si handle to expose the photonic sensors to the fluidic samples [30] and prevent leakage of the waveguide mode into the silicon handle. Undoped Si-crystalline transistor body is used as the waveguide layer, while various available transistor dopings are leveraged to create pn, pin, etc., diode structures in the same layer, allowing the interaction between the electrical carriers and light due to the carrier-plasma effect [34]. The thin buried oxide layer (BOX) allows a relatively low confinement of the optical mode propagating in the thin Si-body waveguide layer. As a result of this, the effective index of the guided mode is affected by molecular binding events taking place on the BOX layer after the handle release.

3.2 Intrinsic Sensitivity

The first step for evaluating the sensing capabilities of a photonic transducer is to characterize the intrinsic sensitivity of the device. This strongly depends on the geometry of the waveguide

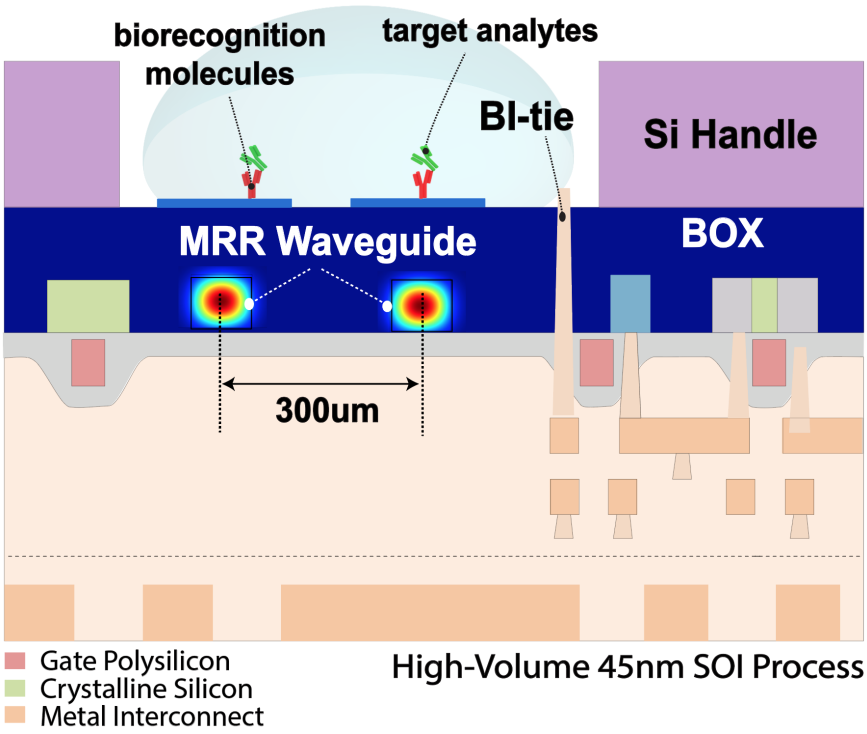

Figure 3.1: Zero-Change 45nm SOI cross-section.The thin Si-body waveguide layer allows a low confinement of the optical mode. Backside substrate etch exposes the sensing area.

and the process. The interaction of the evanescent field of the mode and the cladding environment induces a change in the effective index Δn_{eff}, which can then be translated to other parameters, depending on the type of the photonic sensor.

We evaluate the label-free sensing performance of our platform by examining two basic simulation setups: First, we characterize the bulk sensitivity of the process, as illustrated in Fig. 3.2. The RI of the cladding environment above the BOX is swept and the resonant shift of a default 5µm radius MRR is calculated. Detection of real time molecular kinetics is related to the surface sensing performance of the platform. In order to characterize this sensing capability, we model molecular binding events as spheres of a specific radius and RI landing on the surface of the SiO_2 BOX layer, as shown in Fig. 3.3. For proteins, we assume a radius of 5nm and a RI of 1.45, where as for viral particles we can scale the radius to be in the 100-200nm range.

All simulation results are derived using Lumerical. Figure 3.4 shows the simulation setup used in the Lumerical environment in order to characterize the intrinsic sensitivity of the process. First, we create the layer stackup of the 45nm platform. The Si-waveguide is embedded in the SiO_2 BOX layer and an additional SiO_2 layer is assumed below the waveguides. Initially, the cladding environment of the setup is assumed to be air of RI=1.

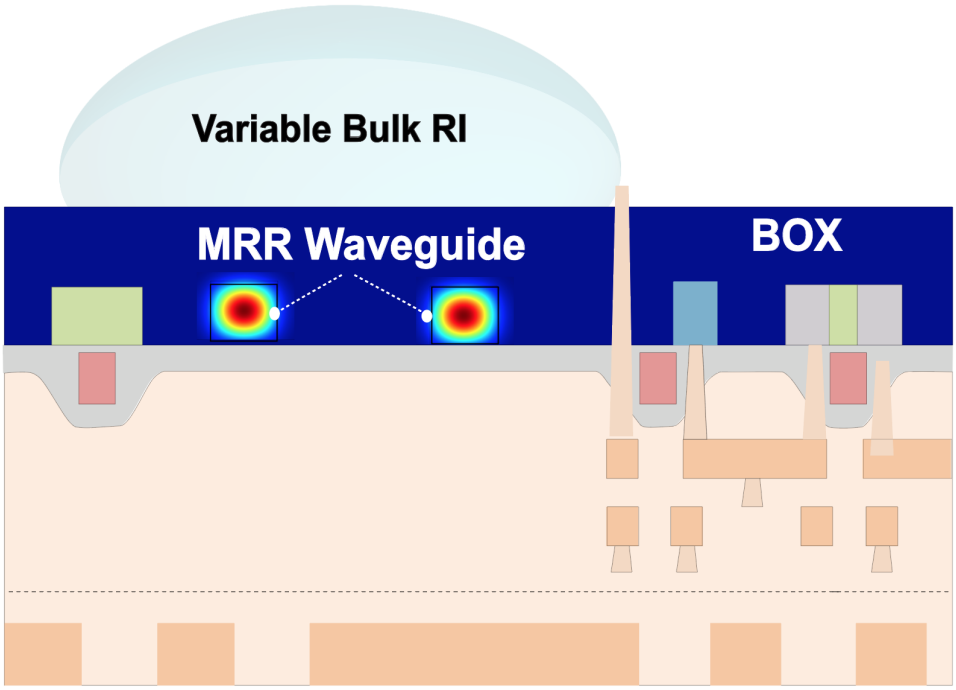

Figure 3.2: Bulk sensing simulation setup. The RI of the cladding material is swept to model the effect of a different background solution on top of the sensor.

The width and height of the waveguide is 1.2µm and ≈70nm respectively similar to the characteristics of the ring waveguide in our monolithic platform. For biosensing applications a low mode confinement of the optical mode is desired, resulting in stronger interactions with any environmental change in the cladding environment. As the waveguide thickness decreases, the mode is less confined leading to stronger interactions. However, this results in higher losses and therefore a lower quality factor Q, thus degrading the effective photonic sensitivity of the device.

After building the layer stackup and defining a simulation volume, the RI of the cladding environment is swept within a range of 1.3-1.7 RIU and the bulk sensitivity of the platform is extracted. This sensitivity metric is related to the response of an MRR to large and uniform changes of the cladding environment and can provide information about the effect of bulk environmental changes on the ring. Target analytes are diluted in buffer solutions flowing over the sensors. These background fluids can introduce large RI changes in the cladding environment and result in a significant resonant shift, which can be considered as an offset signal to be cancelled. Therefore, characterizing the bulk sensitivity of the process allows us to estimate the effect of buffer solutions and the amount of resonant shift that needs to be calibrated so that molecular detection starts from a ring bias point near resonance.

Assuming a 5µm MRR, a bulk sensitivity of $5\frac{nm}{RIU}$ is simulated, as illustrated in Fig. 3.5.

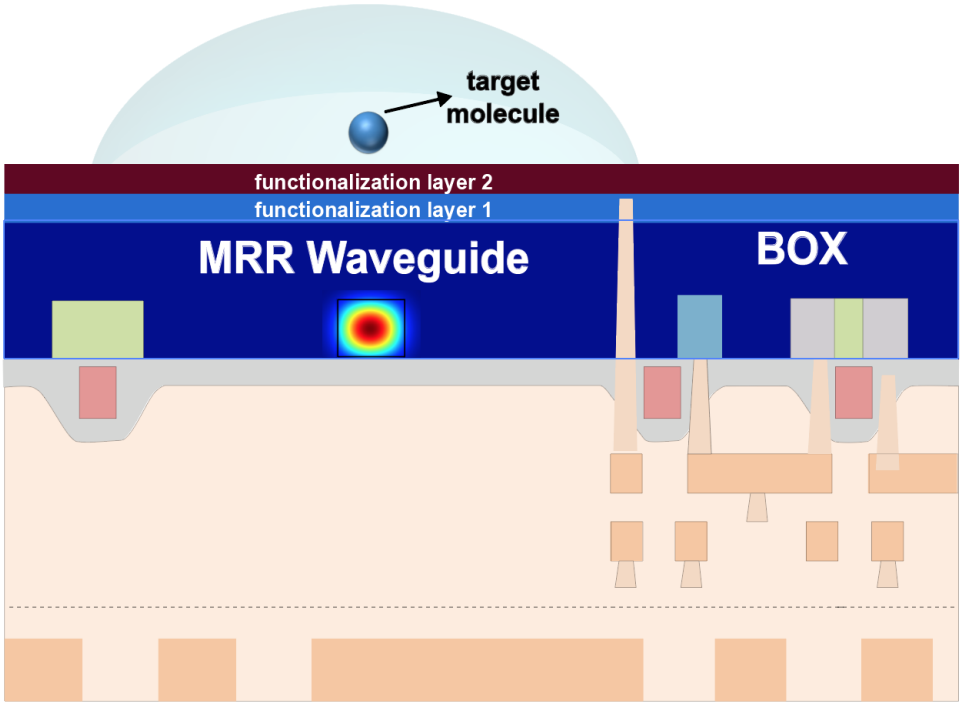

Figure 3.3: Surface sensing simulation setup. Target molecules are modeled as spheres of a specific radius and RI, binding on a functionalized surface with bioreceptors.

This results in an offset shift of ≈1.65nm when the sensor is exposed from air to water, which is the buffer solution for most testing fluids. A reduced BOX thickness can significantly boost the intrinsic sensitivity. This can be explained from the less confined mode propagating in the waveguide which results in stronger interactions with the cladding environment. A 100nm partial etch is expected to increase by 7x the bulk sensitivity [30].

Real time molecular kinetics are related to the surface sensing performance of the platform. In order to characterize this sensing capability of the platform, we model molecules with spheres of a specific radius and RI, as shown in Fig. 3.3. Initially the effective index of the mode is calculated when the cladding environment is water and the surface of the BOX layer is coated with two layers: (1) an aminosilane layer of ≈3nm used for binding receptors and (2) a layer of ≈5nm thickness which represents a uniform molecular layer of receptor antibodies. This assumes that a large receptor concentration was used in order to functionalize the waveguide and fully covers the surface. By simulating the change of the effective index before and after binding a sphere (Fig. 3.3), the effect of a single molecule can be calculated. For a protein of 1.45 RI and 5μm radius, this is found to be ≈0.03fm. Additionally, for a particle of 140nm and RI=1.6, similar to the characteristics of viral particles, the shift is ≈170fm, or equivalently 0.17% of the MRR's $FWHM$.

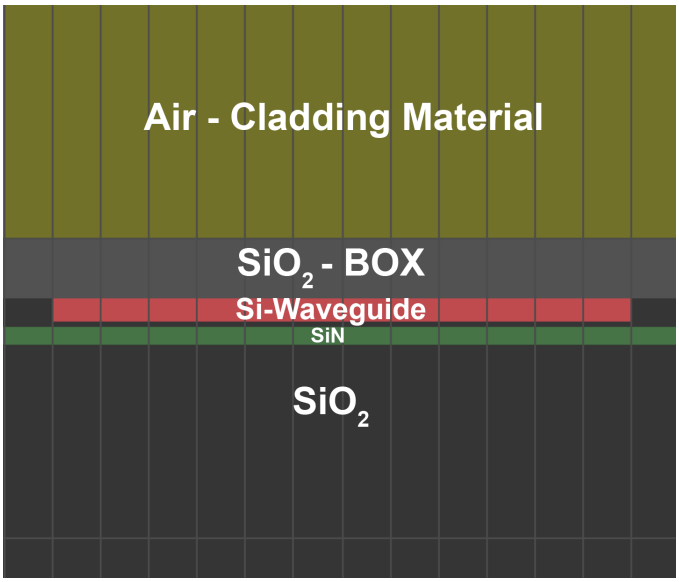

Figure 3.4: Lumerical simulation layer stackup.

3.3 Preliminary proof of concept

3.3.1 Bulk sensitivity

As a first proof of concept, we establish the label-free sensing capabilities of the platform by presenting preliminary experimental results of evanescent field sensing in our 45RFSOI process using a passive chip. Through these experiments we unlock the path towards a drastically miniaturized label-free biosensor in our high volume monolithic platform and also verify the modeling and simulation results in Lumerical.

In the first section, we characterize the bulk sensitivity of the platform which is related to the response of the sensor to a uniform and homogeneous change of the cladding environment. In order to ensure that the change of the cladding RI exceeds the evanescent length and can be assumed to be uniform, large drops of different RI optical oils (Cargille Labs) were spotted on top of the sensors, as shown in 3.6. The estimated thickness of the drop is ≈20µm. The resonant shift of the MRR is shown in Fig. 3.7 for different RI oils in the range of 1.3 to 1.7 and a step of 0.1. An average bulk sensitivity of ≈5nm/RIU was measured, which is in close agreement with simulation results in Lumerical Mode Solutions.

3.3.2 Real time kinetics

3.3.2.1 Functionalization and Protein Immobilization

One of the most critical parts in a biosensing platform is the interface between the sensing transducers and the biological samples. A robust interface between testing solutions and

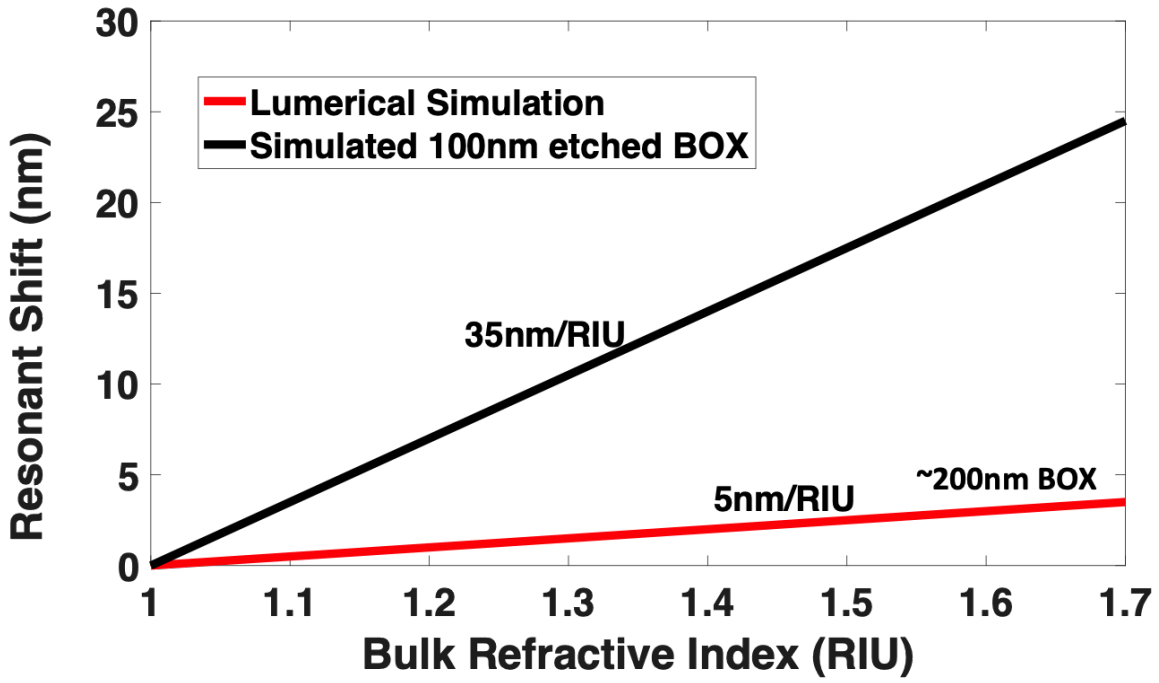

Figure 3.5: The bulk sensitivity of the 45nm process is evaluated. The resonant shift of a default MRR with ring radius of 5µm is calculated for different RI values of the cladding environment. A boost in sensitivity can be achieved with a reduced BOX thickness.

photonic transducers is key for a highly sensitive biophotonic system. In affinity-based sensors, the biorecognition molecules need to be immobilized on the sensor's surface in order to specifically bind to the target analytes of the testing solution. A wide variety of functionalization protocols have been used in label-free sensors. One of the key challenges is to verify that our monolithic electronic-photonic platform is compatible with state-of- the-art cost effective functionalization protocols. The Si substrate release required for preventing any leakage of the waveguide mode into the substrate, could potentially interfere with any surface chemistry for protein immobilization. Therefore, being able to verify the functionality of a simple protocol in our process is an important step.

The surface chemistry applied in Si-based label-free sensors is based on silane reagents that have a wide range of functional groups. This allows the efficient coupling of receptor molecules to an aminosilane layer formed on top of the sensors. In order to verify the functionality of the protocol, the gold standard of avidin-biotin was used. The strong affinity rate of avidin for biotin allows safe conclusions regarding the efficiency of the surface chemistry. For that reason, the same pair was used for the real time kinetic measurements, presented in the next chapter.

Biotin is a vitamin found in all living cells with a mass of about 244 Da. It is widely used

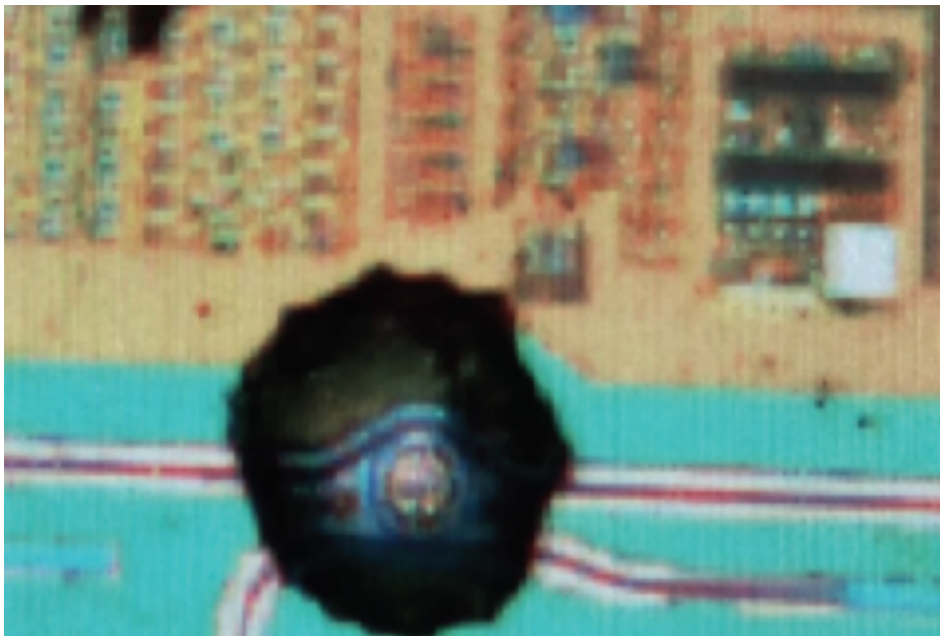

Figure 3.6: Optical oil drops spotted on MRRs for bulk sensitivity measurements. The diameter of the drops delivered with a 30-type needle gauge is ≈20µm, therefore fully covering the 5µm radius rings.

in increasing the sensitivity of many assays since it can be conjugated to many proteins. Avidin is a glycoprotein with a mass of approximately 68 kDa. There are four identical subunits where one biotin protein can bind. The protocol verification experiments were performed with glass slides, since the top surface of our sensors is a SiO_2 BOX layer. Biotin is immobilized on the glass slide's surface as a receptor molecule and streptavidin is the target analyte in the sample solution.

As a first step, the glass slide was dip coated for 3 minutes in a 2% APTES-ethanol solution in order to be functionalized with aminosilane groups. Immobilizing biotin receptor molecules on the sensor's surface was verified using a fluorescent microscope. Specifically the binding between biotin and streptavidin is visualized under a FITC fluorescent microscope. The APTES coated glass slide was first spotted with biotin drops and incubated overnight in a cool environment. After washing off the glass slide, we then spot the slide with a large drop of streptavidin conjugated with Alexa fluorophore. Using a FITC filter, the glass slide was excited with the fluorophore's excitation wavelength of 488nm. The functionality of the protocol was verified using the relative brightness in the area where biotin drops were delivered. This can be explained from the binding of streptavidin labeled with Alexa fluorophore to biotin which results in higher brightness, as shown in Fig 3.8.

The glass slide includes three main distinct areas. The brighter spots correspond to the specific binding between the labeled avidin and biotin. However, around these spots, a less

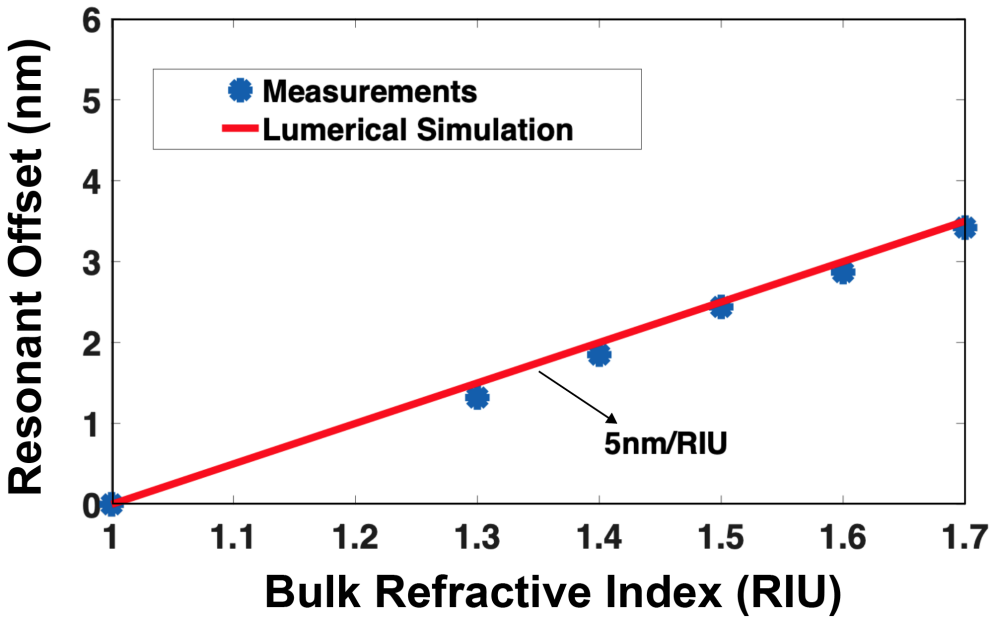

Figure 3.7: Bulk sensitivity of the 45nm RFSOI platform.

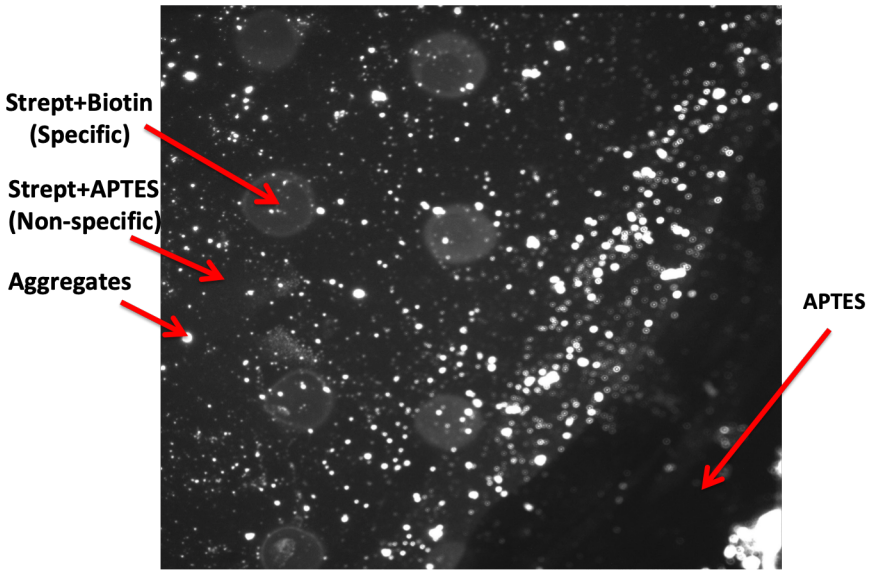

Figure 3.8: Fluorescent visualization of specific binding between avidin and biotin using a FITC filter. The bright spots correspond to biotin-avidin pairs. The less bright region indicates some amount of non-specific binding.

bright region can be observed. This is the result of non specific binding of avidin directly to APTES. Being able to estimate and quantify non specific binding is one of the greatest challenges in label-free assays since it becomes a source of false positive results and increases the Limit of Detection. More advanced functionalization protocols can be used to block any non-specific binding [29]. However, as will be discussed in Chapter 5, we aim to suppress non-specific binding by relying on an on-chip differential readout scheme comprised of sensing and reference MRRs, eliminating the need for complex chemistry. Finally, the darkest area of the slide corresponds to an APTES-only functionalized surface.

3.3.2.2 Microfluidic Delivery Mechanism

Static functionalization of the surface by delivering labeled streptavidin drops results in numerous protein aggregates dispersed all over the slide, as shown in Fig. 3.8. The size of these protein aggregates - seen as bright spots - can interfere with the real time signal obtained from molecular kinetics, since it affects both the quality of the surface chemistry and decreases the surface sensitivity of the platform. Therefore, a more dynamic way of functionalizing and performing the kinetic experiments is required, indicating the need for a microfluidic channel network delivering the testing solutions.

Interfacing with mm-scale chips requires fluidic networks with a size smaller than the size of the die. This ensures robust bonding of the fluidic device, leveraging the flat surface of the chip. A first generation PDMS-based fluidic package was fabricated for preliminary kinetic experiments in our monolithic platform. Microfluidic devices at the size of the chip had to be fabricated, creating challenges in fabricating the PDMS structures guiding the fluid as well as patterning the fluidic inlet/outlet ports and cuts for fiber access. Furthermore, bonding of the PDMS core device on the chip should not require any extra chemical processing that could affect the surface chemistry applied for protein coupling. This suggests that mechanical pressure needs to be applied to attach the microfluidic device on chip, thus preventing any fluidic leakage. Figure 3.9 shows the PDMS layer clamped on the CMOS chip only through mechanical pressure, avoiding the need for irreversible chemical bonding.

The core of the microfluidic design (Fig. 3.10), consists of a bottom PDMS layer of 5.2mm$x$2mm mounted on a 6mm$x$3mm CMOS processor chip with monolithically integrated photonic I/O rows. Its low footprint allows miniaturization of the CMOS die and coupling access to other photonic structures for different applications. In this chip, ring filter banks with doped MRRs of 5um radius, 10k Q and 100mm pitch were utilized as the sensing sites. Each row consists of 11 rings that can be used as sensing or reference devices. The microfluidic channel covers a sensing ring in the row, whereas the rest of the rings can be used as references for cancelling any shifts from ambient temperature changes or pressure.

This first generation single channel microfluidic device paves the path towards the design of fluidic packages interfacing with fully integrated mm-scale dies, while ensuring simultaneous electronic, photonic and fluidic package. However, this single-channel implementation limits the number of rings that can be tested, therefore not allowing multi-analyte sensing. Additionally, a single channel covering one ring does not allow the exposure of any

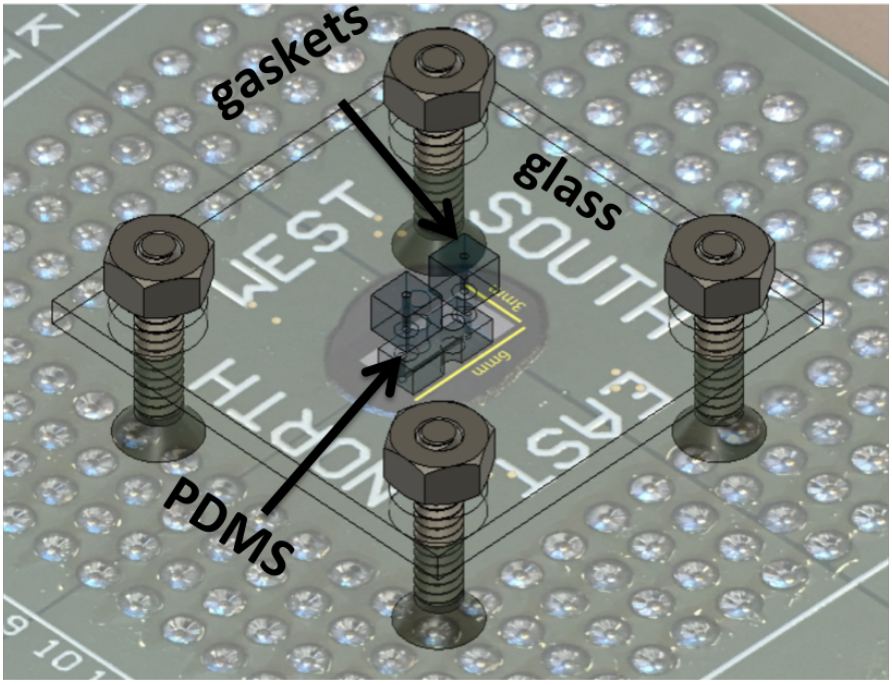

Figure 3.9: A first generation single channel microfluidic device is attached on-chip using mechanical pressure with a glass substrate, thus avoiding any fluidic leakage. Holes are cut in the PDMS for the inlet/outlet ports and the fiber access areas.

reference MRR structures under the same environmental conditions, since the rest of the rings are covered by PDMS. Therefore, we cannot precisely subtract ambient common mode errors induced from environmental variations and also cannot get insight into non-specific binding. In order to address these challenges, we propose a next generation multi-layer and multi-channel microfluidic packaging strategy, presented in Chapter 4.

3.3.2.3 Passive experiments

The surface sensing performance of the chip was evaluated through the molecular interactions between biotin, acting as the probe molecule functionalized over the released BOX surface and streptavidin as the target molecule. In Fig. 3.11, the experimental setup used to demonstrate the sensitivity of the platform is shown. A tunable laser (SANTEC TSL-510) performs multiple scans of the ring row's through port transfer function at a scanning rate of 1min/scan and a step of 5pm while the output power is measured with a power meter (Agilent 8164B).

After the substrate release, the chip was first dip coated for 3 minutes in a 2% APTES (aminosilane)-ethanol solution. A 3mM biotin-PBS solution was then flowed through the

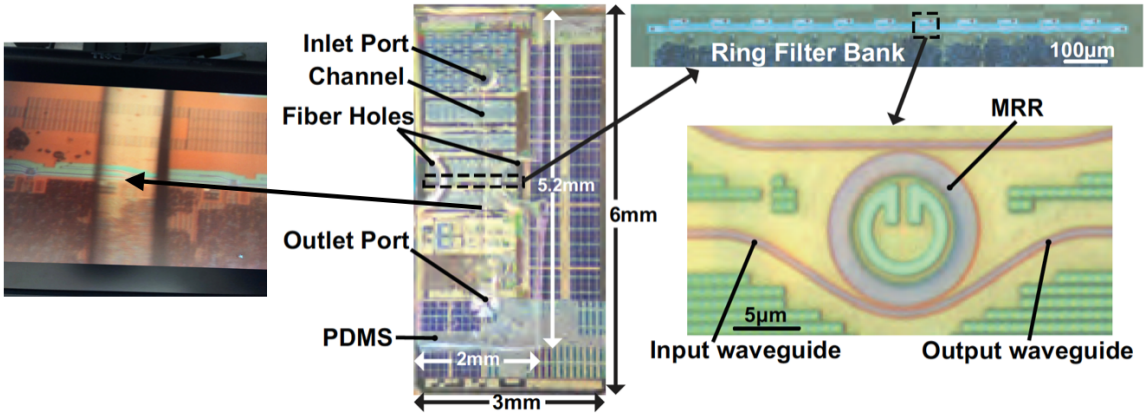

Figure 3.10: PDMS device mounted on the fully Si-substrate released functional processor die, with holes drilled to allow fiber and fluidic access. A ring filter bank is used as the testing site, with 5µm radius MRRs for sensing and drift cancellation. A 100µm wide channel covers the sensing ring.

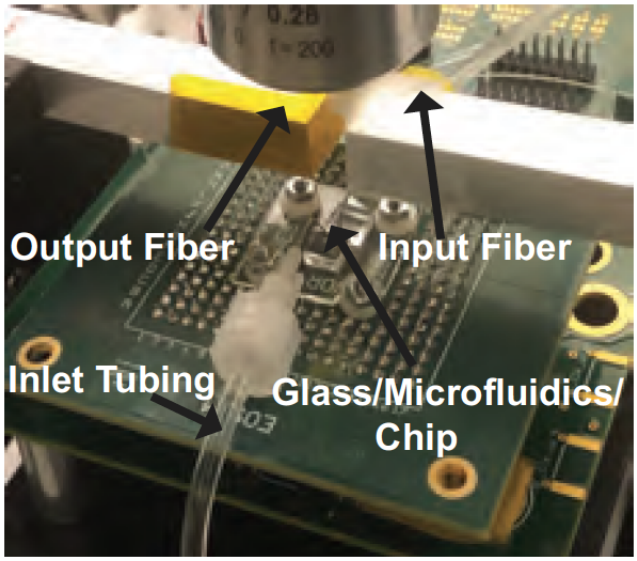

Figure 3.11: Experimental setup with coupled fiber optics and microfluidics.

microfluidic channel for 10 hours, to functionalize the sensor with the receptor molecules. The binding between biotin and streptavidin was tested with three different concentrations of streptavidin-PBS solutions flowing through the channel. Figure 3.12 shows the real time resonant shift of the functionalized MRR for the different solutions tested [30].

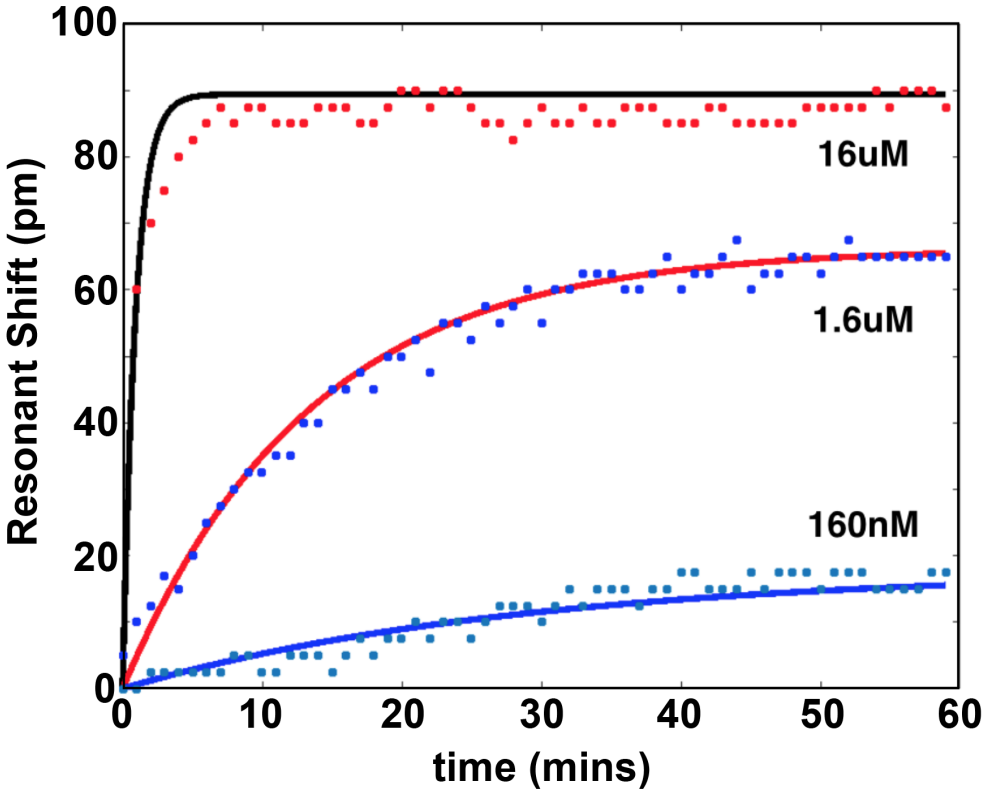

Figure 3.12: Real time resonant shift of biotin-streptavidin binding for different streptavidin concentrations. Solid lines represent the fitted binding curves from the kinetics molecular equation.

The binding curves are fit to standard pseudo-first order kinetics equation governing protein binding [29], given by:

$$\frac{d[AB]}{dt} = k_a[A][B] - k_d[AB], \tag{3.1}$$

where $[AB]$ is the concentration of the binding pairs between A and B, $[A]$ is the target molecule concentration and $[B]$ is the concentration of the unbound molecules of B that acts as a receptor for target A. The association and dissociation rates are given by k_a $(\frac{1}{Ms})$ and k_d $(\frac{1}{s})$ respectively. Assuming the change of the effective index and the wavelength shift to be proportional to the concentration of bound molecules on the sensor, equation 3.1 can be expressed in the resonant shift domain as follows:

$$\frac{d\Delta\lambda_{res}(t)}{dt} = k_a[A]A_{area}[B_{max}]S_{int} - (k_a[A] + k_d)\Delta\lambda_{res}(t), \tag{3.2}$$

where $\Delta\lambda_{res}$ is the real time resonant shift of the ring, A_{area} is the active area of the function-

Table 3.1: Initial binding slope vs Avidin concentration

Avidin Concentration	Initial Slope
160nM	$1\frac{pm}{min}$
1.6µM	$5\frac{pm}{min}$
16µM	$95\frac{pm}{min}$

alized ring for protein binding, $[B_{max}]$ is the initial concentration of the receptor molecules, $[A]$ is the target analyte concentration and S_{int} the intrinsic sensitivity of the ring ($\frac{nm}{molecule}$).

The initial binding slope $\frac{d\Delta\lambda_{res}(t)}{dt}$ at t=0 can be found by the kinetics equation in the resonant shift domain, assuming that initially $\Delta\lambda_{res}(t=0)=0$. Therefore, we can write:

$$\text{Slope} = k_a[A]A_{area}[B_{max}]S_{int}. \tag{3.3}$$

This shows that the initial slope scales linearly with the initial receptor molecule concentration $[B_{max}]$, the sensitivity S_{int} and the concentration of the target analyte $[A]$. Furthermore, it also depends on the affinity rate constant k_a of the molecular reaction.

From the real time kinetics obtained in Fig. 3.12 the effect of streptavidin concentration on the initial binding slope is clear. For higher avidin concentrations the binding reaction is faster. Table 3.1 shows the initial slope for different avidin concentrations. The experiments for 160nM and 1.6µM were done sequentially. This can explain the reduced scaling of the slope at 1.6µM, which is not linearly increased by 10 times. After the first experiment, some of the binding spots have been covered by avidin, resulting to a lower number of receptor molecules available for binding in the next experiment. Since the receptor concentration linearly affects the initial binding slope, the measured slope for the 1.6µM avidin concentration is lower than expected. However, the binding curve at 16µM streptavidin – done as a separate experiment – shows that the initial slope is approximately 100x larger than the slope at 160nM, which agrees with the predicted linear behavior from the kinetics equation.

From this preliminary set of real time kinetics in 45RFSOI process we can highlight a key limitation of the testing setup. Residual ambient temperature fluctuations can be observed in the binding curve. This can be explained from the the different cladding material to which sensing and reference rings are exposed. Reference rings are under PDMS, which has a more negative thermo-optic coefficient than the aqueous cladding environment of the sensing rings. Therefore, any ambient temperature fluctuations will result in different wavelength shifts for the sensing and reference rings. These shift fluctuations can be further reduced by exposing the rings to the same cladding environment.

3.4 Summary

In this chapter, we introduced the fully integrated electronic-photonic high volume 45nm process and established the label-free sensing capabilities of the platform by demonstrating preliminary RI and molecular kinetic results. First we characterized in Lumerical the bulk and surface sensitivity of the process. A sample fluidic solution flowing over an MRR will create a large bulk RI change in the cladding environment and local fine RI changes induced from molecular binding events. Next, we demonstrated preliminary bulk RI and label-free sensing results from a 45nm SOI photonic chip, establishing an initial proof of concept. Using a first generation single-channel microfluidic device and applying an APTES-based functionalization protocol, real time molecular kinetics of biotin-streptavidin binding were presented at different concentrations, unlocking the path towards the world's first fully integrated electronic-photonic SoC (EPSoC), presented in Chapter 5.

Chapter 4

Multi-Channel Microfluidic Systems

Label-free MRR-based assays have been able to provide real-time information from a wide range of molecular concentrations of different target analytes, ranging from femtomolar to micromolar, by leveraging high transducer sensitivity and small footprints [30, 36–44]. However, one of the key challenges towards efficient and diverse multiplexed sensing of multiple biomarkers is the fabrication of fluidic delivery devices to interface with the extraordinary density and degree of integration of arrays of micrometer-scale MRRs, while allowing both optical and electrical coupling to the integrated circuit, which is often on a millimeter-square scale. Microfluidic interfaces with silicon photonic chips require (a) regular surfaces to form a seal and prevent leaking, (b) optical clarity for alignment, (c) high aspect ratio ($\geq$5:1) vias to communicate with dense channel networks ($\leq$100 µm width, $\leq$100 µm pitch), (d) access areas allowing fiber optics to couple light into the system, and (e) an efficient fluidic delivery mechanism adjusted to millimeter-scale footprint areas. In this chapter, we propose an efficient and rapid packaging strategy for fabricating multi-channel and multi-layer microfluidic packages using 3D-printed molds. This packaging methodology allows the development of fluidic networks delivering multiple solutions to µ-scale ring sensors on mm-scale dies, while ensuring simultaneous electronic and photonic coupling.

4.1 Background

Current approaches to meet the aforementioned constraints often require custom packaging techniques to accommodate centimeter scale microfluidics [45] or complex post processing following conventional multi-layer soft lithography [46]. While there are many techniques to create a sufficiently regular surface [45], a potential strategy is to create microfluidics that are smaller than the footprint of the die, as the small chip surface area is regular enough for secure bonding [46, 47]. By doing this, we eliminate the need for larger chip areas that would significantly increase cost. A larger secondary microfluidic layer – which directly interfaces to the smaller primary chip-bonded layer – can route fluid to the small footprint region allowing for a macro-scale tubing interface that supports complex channel structures.

This multi-layer interface approach requires precisely aligned microfluidics at two different scales. Creating each layer via photolithography traditionally offers the greatest precision in channel dimensions and surface finishes, but requires complex processing to create high-density vias and align multiple layers [48]. A hybrid of soft lithography and laser micromachining can be used to address these challenges but requires expensive and specialized equipment [46]. Additive manufacturing can greatly reduce the complexity in fabricating such multi-layer devices through 3D printed transfer molding wherein each layer is cast on a printed mold. Despite the promise of 3D printing, fabrication of molds for microfluidics has been historically limited by the inability to produce the smooth surface finishes – necessary for both visualization through the microfluidic layers as well as proper sealing – and minimum feature sizes of photolithography, and has thus been limited to centimeter scale microfluidics [49].

Commercial printing technology has now crossed the resolution threshold to overcome surface finish, feature size, and aspect ratio constraints in designing millimeter scale microfluidics. Leveraging these advances, we demonstrate a simple, highly scalable, and versatile multi-layer microfluidic device for CMOS integration created by 3D printed transfer molding and bonding. This packaging architecture can enable multiplexed analyte sensing without requiring large die surfaces and complicated fabrication techniques, while it ensures a robust interface between the photonic sensors and the fluidic samples.

4.2 Microfluidic Packaging Strategy

3D printed transfer molding enables rapid fabrication of multi-layer microfluidics for co-packaging with highly miniaturized silicon photonic chips as seen in Fig. 4.1.

This versatile packaging technique can accommodate multi-fluidic and photonic coupling, independent of the electronic interface. As a first step, the advanced process node of the 45nm SOI fully integrated electronic-photonic platform requires release of the Si substrate to prevent leakage of the optical mode in the substrate and expose the photonic sensors to the fluidic samples, as illustrated in Fig. 4.1a. In the package shown in Fig. 4.1b, the silicon die is flip chip bonded on a printed circuit board (PCB) for electrical coupling and multi-layer microfluidics are mounted on top of the chip. Our microfluidic design consists of two polydimethylsiloxane (PDMS) layers and a glass substrate for mechanical stability. The layers are enumerated by proximity to the chip wherein the small footprint PDMS layer in contact with the chip is layer 1 ("primary layer"), the larger layer for fluid routing is layer 2 ("secondary layer"), and finally the glass substrate is layer 3.

4.2.1 3D printed Mold Fabrication

The mold for each PDMS layer is designed in CAD (Autodesk Fusion360) as an array of devices with various geometries of vias, channels, and access areas for optic fibers that act as photonic ports. To test the limitations of the printed molds, we designed devices ranging

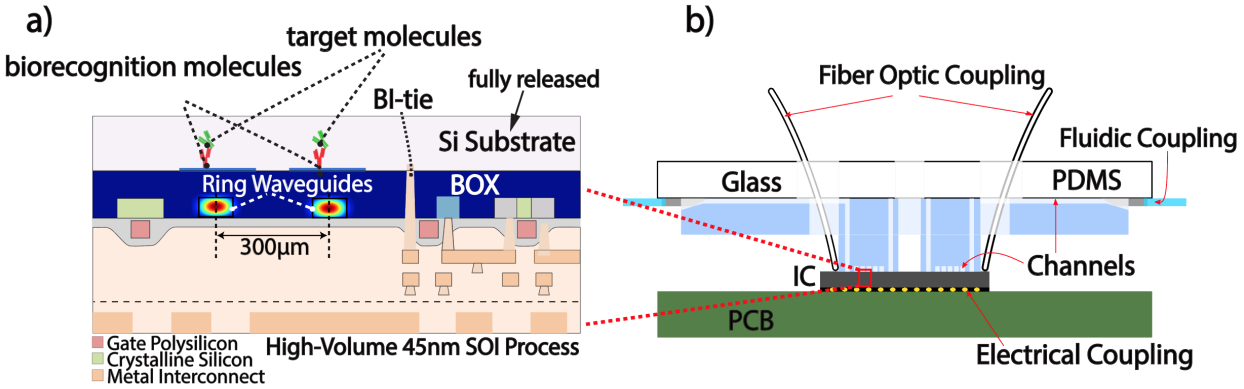

Figure 4.1: (a) CMOS 45RFSOI process cross-section. Backside Si substrate etch exposes the sensing photonics to the fluidic samples. (b) Cross section of microfluidic package aligned to chip. Photonic ports allow for fiber optic coupling, needles inserted at the edge allow for fluidic coupling, and flip chip bonding allows for electrical coupling. Layer 1 interfaces with the chip, layer 2 routes fluid to tubing, layer 3 provides mechanical support.

from 4 to 14 channels, 8 to 28 vias, and 3 photonic ports on a 5.5mm by 3mm footprint to match the size of our chip. The final 3D model forms high aspect ratio vias (between 5:1 to 15:1), high resolution channels, meso-scale photonic ports, and alignment marks as demonstrated in Fig. 4.2. Alignment marks aid in precisely locating multiple layers while assembling the final device.

The model was submitted for fabrication by projection micro-stereolithography (Boston Micro Fabrication) with 2 µm resolution. In our instance, we achieved a smooth surface finish with well defined channel geometry, 75 µm channel spacing, 10:1 via aspect ratio, and millimeter scale photonic port features, meeting the requirements for silicon photonic integration. Earlier attempts of printing similar molds using high resolution fused deposition modeling and stereolithography printers failed to produce the necessary surface finish. Meanwhile, extremely high resolution 2 photon process printers could not produce larger meso-scale features.

4.2.2 Microfluidic Device Casting

The mold must be coated in a release agent prior to casting for a high-fidelity transfer of features without damage to delicate components of both the mold and the cast. To achieve this, the mold (Fig. 4.3a) is placed in a vacuum chamber with 500 µL of Trichloro(1H, 1H, 2H, 2H-perfluorooctyl)silane (Sigma) under vacuum for 15 minutes [50] as shown in Fig. 4.3b. The PDMS (Sylgard 184, Dow) is prepared by thoroughly mixing 10:1 pre-polymer to crosslinker and degassing under vacuum for 45 minutes [51]. Degassed PDMS is poured onto the silanized mold (Fig. 4.3c) and the mold is capped with a cleaned glass

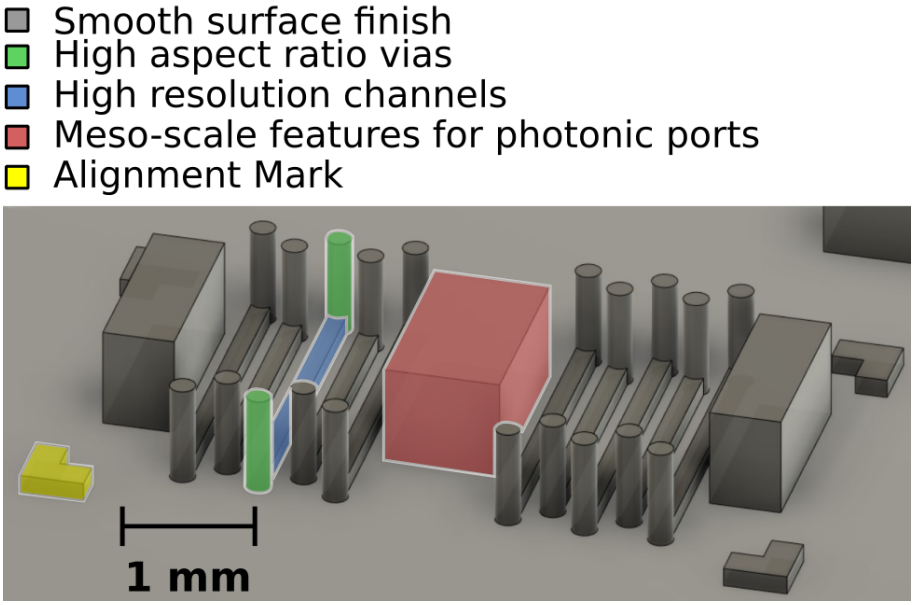

Figure 4.2: 3D printed mold model for 10 channel device with 20 vias, 3 photonic ports, and alignment marks.

slide (Fig. 4.3d) to ensure an even top surface with smooth finish required for multi-layer bonding.

A 500-gram weight is then placed on top of the glass to remove residual PDMS between contact areas on the mold and glass in order assure thru-hole formation for vias and photonic ports rather than thin membranes. The mold, PDMS, and glass sandwich is placed on a hot-plate at 95 degrees Celsius for 2 hours to cure the elastomer. After the PDMS has cured, the cast device is removed from the device and trimmed with a razor to its final size (Fig. 4.3e). This process is repeated for each layer of the final multi-layer device.

4.2.3 Glass substrate fabrication

The microfluidic package is attached on the chipboard trough mechanical pressure. This eliminates the need for permanent bonding of the microfluidic network on the chip and avoids the use of any chemical processing that could affect the quality of the aminosilane surface chemistry.

One of the key challenges in order to ensure robust attachment of microfluidics and allow enough space for the optical fibers to access the chip is the design and fabrication of a glass substrate (ios Optics) (Fig. 4.4), located at the top layer of the microfluidic package. The pressure through which the fluidic package is bonded on the chipboard is applied using screws passing though openings in both the glass and board, therefore holding the two parts

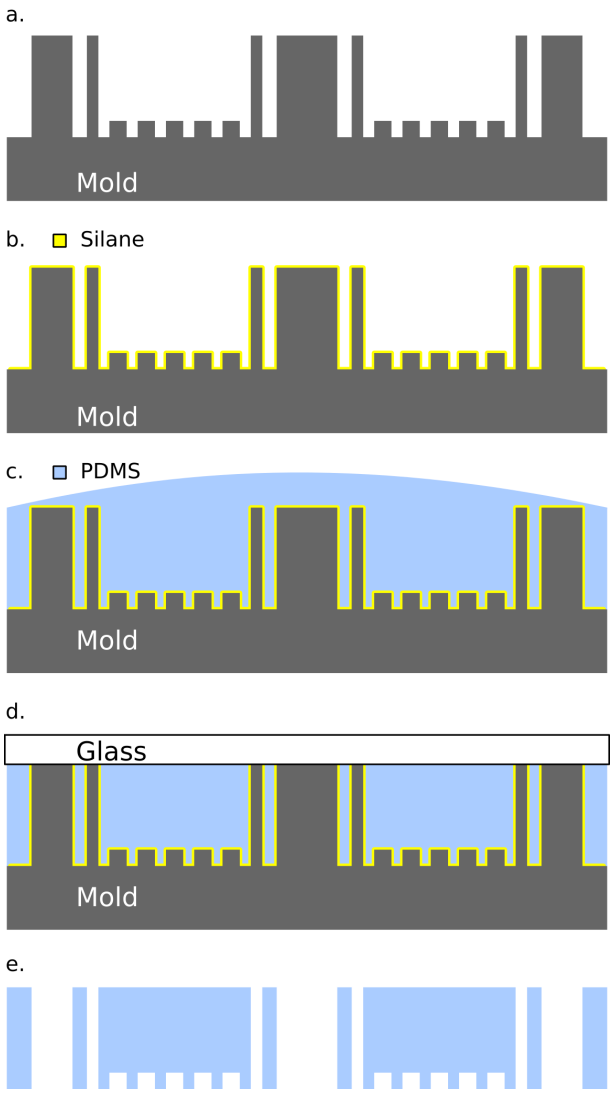

Figure 4.3: Workflow for casting PDMS on the 3D printed mold. (a) The mold is (b) silanized in a vacuum chamber. (c) Mixed PDMS is poured onto the mold and (d) the top surface is made uniform with a glass cap. (e) The PDMS is then cured and removed from the mold.

together. Glass Cuts A-D are aligned with chipboard openings and screws are passed through the aligned holes. In order to allocate space for fiber optics to access the chip and couple light, we pattern openings E, F on the glass. The cut on the left (E) provides space for fiber arrays to be bonded on chip whereas middle cut F allows access for single fibers. The absolute coordinates of the openings are determined based on the location of the chip and the grating couplers, assuming the glass and the chipboard have the same size. Additionally, a row of 1mm diameter holes are patterned on the top and bottom of the glass. These openings are

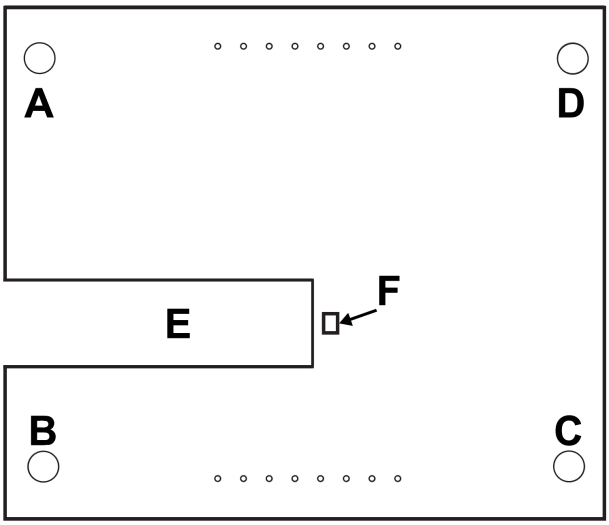

Figure 4.4: Layout of the glass substrate.

used as inlet and outlet holes for the delivery of multiple fluids to the microfluidic channels of the upper and bottom layer.

4.2.4 Alignment and Mechanical Sealing

Once layers 1 and 2 have been cast and the glass substrate (layer 3) is fabricated, we proceed with assembling the separate parts. Layer 2, denoted as upper PDMS in Fig. 4.5a, is first bonded to layer 3 with oxygen plasma by placing them in a reactive ion etch chamber with the mating surfaces exposed. Plasma introduces reactive hydroxyl groups on the surface that facilitate irreversible chemical bonding [52]. The mating surfaces are then aligned under magnification to maximize overlap between the photonic ports of the glass substrate and PDMS layer.

This assembly is placed on a hot plate at 65 degrees Celsius for 15 minutes to drive the reaction to completion. This process is repeated for bonding layer 1 to the layers 2,3 assembly. Coarse alignment is achieved by aligning corner holes in the glass substrate (Fig. 4.5b) with holes on the PCB with screws. Fine alignment is further achieved manually by leveraging optical transparency through layers of the microfluidic stack for visual alignment of channels to sensing structures on-chip. Once aligned, the channels are sealed to the chip through mechanical pressure by tightening corner screws. Bonding the microfluidics (Fig. 4.5c) to the chip exclusively through mechanical pressure allows for thorough decontamination of the chip surface between tests by entirely removing the package for reuse of the electronic-photonic chip. It also enables the rapid iteration of various channel geometries without requiring a unique chip to test each geometry.

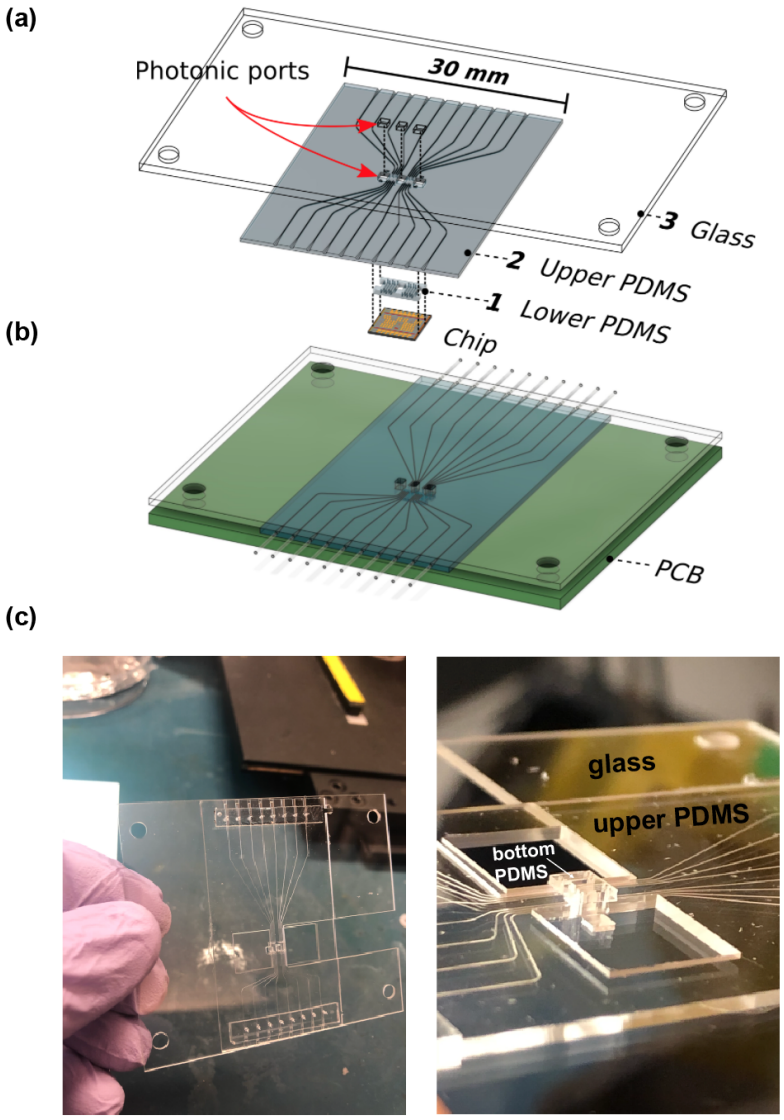

Figure 4.5: (a) Multi-layer stack of glass substrate and cast PDMS pieces are aligned and then bonded using oxygen plasma. (b) The assembly is then coarsely aligned to the printed circuit board (PCB) before fine alignment of channels to sensing regions. (c) Multi-layer and multi-channel fluidic package.

4.3 Microfluidic Validation

4.3.1 Dye Test

We demonstrate the functionality of the described microfluidic packaging by injecting colored dyes to detect leaks between channels. In Fig. 4.6, red dye is injected into a channel by edge

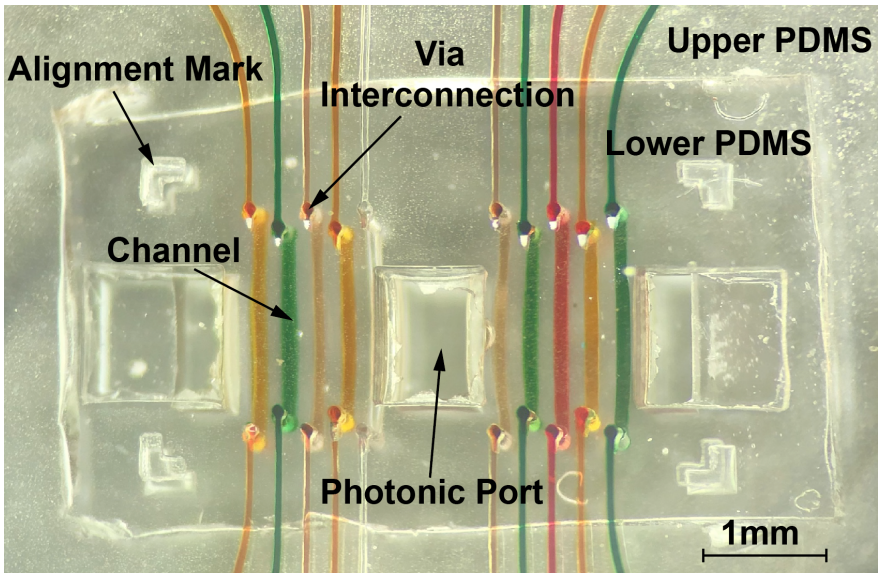

Figure 4.6: Red dye run through the multi-layer microfluidic assembly

coupling tubing with 28-gauge needles into a 4-channel microfluidic device. There was no cross contamination of dye in either the lower chip-sized PDMS channels or the larger upper PDMS channels. This test was done on glass for high contrast to best visualize any leaks. Once the proof of concept was verified using dye on glass, a 10-channel microfluidic package was aligned to 5 µm radius MRRs and optic fibers were aligned with grating couplers on-chip for photonic coupling.

4.3.2 Photonic Coupling and Bulk Sensitivity

Channels of the assembly were aligned to rings as described above. Then, 125 µm diameter lensed fibers are lowered through the photonic ports using micromanipulators on an optical table. These fibers are aligned to on-chip grating couplers to couple laser light into a waveguide. When the wavelength of the input light is at the resonant wavelength of an MRR, power couples into, and circulates within the micro-ring resulting in a power loss at the output coupler [25]. Fig. 4.7 is an infrared image of channels aligned to the MRRs of a fully integrated electronic-photonic system on-chip. Photonic coupling is demonstrated by the circulating power emanating from the rings.

The bulk sensing capability of the platform was then evaluated using the proposed microfluidic packaging strategy. Figure 4.8 shows the resonant shift of three rings located in three different channels. Channels 1 and 2 are exposed to water while channel 3 is empty. A resonant shift of 650pm was measured for the sensors under water resulting in a bulk sensitivity of ≈1.97 nm/Refractive Index Unit, which is lower compared to the bulk sensitivity characterized in Chapter 3, due to a thicker ≈200nm BOX layer. This high channel density

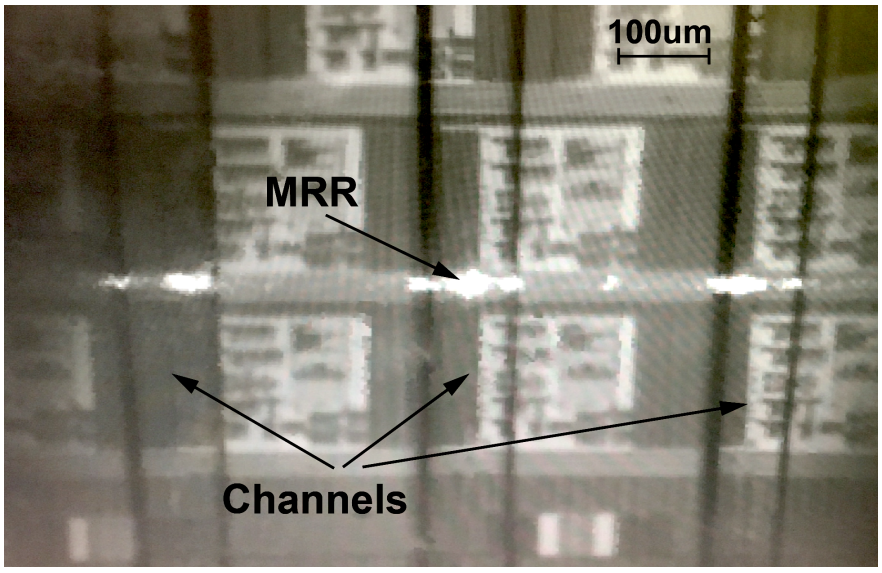

Figure 4.7: Power loss through micro-ring resonators while aligned to channels. This close up focuses on 3 channels from the 10-channel package of Fig. 4.5.

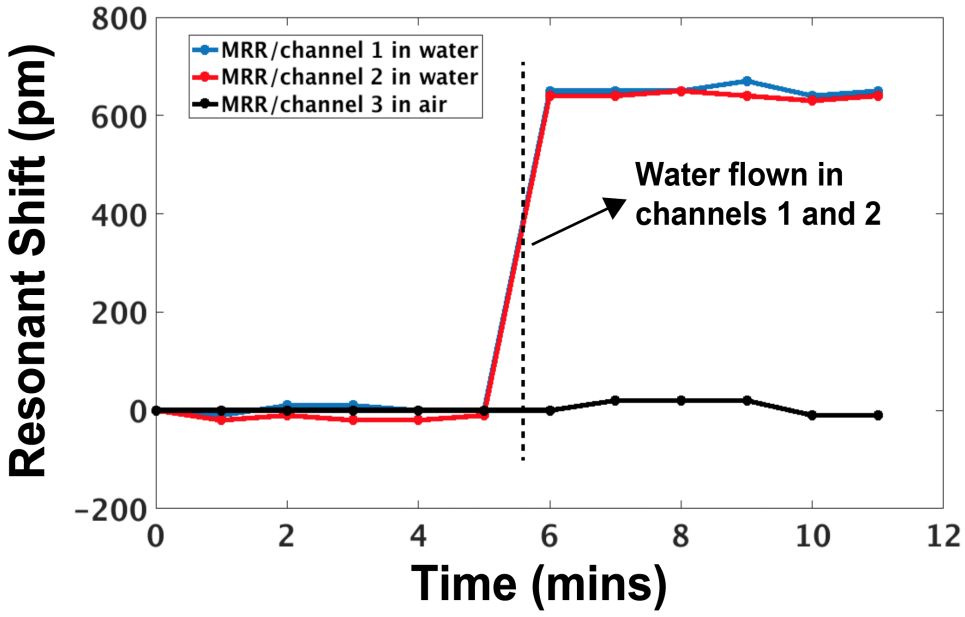

Figure 4.8: Resonant shift of MRRs exposed to water and air.

and miniaturized microfluidic device has the potential to integrate with a variety of silicon photonic devices.

4.4 Summary

We demonstrated a microfluidic packaging strategy for developing multi-layer and multi-channel fluidic networks interfacing with mm-scale chips. To achieve this, we rely on 3D-printed molds for fabricating PDMS-based devices with multiple high resolution channels and vias for communicating fluidic samples from a bottom to an upper layer. Commercial projection micro stereolithography paves the way for using 3D printed transfer molding to create silicon photonic compatible microfluidics. The ability to simultaneously provide electronic, photonic, and fluidic coupling using this rapid packaging methodology underlies its versatility. The facile fabrication of multi-layer dense channel networks with smooth surface finish and photonic ports can solve key challenges for multi-fluidic coupling, alignment of channels to µm-scale ring sensors, and coupling light to the photonic chip. This unlocks the door towards real-time monitoring of various analytes in a highly miniaturized photonic LoC system, while it provides low cost in-channel functionalization of multiple rings with different receptors without the need for expensive micro-array spotters.

Chapter 5

Monolithic Electronic-Biophotonic System-on-Chip

Co-integration of nanophotonic sensors with state of the art electronics in a high volume and low cost commercial monolithic platform will pave the path towards self contained and affordable PoC photonic sensors. Instead of relying on a bulky tunable laser and external electronic equipment for optical scanning and readout processing, co-integrated electronics can unlock the door to low cost single λ laser diodes and on-chip processing of the optical signal embedding the molecular information. To achieve this, we rely on the zero-change integration of photonic components in a high volume, advanced electronic process node (GF 45nm RF-SOI CMOS) [35].

5.1 Architecting "smart" EPSoCs for Real-Time Molecular Sensing

Moving towards our vision for highly scalable real-time and compact PoC molecular sensing, the fully integrated electronic-photonic platform unlocks the door for highly miniaturized Lab-on-Chip photonic label-free sensors by enabling key sensing capabilities to tackle challenges faced by next-generation PoC systems for molecular sensing.

In contrast with all prior work relying on passive platforms and the preliminary passive experiments, presented in Chapter 3, we leverage the monolithic nature of our platform to provide direct readout access from each ring sensor by connecting each MRR to an on-chip low noise receiver. Nanophotonic sensing and highly sensitive readout processing on the same die will not only eliminate the need for bulky and expensive off-chip equipment but will also provide accurate monitoring of each sensor and thus enable insight on sensing information from multiple rings at the same time.

Given the inherent sensitivity of MRRs towards fabrication tolerances and environmental fluctuations, biophotonic sensing systems need to ensure proper biasing of the ring and operation around a highly sensitive region of its Lorentzian spectrum. In order to achieve

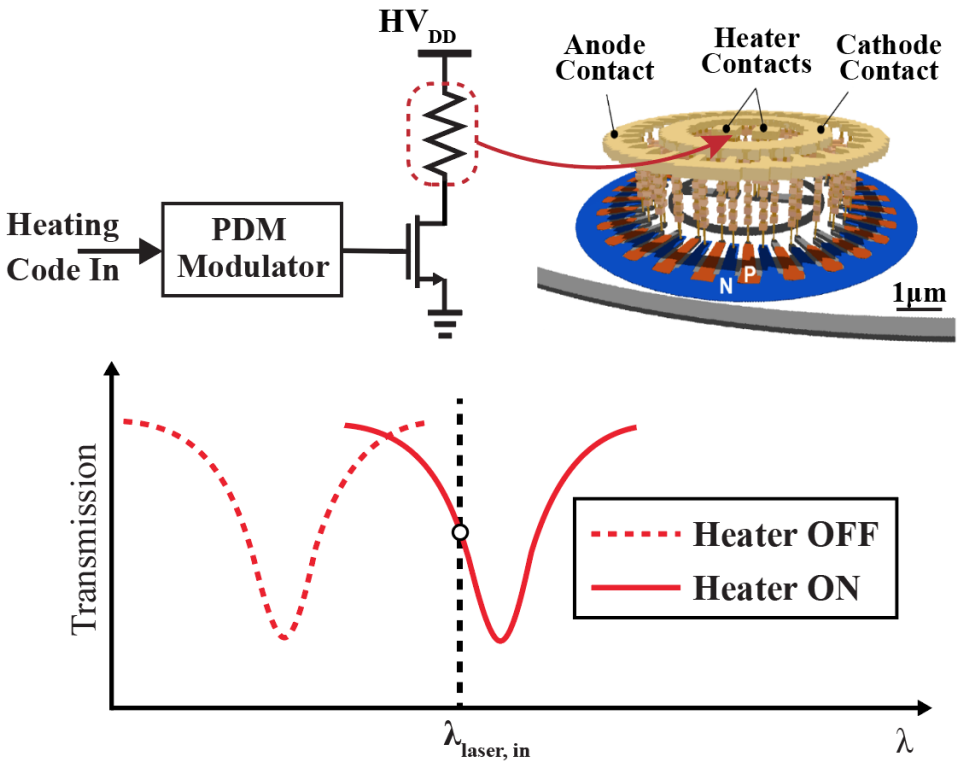

Figure 5.1: Active resonance tuning eliminates the need for a tunable laser, enabling the use of low-cost fixed wavelength light sources.

this, prior work is relying on sweeping a the wavelength of a tunable laser parked on the optimum slope. However, being able to move the ring instead of the laser would unlock the path towards single wavelength low cost laser diodes, eliminating the need for tunable lasers.

We leverage the inherent temperature dependence of the ring resonators and rely on the thermo-optic effect to actively control the ring's resonance utilizing heaters embedded within the internal cavity of the MRR, as illustrated in Fig. 5.1 [53]. The heater resistance controlled by on-chip electronics can actively tune the ring's resonance, enabling efficient resonance tuning. Additionally, on-chip feedback control loops can be wrapped around the ring sensor to ensure operation at a fixed bias point and hence a constant system's sensitivity during measurement.

Fixed wavelength sensing schemes, enabled by the active resonance tuning mechanism, offer key system-level advantages: (1) low cost and simple single wavelength or multi-wavelength laser diode chips [54] can now be used and ultimately co-packaged or bonded on the chip, dramatically reducing cost and form factor compared to implementations requiring a bulky and expensive tunable laser, (2) without the need to sweep the laser's wavelength, many measurement samples can be taken at a fixed ring bias point, offering the advantage of

significant averaging, thus enhancing the signal-to-noise ratio (SNR), and (3) a fixed wavelength multiple channel comb laser can be used, reducing system complexity and cost, while interrogating multiple rings simultaneously in a wavelength division multiplexing (WDM) sensing scheme.

Additionally, the µm-scale footprint of MRRs offers the advantage of creating densely packed arrays consisted of multiple MRRs. This enables the detection of multiple target molecules by functionalizing each ring with a different receptor, specific to a target antigen, as shown in Fig. 5.2. Therefore, by combining integration of multi-MRR electronic-photonic sensing arrays with the active resonance tuning capability, simultaneous and direct on-chip readout from multiple rings is enabled, thus unlocking the door toward multiplexed sensing of various biomarkers using low volume samples.

Using the MRR sensor as the unit transducer cell, various photonic architectures can be implemented, leveraging sensing information from both the amplitude and phase of the ring. Single WDM ring rows offer multiple sensing sites for amplitude detection by monitoring the power fluctuations inside each ring waveguide. However, detection of the ring's phase instead of amplitude can also be accomplished using RAMZI architectures, which rely on splitting and recombining light from two arms, as illustrated in Fig. 5.3. Therefore, various sensing schemes can be explored providing both simplicity and increased sensitivity.

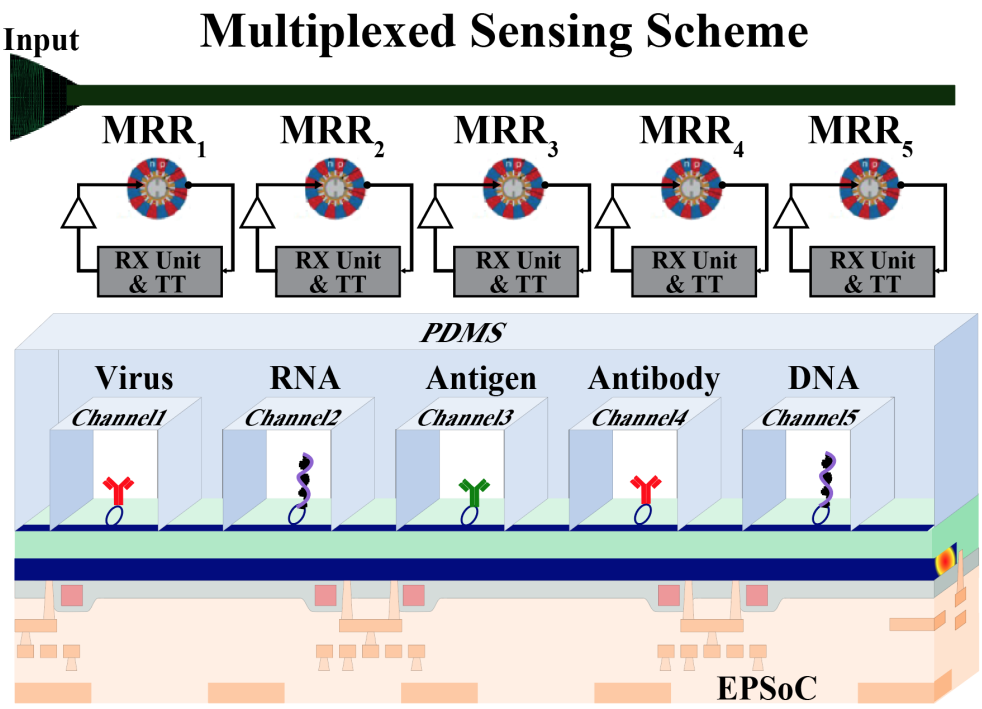

Figure 5.2: Interrogation of multiple rings enables simultaneous multi-molecular sensing of different types of analytes.

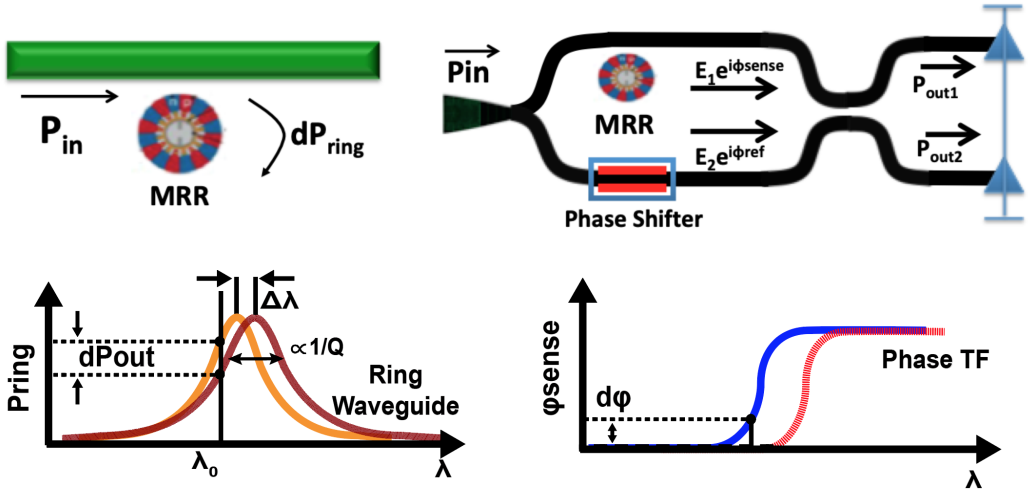

Figure 5.3: Using the MRR sensor as a unit transducer, amplitude and phase photonic schemes are implemented.

The dense integration of ring resonators into highly scalable arrays necessitates an efficient interface with fluidic solutions. The pitch of the ring sensors in the WDM rows is designed so that it facilitates alignment of multiple fluidic channels delivering simultaneously various samples to different ring sensors. As discussed in Chapter 4, the monolithic nature of the platform allows direct electrical coupling through the flipchip of the die on a PCB while the exposed surface enables access of optical fibers for coupling light. Therefore, the simplicity of simultaneous electrical and optical coupling without the need for wirebonding techniques, offers the additional advantage of creating enough space for microfluidic packages to land on-chip and deliver multiple low volume fluidic solutions.

Monolithic integration of on-die electronics with MRRs allows us to build a complete receiver unit right next to the ring sensors, and thus take a major step towards a miniaturized, self-contained LoC system by eliminating external read-out equipment.

Fig. 5.4 illustrates the architecture of the receiver unit, directly integrated with an on-chip MRR-PD. One of the key challenges we need to address is the ability to detect nA photocurrent changes induced from molecular binding events in a strong uA background photocurrent. We solve this problem by adding gain programmability to the receiver, amplifying the signal with a programmable gain transimpedance amplifier (TIA). This gain programmability, accomplished by using a digitally controlled large feedback resistance, offers a very wide sensor dynamic range and can be used to adjust between different sensing modes. Additionally, to avoid saturation of the receiver by the strong background photocurrent, which originates from the optical power circulating in the ring waveguide, current DACs are connected to the receiver input.

In order to provide a fully integrated readout processing system we digitize on-chip the

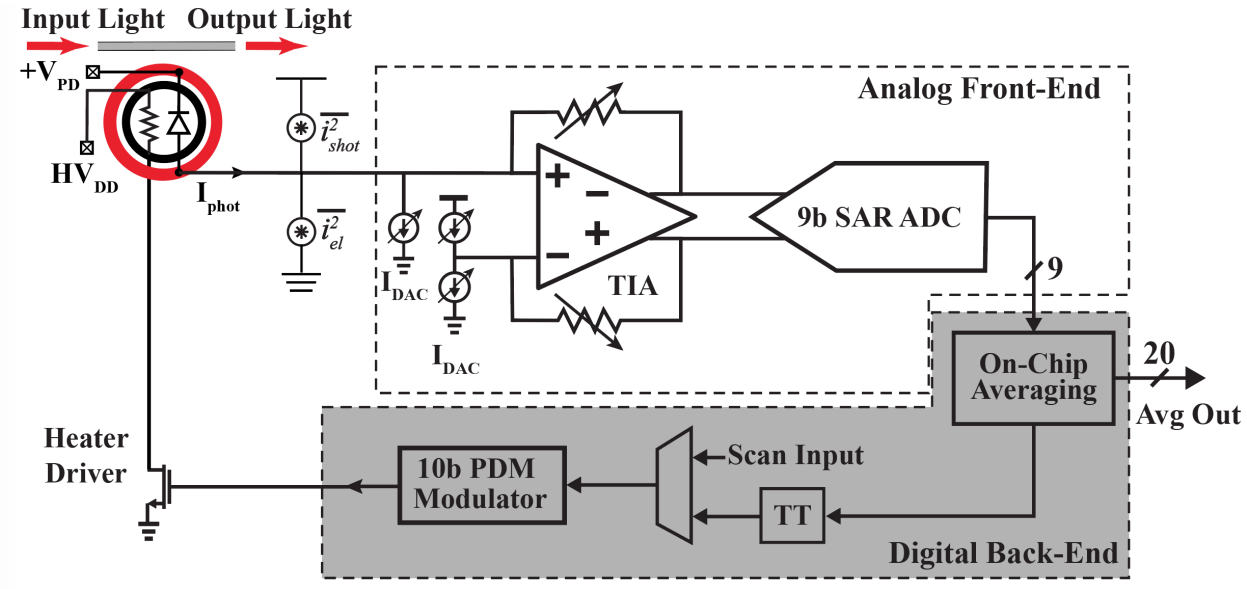

Figure 5.4: On-chip readout processing enables miniaturization of the LoC biosensing system.

analog information using a 9-bit SAR ADC operating at 50MSa/sec. The high sampling rate combined with on-chip digital back-end offers the additional advantage of averaging the digital output to further enhance the SNR, especially for low frequency applications.

The key architectural aspects introduced above, enable the design of highly scalable and versatile miniaturized LoC photonic systems. However, in order to better understand the key limitations of these photonic-based systems in respect with performance, and select optimal design strategies to address these challenges, it is necessary to examine the various noise sources and offsets which affect the LoD.

Figure 5.4 illustrates the main noise processes that exist in a single MRR-based receiver unit consisting of a ring sensor and an on-chip receiver. Several stochastic processes from the photonics and the circuit receiver, as well as ambient environmental fluctuations, contribute to the overall noise power, thus degrading the LoD. The shot noise i_{shot} from the photodetector and the electronic thermal noise from the receiver can be considered as white noise sources of the system, since lasers with sufficient performance [55] allow us to neglect relative intensity noise (RIN) and phase noise terms. Given the slow nature of molecular kinetics we can leverage the fixed wavelength scheme and the much higher speed of electronics to collect multiple measurements samples within a given time frame and perform significant averaging. This can significantly mitigate the effect of white noise sources resulting in flicker noise being the dominant electronic noise source.

However, ring resonators are inherently sensitive to environmental ambient variations such as temperature and pressure. The effect of the ambient fluctuations can severely degrade the sensing performance and become the dominant noise source of the system. Instead of relying on expensive solutions for controlling the ambient environment, we address this

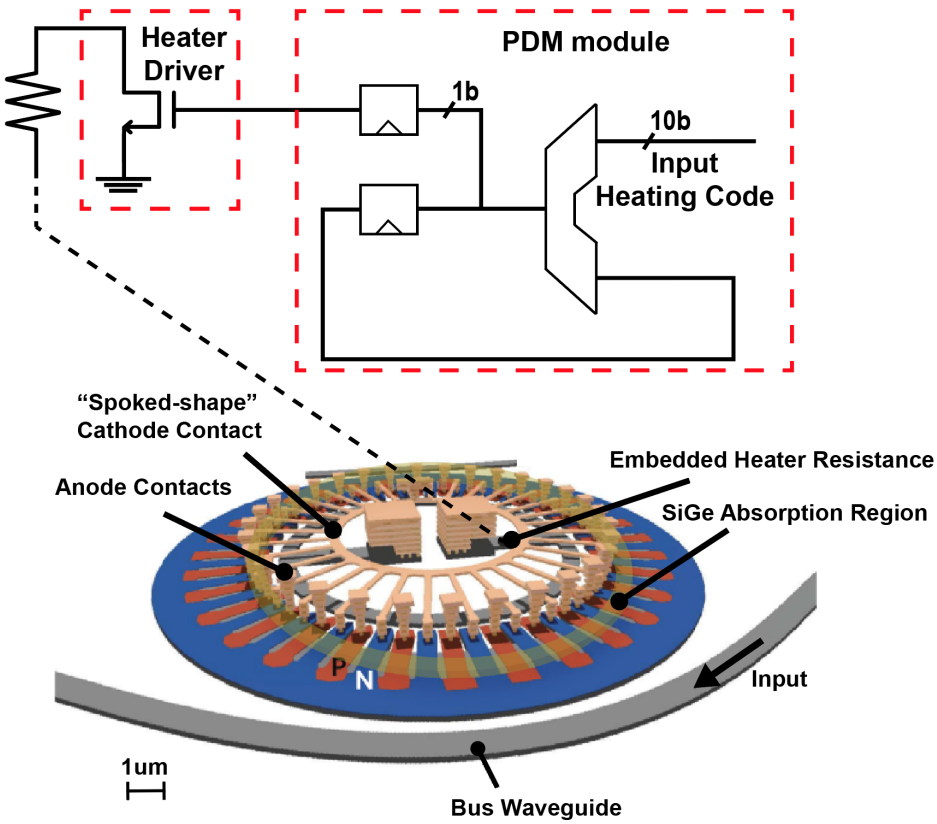

Figure 5.5: MRR-based photodetector in 45nm platform. An integrated heater embedded in the design of the ring eliminates the need for a tunable laser.

challenge by leveraging one of the key architectural features of the EPSoC. The ability to integrate multiple MRRs into highly scalable arrays offers a two-fold advantage: (a) it enables monitoring of multiple rings and therefore detection of various biomarkers and (b) each MRR sensor can be paired with another MRR structure acting as a reference structure in order to suppress ambient common mode errors. Therefore, by employing a differential readout scheme of a sensing and reference, we can suppress ambient fluctuations which appear as a common mode that can be subtracted in a differential measurement.

5.2 MRR-Based Photodetector with Embedded Heater

The structure of the MRR transducer in the zero-change 45nm RFSOI process is shown in Fig. 5.5. Its 5µm radius enables densely packed ring arrays for multi-analyte detection. Conversion of the optical power to the electrical domain is achieved with 30 interleaved pin

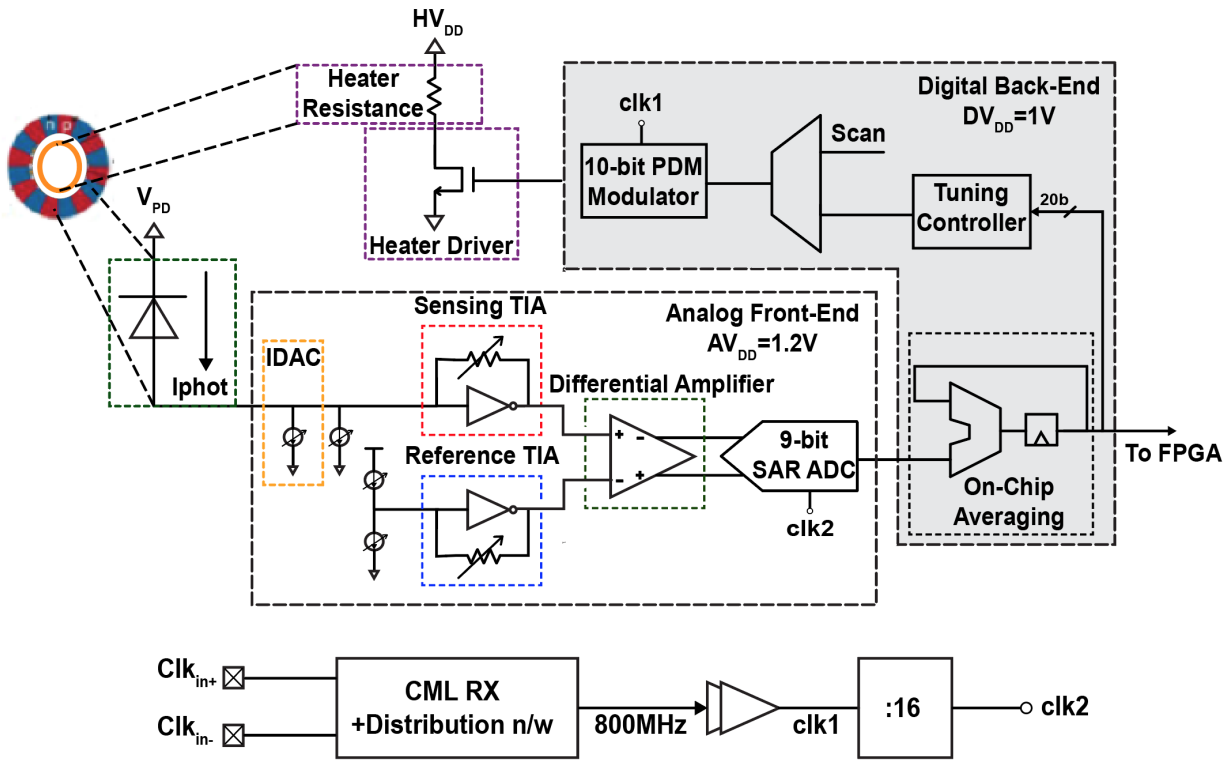

Figure 5.6: Architecture of the on-chip receiver. The photocurrent generated from MRR-PD is passed as an input to a pseudo-differential TIA. A post-amplifier converts the single ended output of the sensing TIA into a fully differential signal, digitized by a 9-bit SAR ADC. An on-chip tuning controller receives the averaged digital output and locks the MRR at the desired bias point.

diodes located along the perimeter of the ring cavity that fully deplete the ring waveguide from carriers. The p-n junctions use the same n and p-type implants as source/drain. Spokes of n and p-types are used to connect the p-n junctions with their respective contacts in the center of the ring. The responsivity of the MRR-based sensor is further enhanced with a doped SiGe strip that is responsible for carrier generation [56]. This enables the use of the same ring structure as both a biosensing transducer and a ring photodetector (PD) resulting in a simple scheme without the need of a separate sensor and PD.

An integrated heater resistance, located at close proximity to the ring cavity is embedded inside the MRR sensor. By leveraging the strong thermo-optic effect, the thermal power dissipated by the heater resistance selectively heats the ring waveguide, thus actively tuning its resonance and eliminating the need for a tunable laser. A 10-bit Pulse Duration Modulation (PDM) driver generates pulses at a 800MHz rate (Fig. 5.5). The heat pulses are then averaged by the low pass thermal response of the ring.

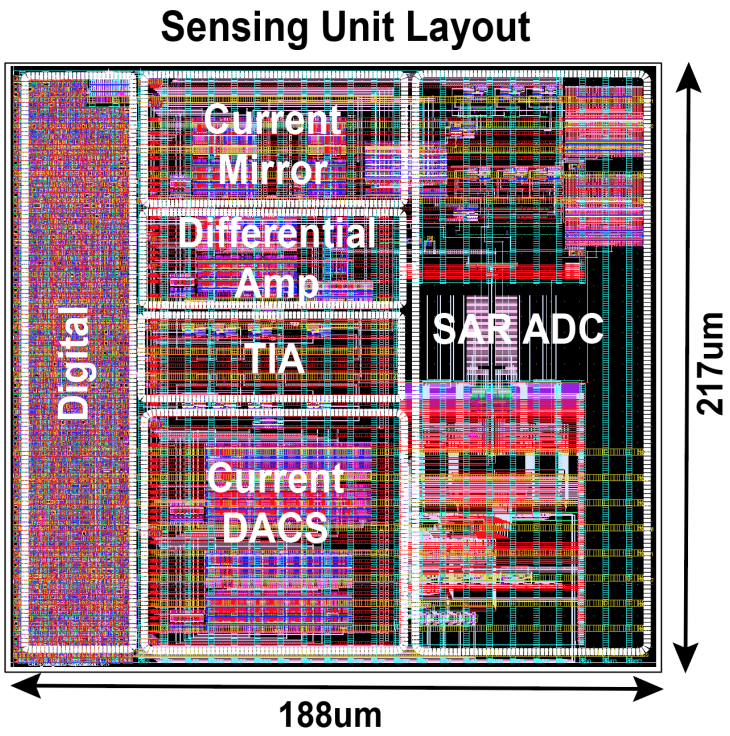

Figure 5.7: Layout of the on-chip receiver.

5.3 Sensing Circuitry

Co-integration of on-chip electronics and photonics on the same die eliminates the need for bulky and external readout equipment. The on-chip PD is connected in a reverse bias configuration to an on-chip sensing receiver and converts the optical power fluctuations – induced from molecular binding events – into a change in photocurrent. The strong background current originating from the optical power circulating in the ring requires a large dynamic range receiver capable of detecting small <10nA photocurrent changes at a large 1-100µA background signal. Therefore, gain programmability is needed in order to avoid saturation of the receiver and adjust between coarse and fine sensing modes of operation required for detecting a wide range of molecular concentrations.

The analog front-end (AFE) of the sensing receiver, illustrated in Fig. 5.6 is composed of a pseudo-differential shunt feedback Transimpedance Amplifier (TIA) followed by a fully differential postamplifier. A 9-bit asynchronous SAR ADC operating at 50MSa/s digitizes the signal. The relatively high sampling rate of the ADC compared to the slow nature of molecular kinetics offers the advantage of significant averaging. The ADC's output is averaged on-chip by 512 cycles in order to further enhance the SNR by mitigating the effect

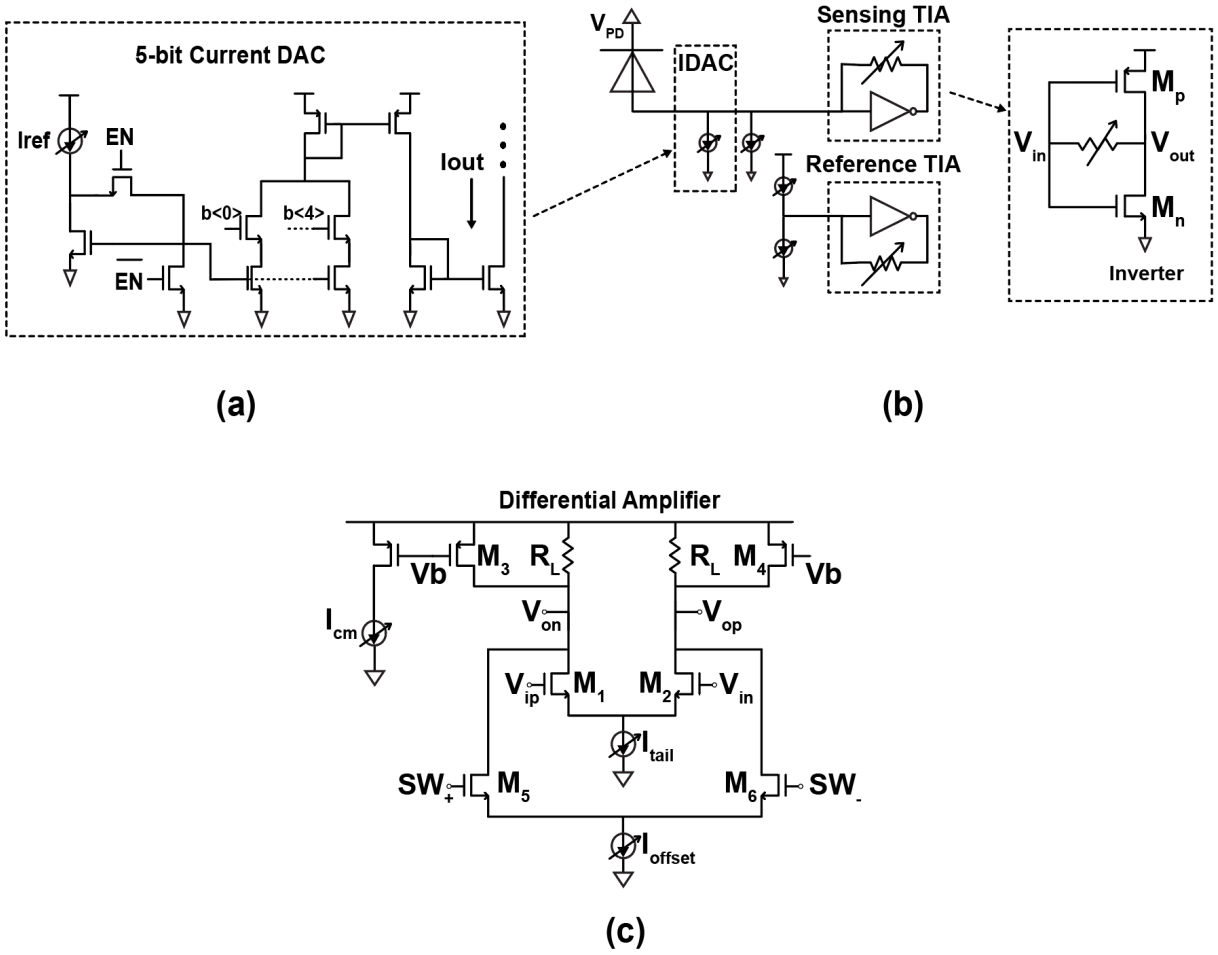

Figure 5.8: Circuit diagrams of (a) input current DAC, (b) shunt-feedback pseudo-differential TIA, and (c) fully differential post-amplifier.

of white noise sources and provide an averaged value to the on-chip tuning controller. The 10-bit PDM module receives the controller's output and based on the digital code selectively red or blue shifts the MRR. The clock path includes a CML receiver and a distribution network providing a 800MHz clock to the PDM logic. The clock signal is then divided by 16 times in order to provide a 50MHz clock to the SAR ADC. The reference currents for the AFE blocks are generated locally by a current mirror in each sensing receiver.

In order to suppress the large background photocurrent, input current DACs connected at the input of the receiver prevent saturation of the TIA. Specifically, this is achieved by a 5-bit coarse and a 5-bit fine current DAC connected at the input of the sensing TIA (Fig. 5.8a,b), cancelling a maximum bias photocurrent of ≈130µA and providing a 10-bit biasing resolution for the sensing TIA. The thermal noise current of the DACs is directly

referred at the input of the receiver, however it is strongly attenuated by on-chip averaging. Leveraging the input current DAC's dynamic range, we allow operation at high input optical power levels, therefore improving the SNR. However, increasing the optical power can reach a diminishing return due to self-heating effects which decrease the effective slope of the ring spectrum [57].

The first stage of the analog frontend is a pseudo-differential inverter-based shunt feedback TIA, as illustrated in Fig. 5.8b. A digitally controlled large feedback resistance (50k-800kΩ), enabled by monolithic integration, lowers the ADC quantization error and thermal noise floor, allowing the detection of nA current changes induced from single nanoparticle binding events while providing the required gain programmability of the receiver, necessary for wide dynamic range operation. A reference-dummy TIA in conjunction with a 3-bit push-pull current DAC connected at its input is used to provide a reference voltage for biasing a fully differential postamplifier, and also improves the Power Supply Rejection Ratio (PSRR) of the first stage pseudo-differential TIA. The single-ended (SE) output of the sensing TIA is converted to a differential signal by a fully differential amplifier (Fig. 5.8c). The PMOS transistors M_3 and M_4 adjust the amplifier's common mode output and a 3-bit offset current DAC corrects the amplifier's offset using NMOS transistors M_5 and M_6.

5.4 System Architecture

The µm-scale footprint of the MRR allows integration of multiple rings into densely packed arrays for multiplexed sensing of different analytes and repeated biosensing experiments. Figure 5.9 shows the overall architecture of the $5.5 \times 3\text{mm}^2$ arrayed EPSoC, consisting of 60 MRR sensors. The rings are arranged into 4 dual-row intensity and 2 phase-based sensing instances. Input laser light of a fixed wavelength is coupled to each instance through grating couplers. For two of the intensity-based instances, an on-chip Y-splitter splits the light into two rows of 5 MRR sensing units each. Each ring has a radius increment that sets the nominal resonant wavelength spacing of ≈100GHz in the O-band region.

5.4.1 Single MRR-PD Intensity Detection

In intensity-based detection schemes, the molecular binding events manifest as a change in the amplitude transfer function of the MRR, as described in Chapter 2. This results in a power fluctuation inside the ring waveguide which is indicative of the amount of molecular binding. The arrayed system-on-chip consists of two types of intensity-based schemes. In the first, a Si-Ge enhanced single ring (Fig. 5.10a) can act as both a biosensing transducer and a PD. This eliminates the need for a separate PD and reduces the complexity of the intensity scheme by requiring control of only one ring. However, this happens at the cost of a lower photonic sensitivity due to the limited Q of the MRR-PD.

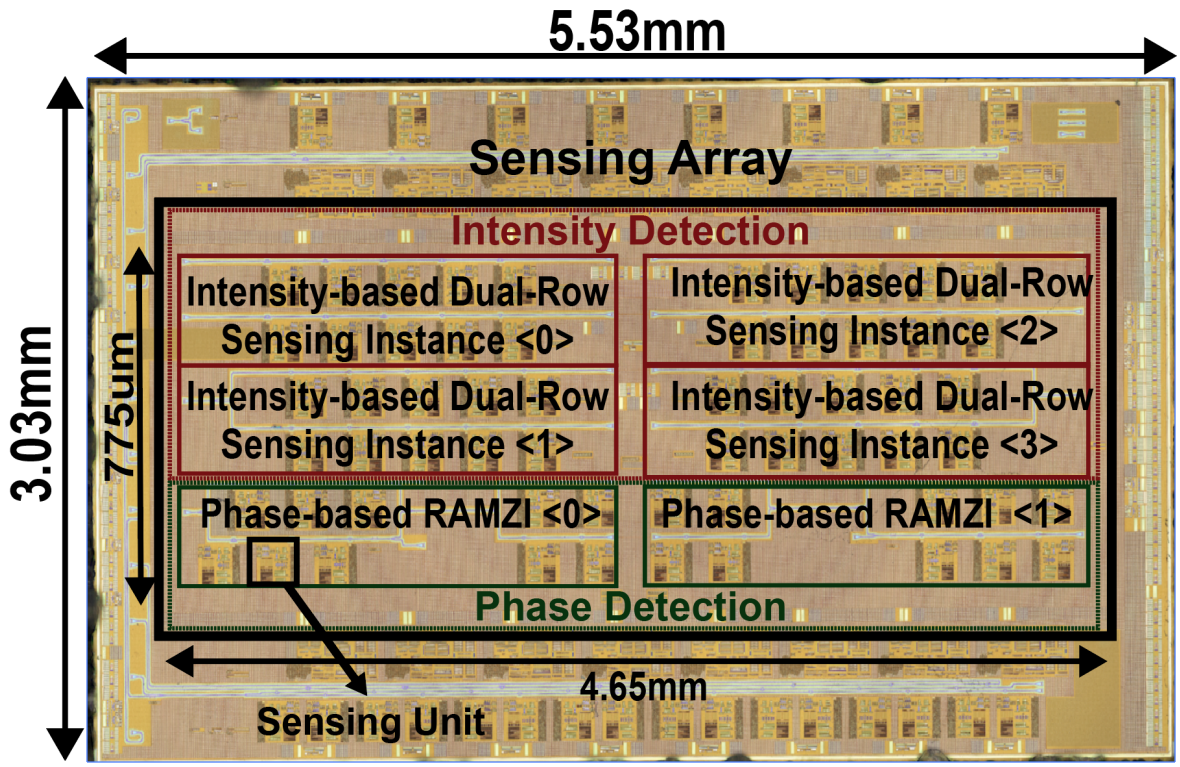

Figure 5.9: Architecture of the biosensing EPSoC. A total of 60 MRRs are arranged in intensity and phase-based sensing schemes, offering the advantage of multiplexed sensing and leveraging the amplitude and phase information of the rings.

5.4.2 Dual MRR Intensity-based Scheme

In order to circumvent this limitation and leverage higher quality factor MRRs, a dual-ring topology is also implemented. Figure 5.10b illustrates the sensing principle of this scheme. Power fluctuations dP_{hQ} at the thru-port of a higher Q biosensing ring – induced by molecular binding – are detected by an MRR-PD which acts only as a photodetector. This dual MRR architecture enables the use of ultra-high Q sensing rings [58] that can be interrogated by high responsivity PDs, thus enhancing the photonic sensitivity and the overall system's performance. However, the need to thermally stabilize two rings increases the level of complexity.

5.4.3 Ring Assisted Phase Detection Architecture

A resonant shift induced from molecular binding events results in a change in the amplitude and phase of the electric field of the MRR. As analyzed in Chapter 2, detecting phase instead of amplitude has received increased interest over the last decade due to its superior sensitivity

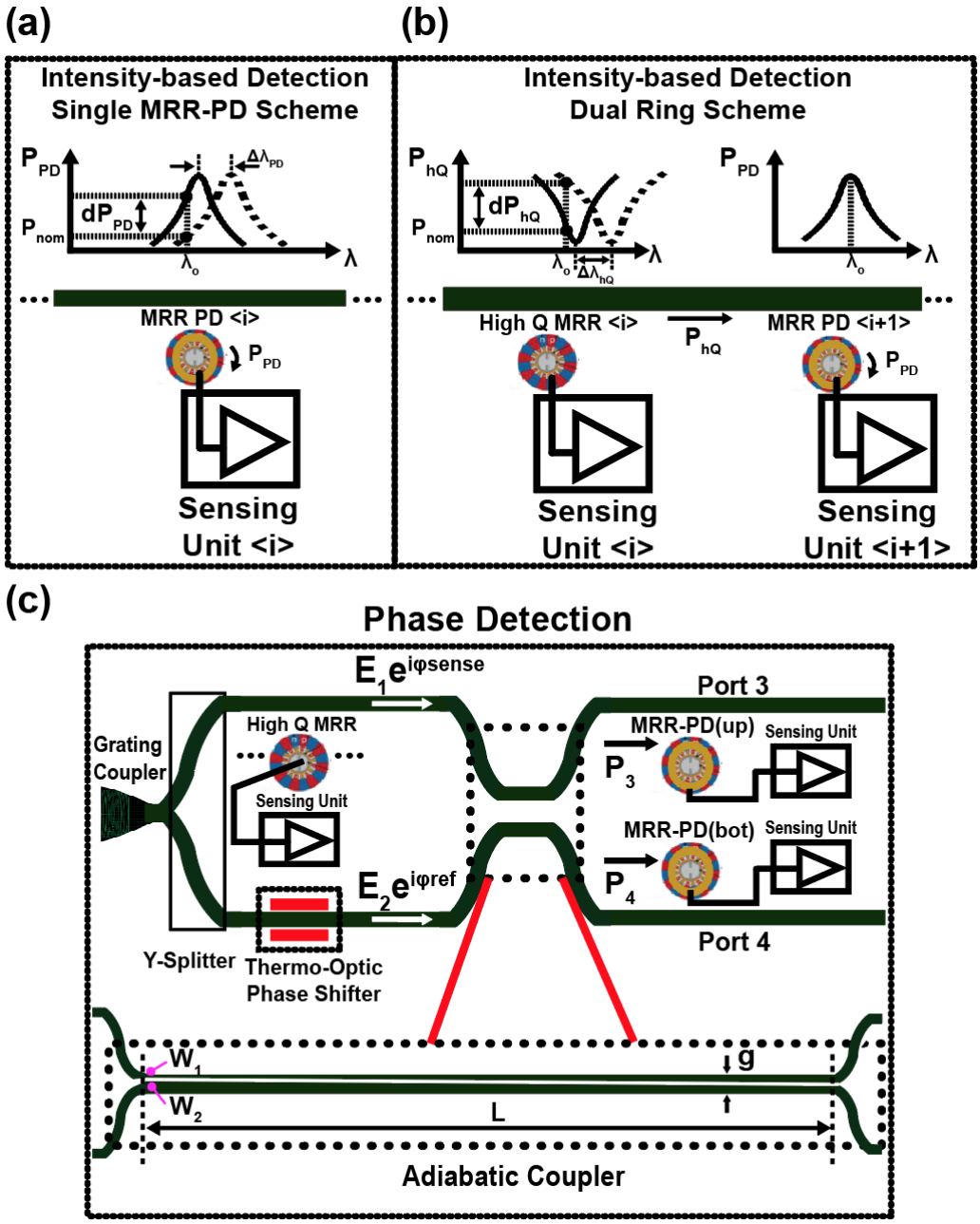

Figure 5.10: (a) Single MRR-PD intensity detection. A single MRR can be used as both a sensor and a photodetector, simplifying the complexity of the sensing scheme. (b) Dual-MRR intensity scheme. A high Q resonator - used as the sensing transducer - is interrogated by a separate MRR-PD. (c) Phase detection architecture of the Ring Assisted MZI.

compared to intensity based schemes [31–33]. In this chip, Ring-Assisted Mach Zhender Interferometer (RAMZI) phase detection architectures are implemented in order to further enhance the sensing performance of the EPSoC. In Fig. 5.10c, the topology of a RAMZI is shown. Light of a fixed wavelength is split into a reference arm and a sensing arm with high Q modulator MRRs. The electric fields E_1, E_2 of both arms are then recombined using an adiabatic 2x2 coupler [32]. The initial waveguide widths W_1, W_2 and tapering length L of the coupler are determined using mode solver simulations. The adiabatic coupling is implemented by two waveguides with initial widths W1 and W2, separated by 120nm. The gradual tapering of the waveguides over a length of ≈300µm results in maintaining the fundamental mode until the tapered waveguide becomes equal to 0.4µm. Parameters W_1, W_2, and L are determined using mode solver simulations. The optical power is then evenly divided in two output waveguides which are quickly separated. The output power at ports 3 (P_3) and 4 (P_4) can be written as:

$$P_3 = \frac{P_1}{2} + \frac{P_2}{2} + P_1 P_2 \cos(\phi_{sense} - \phi_{ref}) \tag{5.1}$$

$$P_4 = \frac{P_1}{2} + \frac{P_2}{2} - P_1 P_2 \cos(\phi_{sense} - \phi_{ref}), \tag{5.2}$$

where ϕ_{sense} and ϕ_{ref} are the phases of the biosensing ring and reference arm respectively and $P_1 = {E_1}^2$ and $P_2 = {E_1}^2$ are the optical power of the sensing and reference input waveguides. As observed, the RAMZI's single-ended output power expressions include both amplitude and phase related terms. By taking a differential measurement of (5.1) and (5.2) and leveraging the output power from both arms, the phase terms can be isolated as following:

$$P_{diff} = P_3 - P_4 = 2P_1 P_2 \cos(\phi_{sense} - \phi_{ref}) \tag{5.3}$$

The sensitivity of the RAMZI scheme is defined as the change of the differential power P_{diff} due to a resonant shift of the sensing ring. This can be written as:

$$\frac{\partial P_{diff}}{\partial \lambda_{res}} = 2\frac{\partial P_1}{\partial \lambda_{res}} P_2 \cos(\phi_{sense} - \phi_{ref}) - 2P_1 P_2 \sin(\phi_{sense} - \phi_{ref}) \frac{\partial \phi_{sense}}{\partial \lambda_{res}}. \tag{5.4}$$

Sensitivity is maximized at the quadrature point of the sine wave, where the phase slope $\frac{\partial \phi_{sense}}{\partial \lambda_{res}}$ dominates [33]. In order to ensure correct biasing of the RAMZI structure and operation near the quadrature point, a thermo-optic phase shifter, located in the reference arm, is used to optimize the reference phase offset. We convert the optical power at ports 3 and 4 into the electronic domain using two MRR photodetectors in the upper and bottom output arms. The differential measurement between the upper and bottom MRR-PD further enhances the scheme's sensitivity compared to a single-ended RAMZI operation. Overall, the proposed RAMZI structure offers a two-fold advantage: (a) the use of higher Q ring resonators as sensing rings (like in the dual-ring intensity scheme) and (b) the increased sensitivity of the photonic architecture due to phase instead of amplitude-based detection.

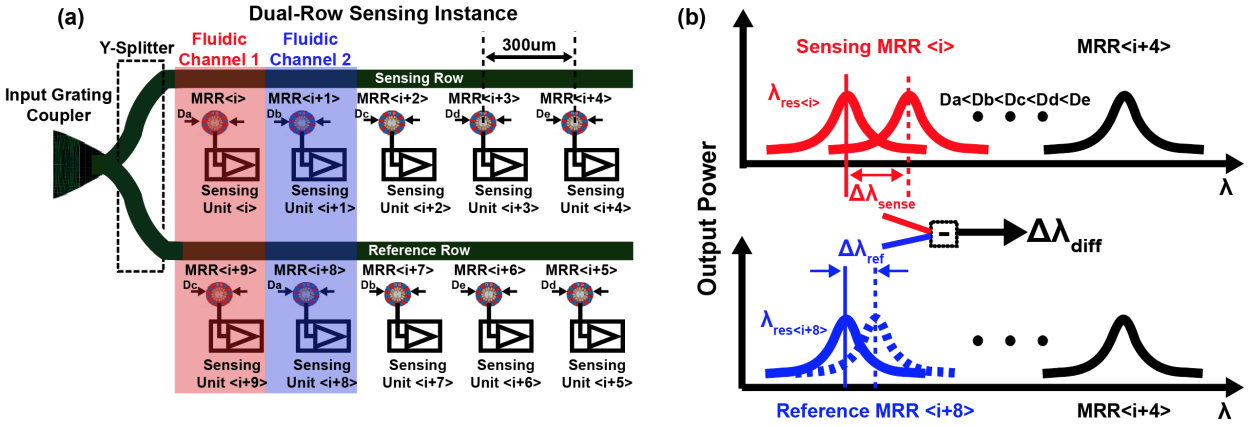

Figure 5.11: (a) Dual-Row Sensing Structure. (b) The reference shift is subtracted from the sensing signal, thus suppressing ambient common mode errors.

5.4.4 On-chip Common Mode Error Cancellation

Ring resonators are inherently sensitive to environment ambient variations, such as temperature ans pressure [59]. These sensitivities to fluctuations in the ambient environment, along with the non-specific binding events, cause erroneous signals to be detected. In order to cancel these interferers, each functionalized sensing ring is paired with a ring that acts as a reference structure. This results in ambient fluctuations and non-specific binding events to appear as a common mode signal to both the rings. Thus the differential response suppresses these interferers, isolating the signal induced from specific molecular binding events. In the system architecture of Fig. 5.11a, each dual row instance includes a sensing and a reference ring row. The top row consists of sensing rings to be functionalized with receptor molecules, whereas the bottom row provides reference ring structures for each of the sensors to cancel common mode offsets from the environment and non-specific binding.

The rings are physically separated by a 300µm pitch to facilitate high channel density microfluidic integration. Multiple channels enable simultaneous flow of target analyte solutions of different biomarkers. Additionally, they can allow low cost simultaneous in-channel functionalization of multiple rings with different biorecognition molecules, therefore eliminating the need for expensive micro-array spotters, which offer however higher spotting precision.

A reference MRR structure covered by a reference fluidic channel can be exposed to a reference solution, thus cancelling environmental common mode errors, as illustrated in Fig. 5.11b. However, in order to suppress non-specific binding and ensure more uniform fluidic environmental conditions, a reference MRR structure located inside the sensing fluidic channel can be exposed to the same target solution, thus canceling environmental variations and mitigating non-specific binding. As observed in Fig. 5.11a, the reference rings are interdigitated in the horizontal axis and not placed directly below their paired sensing MRRs in

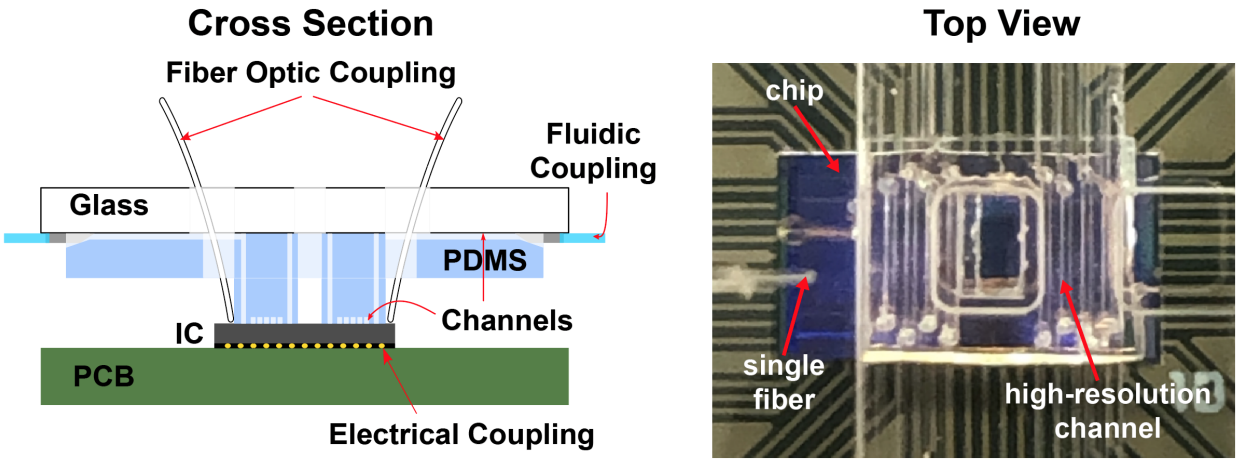

Figure 5.12: Simultaneous electronic-photonic and fluidic coupling using a co-packaged multi-channel microfluidic device fabricated with 3D printed molds. Single fibers couple light to the photonic array and flipchip of the silicon die on a PCB provides electrical coupling.

order to prevent contamination from functionalization solutions flowing vertically across the fluidic channels.

5.4.5 Electronic-Photonic and Fluidic Packaging

One of the key challenges towards efficient multiplexed sensing of different biomarkers in a silicon photonic platform is the simultaneous electronic, photonic and fluidic coupling. The flat surface needed in order to accommodate multiplexed microfluidic networks requires custom packaging techniques for the microfluidics [60] and large chip surfaces that significantly increase cost. Here, we address these challenges using (a) a multi-layer PDMS structure to interface with the small footprint of the silicon photonic chip and (b) a 3D printed transfer molding technique to create high resolution molds with densely packed channels down to <200µm spacing [61]. The fabricated microfluidic package is aligned and attached on the silicon-photonic die, as illustrated in Fig. 5.12, providing the capability to flow multiple solutions in parallel over the ring sensors. Single optical fibers couple light to the grating couplers of the photonic array. The fully integrated EPSoC is flipchip attached to an FR4 chip-board using 250µm pitch Cu pillars that provide electrical coupling, as shown in Fig. 5.12. This packaging technique offers unique advantages in multiplexed sensing arrays as it facilitates routing of multiple sensing signals, which remains a challenge in wirebond-based packaging required in systems using hybrid electronic-photonic integration. The chip-board is then plugged into a socket of a hostboard which provides regulated power and external connectivity.

5.5 Design Methodology

Design and implementation of complex EPSoCs with highly scalable multi-MRR arrays and on-chip electronics requires automation in generating and integrating electronic and photonic blocks. In this section, the design methodology and top-level integration for developing the biosensing EPSoC will be outlined, highlighting the key steps, required for building a highly parametrizable EPSoC.

5.5.1 Photonic Layout Generation

Unlocking the path towards multi-MRR biosensing applications necessitates a design workflow that enables scalability to systems with many optical devices and allows simple electronic-photonic integration. The development of the multi-MRR biosensing photonic array was enabled by the Berkeley Photonic Generator (BPG). BPG is a Python-based framework for the development of large-scale, customizable, and process-portable photonic integrated circuit generators. These generators include parameterized design methodologies for producing layouts, schematics, and testbenches.

One of the critical aspects of building a complex electronic-photonic system is adopting a design hierarchy which allows scalability and parametrization. The photonic array is implemented separately from electronic blocks. In Fig. 5.13a the levels of hierarchy of the photonic array layout are illustrated. Starting from a fully parametrizable sensing MRR unit cell, a row of multiple MRR cells – separated by a certain pitch – can be designed as a new module. In order to allow design flexibility, different ring variants can be created by passing as parameters into the core ring function the radius and doping information. Therefore, MRRs of different radii and doping regions can easily be created by selecting the desired parameters, resulting in different ring variants used as high quality factor biosensing structures or ring photodetectors in WDM ring rows. Additionally, other photonic blocks such as grating couplers are designed as separate cells, enabling the design of ring rows with input and output grating couplers for coupling light.

The ring row module receives as parameters the number of MRRs, the type of ring variants and the ring pitch. This enables the design of multi-MRR ring rows consisted of rings from different variants and separated by a desired pitch, which facilitates alignment of multi-channel microfluidics of a certain fluidic channel pitch. As described in Sections 5.4.1-5.4.3, different photonic amplitude-based sensing schemes can be developed. Ring rows of only MRR-PDs provide multiple singe-ring sensing sites, whereas mixed rows of ring modulators interrogated by MRR-PDs offer the additional advantage of higher Q rings used as biosensors. By combining ring row modules, a waveguide-based thermo-optic phase shifter and an adiabatic coupler unit cell, we create a phase-based RAMZI module.

The photonic sensing system consists of amplitude and phase-based structures. Single ring rows of different variants provide amplitude detection, where as RAMZI structures enable phase detection. To implement the photonic array, a top-level generator instantiates the desired number of different ring row modules and RAMZI, as illustrated in Fig. 5.13b.

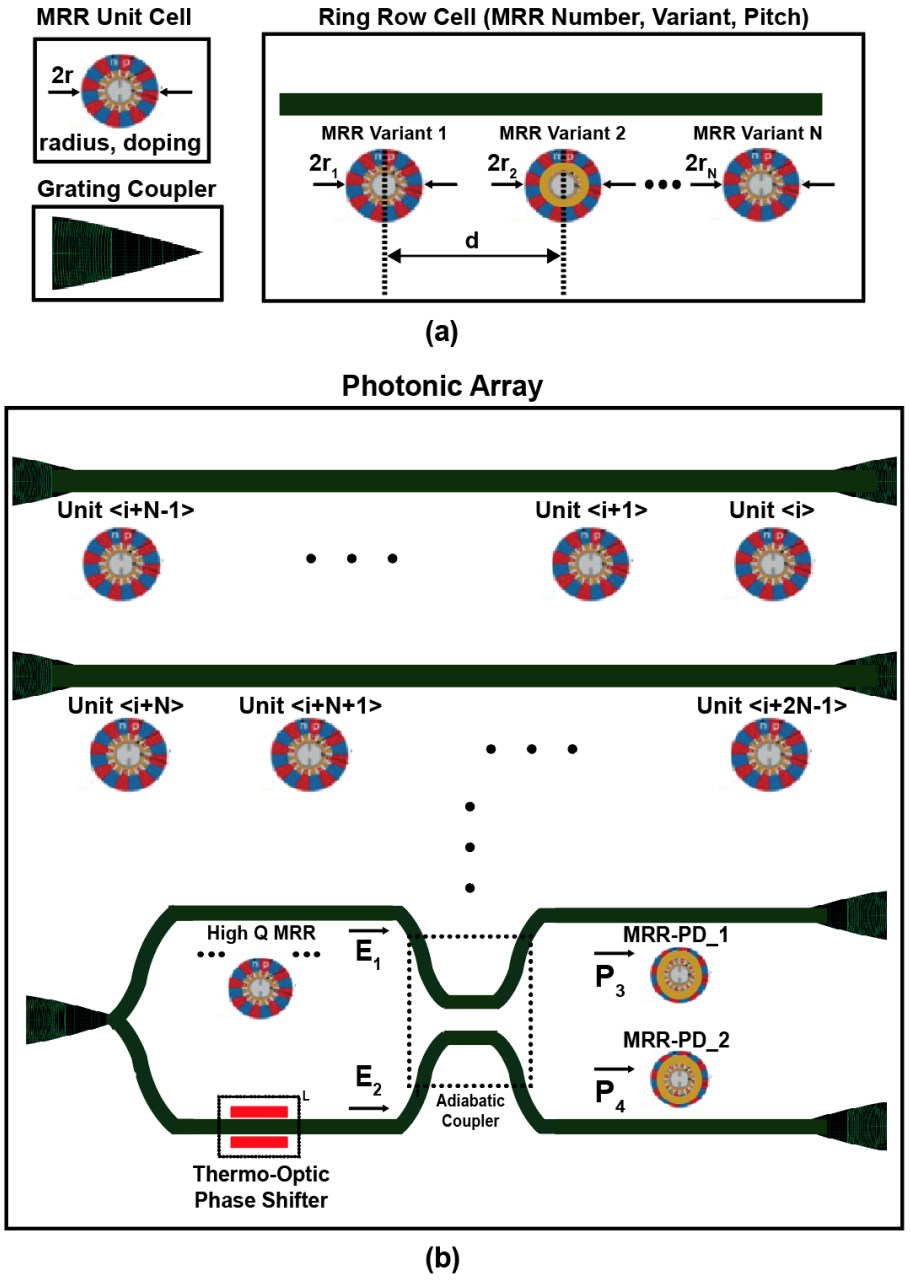

Figure 5.13: (a) Using a python-based framework for the photonics layout generation, a row of multiple parametrizable MRR cells can be designed. (b) A photonic array comprised of amplitude-based ring rows and phase detection structures is generated.

After developing the photonic array using BPG, the design is imported in Cadence Virtuoso and a LEF file is extracted, including the pins of the anodes, cathodes and heaters of the

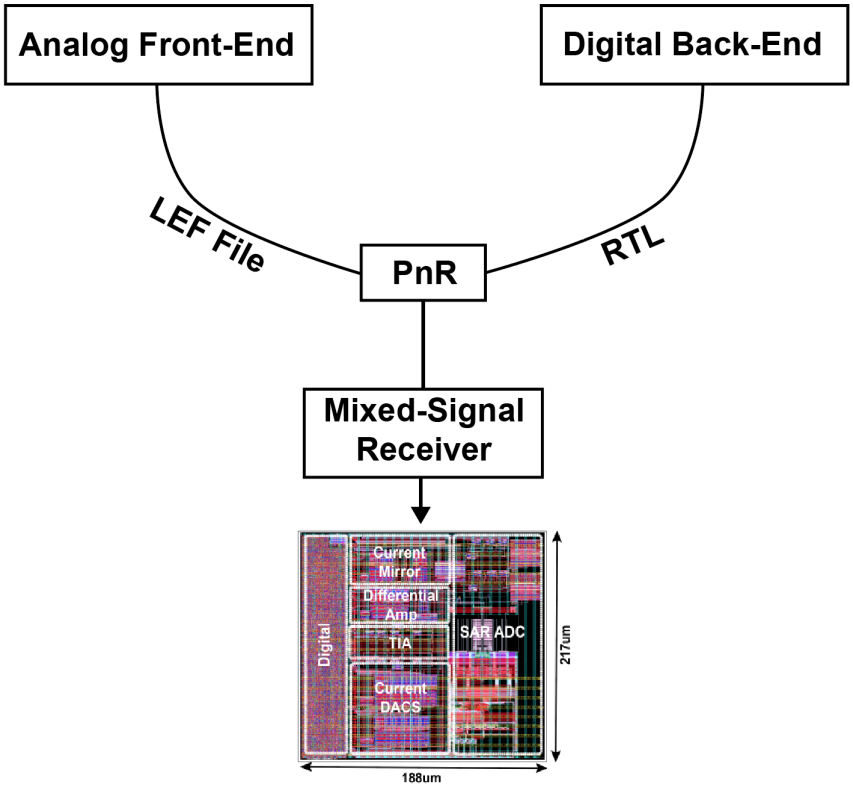

Figure 5.14: The on-chip electronic receiver consists of an Analog Front-End (AFE) and a digital Back-End. After generating the AFE blocks and extracting LEF files, a mixed-signal receiver block is designed using the standard flow of digital synthesis and place-and-route in Innovus.

rings.

5.5.2 Electronic-Photonic Top-Level Integration

The on-chip electronic receiver consists of the Analog Front-End (AFE) and the digital Back-End (Fig. 5.7). The electronic AFE blocks are implemented using BAG generators [62], thus allowing fast layout generation and multiple design iterations. After extracting a LEF file for the AFE, a mixed-signal receiver block comprised of the AFE and digital back-end is designed using the standard flow of digital synthesis and place and route in Innovus. After the design is DRC and LVS clean, a LEF file is extracted from the final mixed-signal receiver block which will be repeated multiple times in order to create an electronic receiver array interfacing with the multi-MRR photonic system, as shown in Fig. 5.14.

After designing the photonic array and the mixed-signal receiver block, we floorplan the electronic-photonic SoC by setting the location of the different modules. The receivers are

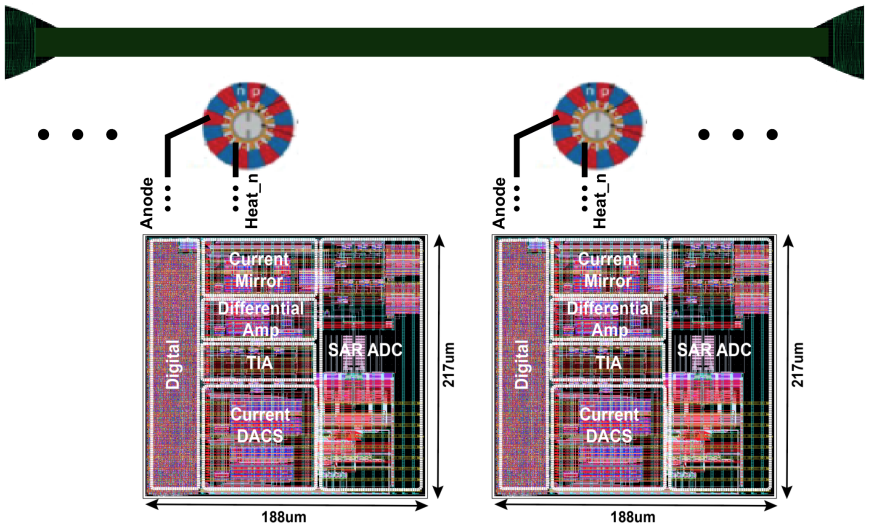

Figure 5.15: The receivers are placed at the same pitch as the rings of the array in order to ensure physical contact with the photonics by overlapping the two layouts

placed at the same pitch as the rings of the array in order to ensure physical contact with the photonics by overlapping the two layouts (Fig. 5.15). The photonic array module, described by its LEF file, is then instantiated at a pre-calculated location that ensures complete alignment and DRC-Clean contact with the I/O pins of the receivers. Any misalignment between rings and receivers will appear as an LVS error. The design is pushed into place and route and this procedure is iterated until the electronic-photonic system is DRC and LVS clean.

5.5.3 Board Design

The fully integrated electronic-photonic die is flipchipped on a chipboard illustrated in Fig. 5.16. The 250µm pitch of the chip bumps needs to be aligned with the pads on the board. Therefore, the chipboard has a 11x21 pad array and the signal mapping for each pad is determined by the corresponding bump of the die, once flipchipped. The board has 8 layers and we allocate each layer to a power signal. The pads of the array are routed at multiple layers and connect to outer pins of the board, as shown in Fig. 5.16. Via-in-pads are used in order to connect a chip bump to a board pad and route it at an intermediate layer.

The chipboard is plugged on a PGA socket of a hostboard, shown in Fig. 5.17. The PGA socket has 289 pins from which only 231 are used based on the number of chipboard pins. The hostboard has decoupling capacitances of multiple values located close to the socket and connected to the power supplies of the design. A 3.3V external supply powers multiple LDOs in the board, which provide regulated power supplies to the chip.

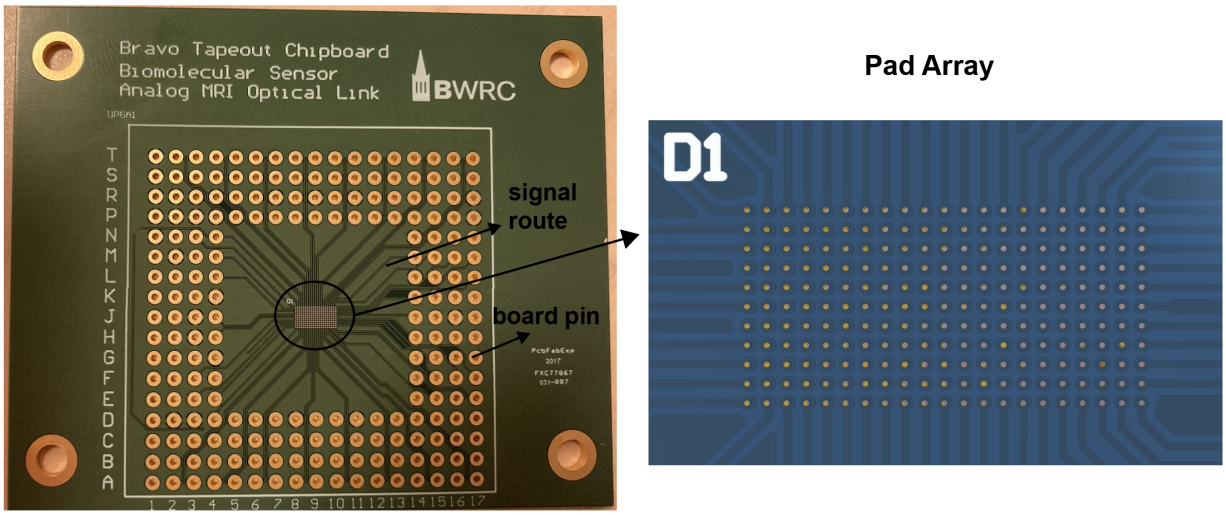

Figure 5.16: Chipboard design. The die is flipchipped on a 11x21 pad array on the board. Signals are routed to outer pins of the board at intermediate plane layers.

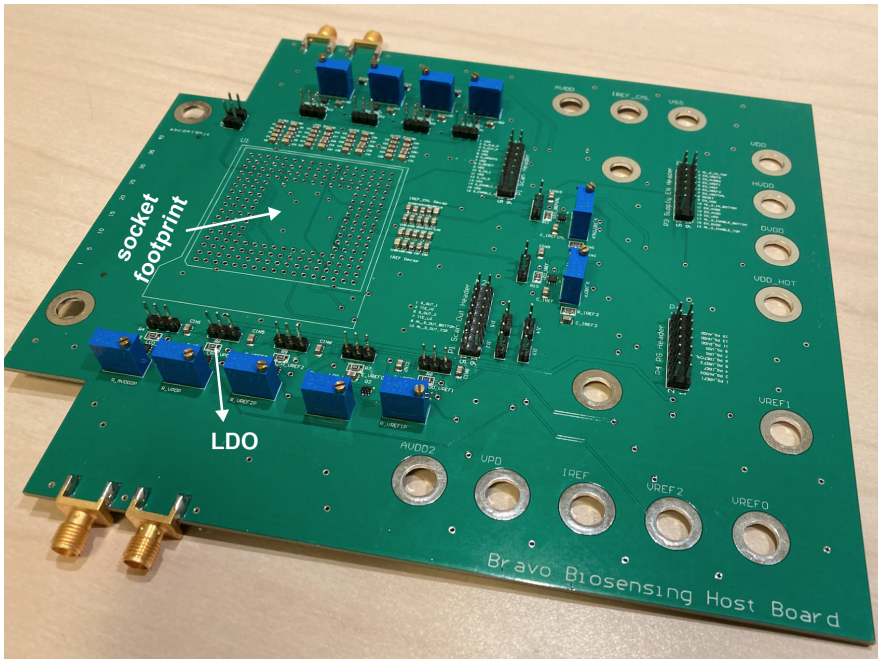

Figure 5.17: The chipboard is plugged on a hostboard, which provides regulated supplies to the chip using LDOs.

5.6 Summary

We introduced a first of its class fully integrate electronic photonic SoC for label-free molecular sensing. Co-integration of µm-scale MRRs with on-chip electronics on the same die

unlocks the path towards highly miniaturized self-contained photonic biosensors for PoC. In this section, we presented a brief overview of the key architectural features of the system that enable critical sensing capabilities and we identified the main noise sources of the system. Next, we analyzed the basic sensing unit cell which consists of a ring sensor connected to an on-chip receiver. The ring structure in 45nm process has an integrated heater resistance embedded in the design of the ring. Leveraging an active resonance tuning mechanism, enabled by on-chip control electronics, we eliminate the need for a tunable laser and pave the path towards the use of single wavelength laser diodes which can ultimately be co-packaged in the LoC platform. We then analyzed the readout sensing circuitry and discussed the design choices to meet both the noise requirements and the wide input current Dynamic Range originating from the strong background photocurrent of the MRR. The system architecture was then presented, analyzing the various photonic sensing schemes which rely on amplitude and phase detection. Starting from the simple single MRR-PD amplitude scheme, we introduced more sensitive sensing architectures by utilizing higher Q rings in dual-MRR schemes and combining them with RAMZI phase structures detecting phase instead of amplitude changes. To address the inherent variabilities of MRR towards environmental fluctuations, we introduced a differential readout scheme, comprised of sensing and reference ring sensors to subtract common-mode errors. Next, we presented the packaging strategy providing simultaneous electronic, photonic and fluidic coupling and finally we described the design methodology in order to design and integrate this EPSoC and discussed the board design interface.

Chapter 6

Measurement Results

In this section, we evaluate the sensing performance of the fully integrated EPSoC. We initially characterize the performance of the on-chip receiver and the MRR-based sensing schemes without any bio-samples. This allows us to extract and optimize the effective electronic-photonic sensitivity, and examine the system's performance in order to determine the *LoD*. To evaluate the biosensing performance, we demonstrate real-time kinetics of anti-BSA, BSA and 150nm streptavidin-coated nanoparticles. In all experiments, fixed wavelength laser light is coupled onto the chip from a standard single-mode optical fiber through the vertical grating couplers. Kinetics between biotin and streptavidin are monitored as a first proof of concept. In a second experiment, after activating the surface with a layer of glutaraldehyde, real-time kinetics of anti-BSA are first detected and the binding events between BSA and anti-BSA are then monitored in real-time. In all experiments, a laser light of 1300nm is used, coupling light to the grating couplers of the chip through a single mode optical fiber.

6.1 Electronic-Photonic Performance

6.1.1 Electronic Characterization

As a first step, we characterize the performance of the on-chip receiver. Figure 6.1a shows the dc characteristic of the receiver at a TIA gain of 50kΩ. This is obtained by sweeping the digital code of the fine current DAC, thus creating incremental current changes at the input of the receiver. Using the simulated gain of the post-amplifier, the DNL of the SAR ADC can be characterized for each current DAC step (Fig. 6.1b), which creates an incremental change of ≈12mV at the SAR's input. We then evaluate the noise performance of the receiver by monitoring the ADC's output at a fixed input current DAC code. For clinically relevant molecular concentrations in the fM and pM regime, binding events can occur on the order of a minute. By leveraging the slow nature of molecular kinetics, the *LoD* can be lowered with further off-chip post averaging, enabled by the 50ms readout sampling rate. The contribution

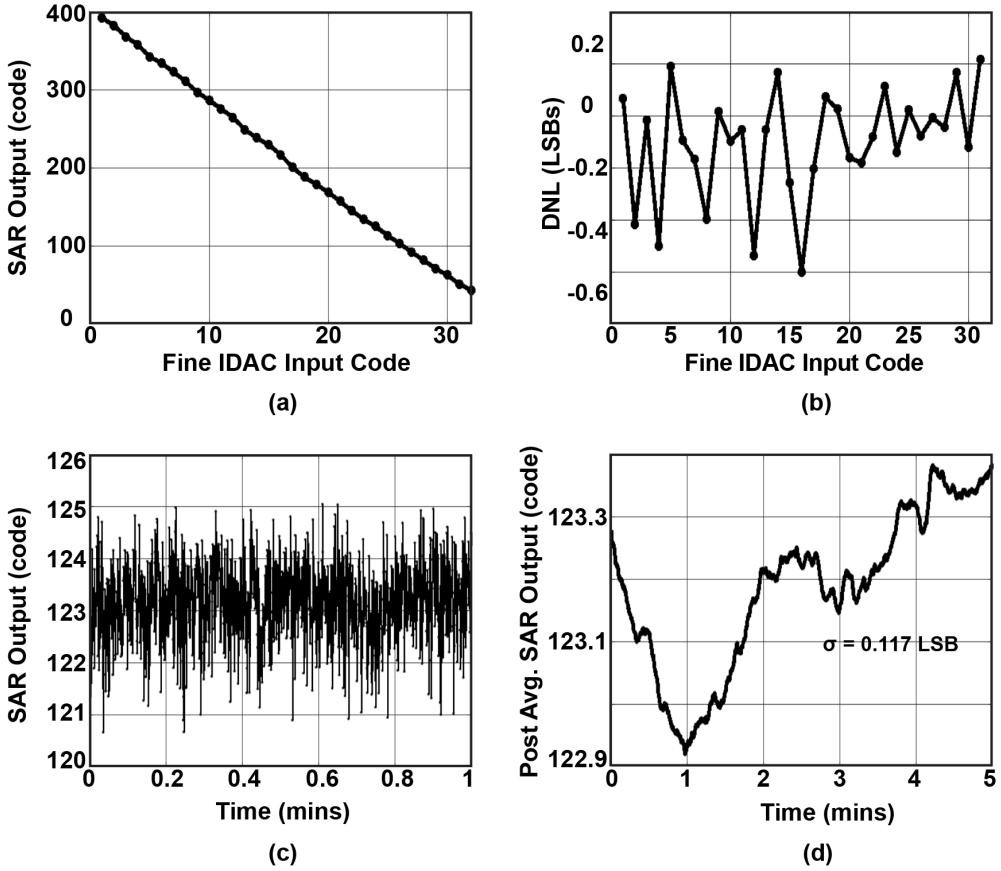

Figure 6.1: Electronic Characterization of the receiver. (a) SAR dc characteristic. (b) Extracted DNL. (c) On-chip averaged SAR output at 400kΩ TIA gain. (d) Post averaged output.

of white noise sources is therefore significantly decreased, resulting in an averaged output that is mostly dominated by flicker noise. Fig. 6.1c shows the on-chip averaged SAR output at a TIA gain of 400kΩ and a fixed input DAC code. After applying a moving average window of 1 minute, the post averaged output, shown in Fig. 6.1d., results in a standard deviation (σ) of 0.117 LSB. Dividing by the gain of the receiver results in a σ in input current of 170pA. This minimum detectable current combined with the maximum current detected at 50kΩ, results in an 85dB dynamic range. The power dissipation from each receiver unit is ≈3.4mW. The analog front-end consumes ≈2.7mW, while the digital back-end and the integrated heater dissipate ≈0.5mW and ≈0.2mW respectively.

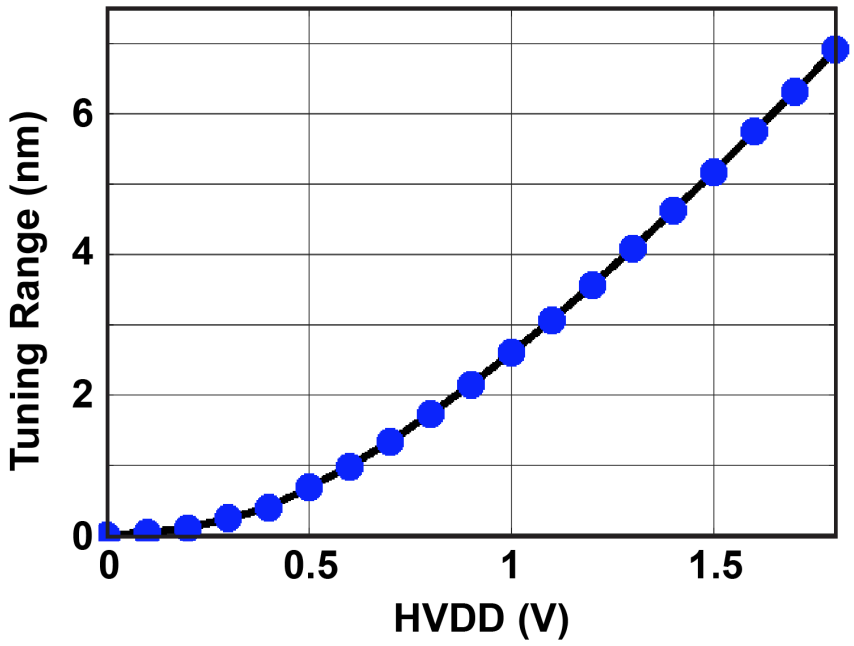

Figure 6.2: Tuning range of the integrated heater at full-scale operation.

6.1.2 Single MRR-PD Lorentzian Spectrum

We convert the optical power into the electronic domain using on-chip reverse-biased single MRR-PDs, with a maximum responsivity of $0.2\frac{A}{W}$. The photocurrent generated by the MRR-PD is then passed as an input to the on-chip receiver.

We first evaluate the overall electronic-photonic performance of single ring-based PDs by characterizing the Lorentzian spectrum of the MRR device using the on-chip receiver. Figure 6.3a shows the ring spectrum of a MRR-PD at different TIA gains and a fixed wavelength. Instead of tuning the laser to obtain the Lorentzian shape of the ring, we tune the ring's resonance by sweeping the input heating code of the PDM driver by an LSB step within a range of 200 codes. Based on the maximum tuning range at $HV_{\mathrm{DD}} = 1.1V$ and the 10-bit resolution, each heating step corresponds to a step of 3pm, as shown in Fig. 6.2, resulting in an equivalent wavelength sweep of 600pm.

The gain programmability of the receiver allows an increase of the Lorentzian slope. By taking the derivative of each ring spectrum over the stable, blue side of resonance, an effective electronic photonic sensitivity can be established, as illustrated in Fig. 6.3b. This sensitivity term depends on the power incident to the ring, the MRR's quality factor, the responsivity of the ring PD and the receiver's gain. Specifically, we can write:

$$S_{eff} = \frac{\partial V_{out}}{\partial shift} \approx S_{phot} R_{PD} Gain_{RX}, \tag{6.1}$$

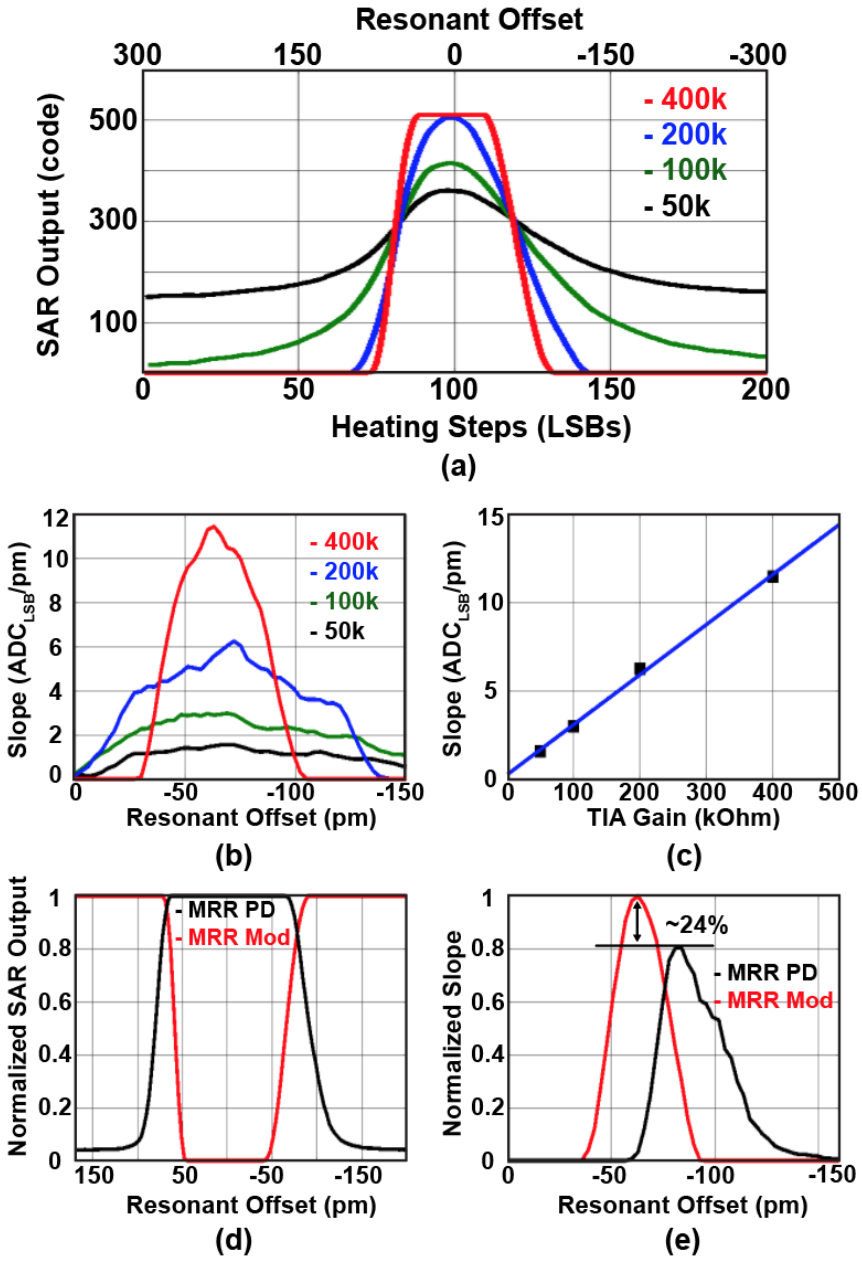

Figure 6.3: (a) Lorentzian spectrum of a single MRR-PD for different TIA gains. (b) Slope of the ring spectrum for different TIA gains. (c) Electronic-photonic sensitivity versus TIA gain. (d) Ring spectrum of the higher-Q sensing/modulator MRR and the interrogating MRR-PD. (e) Lorentzian slope of the higher-Q modulator/sensing MRR and MRR-PD. A 24% increase in sensitivity is observed.

where V_{out} is the receiver's output voltage signal and can be expressed in LSB units, S_{phot} is given by eq. (2.9), R_{PD} is the MRR-PD's responsivity and $Gain_{RX}$ is the gain of the receiver.

In this experiment, an input power of ≈-13 dBm is applied. The linear dependence of the maximum effective slope on the TIA's gain is presented in Fig. 6.3c.

6.1.3 Dual-MRR Demonstration

In order to leverage higher Q rings, a dual ring scheme is needed. In this detection mechanism, we use a separate non SiGe-doped lower-loss MRR modulator acting as the sensor and an MRR-PD used only as a photodetector. In order to examine the performance of the dual ring scheme, the tuning heater of a ring modulator sweeps its resonance and the power fluctuations of the thru port are captured by the receiver of an MRR-PD which has its resonance located on the laser's wavelength. Figures 6.3d,e show the Lorentzian spectrum and the effective sensitivity of a non-SiGe doped MRR modulator and a ring PD. A 24% increase in sensitivity is observed which results from the higher Q of the MRR modulator. This detection mechanism unlocks the path toward the use of up to 200k Q rings, previously shown in this platform [58], thus enhancing the system's sensitivity by at least an order of magnitude compared to 12k-18k Q MRRs measured in this chip.

6.1.4 Phase-Based Scheme Characterization

In order to further improve the system's sensitivity, we explore phase detection by implementing ring-assisted MZI structures.

The RAMZI single-ended output power expressions, given by (5.1),(5.2), includes both amplitude and phase related terms. The optimal sensitivity is obtained by operating the RAMZI structure at the quadrature point of the cosine wave, where ideally both output arms have the same intensity [33]. To allow tuning of the reference phase shift and enable optimal biasing of the RAMZI structure, a reference phase offset is introduced using a waveguide-based heater located at one of the input arms. By sweeping the heating code of the waveguide-based thermo-optic phase shifter, the optimal sensitivity point can be selected at the quadrature point of the sine wave in order to maximize the photonic sensitivity.

The improved performance of phase-based sensing is illustrated in Fig. 6.4a, where the sensitivity of the RAMZI's differential response is 49% higher compared to the slope of the MRR's amplitude spectrum. In the design implemented in this work, the optical power is further split for monitoring purposes before entering the adiabatic coupler, resulting in an extra 3dB power loss which is not fundamentally required in a RAMZI-based scheme. Therefore, the differential phase-based architecture can be up to ≈$x3$ more sensitive compared to intensity-based sensing with a ring modulator and $x3.7$ more sensitive compared to a single MRR-PD by benefiting from the higher quality factor of an MRR modulator.

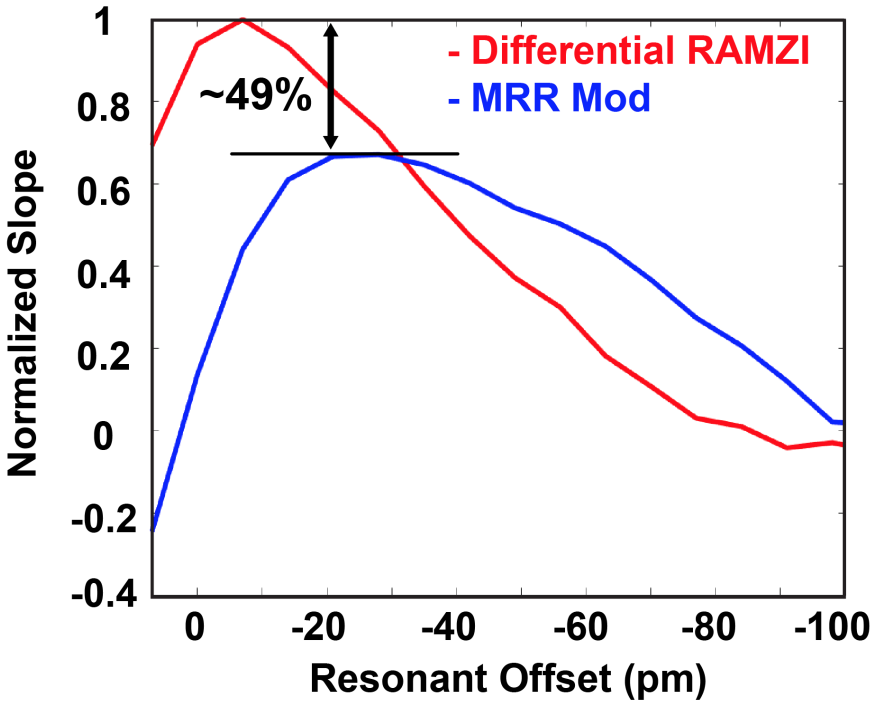

Figure 6.4: Phase detection RAMZI characterization. Measured sensitivity comparison between optimal differential RAMZI output and intensity based detection of the MRR modulator. A 49% enhancement is observed.

6.1.5 On-chip Tuning Controller

By leveraging the in-ring integrated heater, we implement an on-chip tuning controller that automatically locks the ring at a user-defined bias point of the Lorentzian spectrum. The on-chip tuning mechanism offers the additional benefit of re-locking the ring at its nominal point when large bulk RI changes introduce offsets. After pre-characterizing the Lorentzian spectrum of the MRR and selecting the desired bias point (Fig. 6.5a), the controller is enabled and locks the ring, as shown in Fig. 6.5b. Starting from off resonance, the integrated heater blue-shifts the Lorentzian spectrum at a scanning step selected by the user. Once the desired bias point of the Lorentzian is detected, the controller enters the locking mode in which the ring is locked within an LSB heater precision, as shown in Fig. 6.5c. In addition to the ring's locking, we verify the functionality of the controller by introducing ambient heating events. As illustrated in Fig. 6.5d, the tuning controller adjusts the heating code of the PDM driver and cancels the ambient-induced shift.

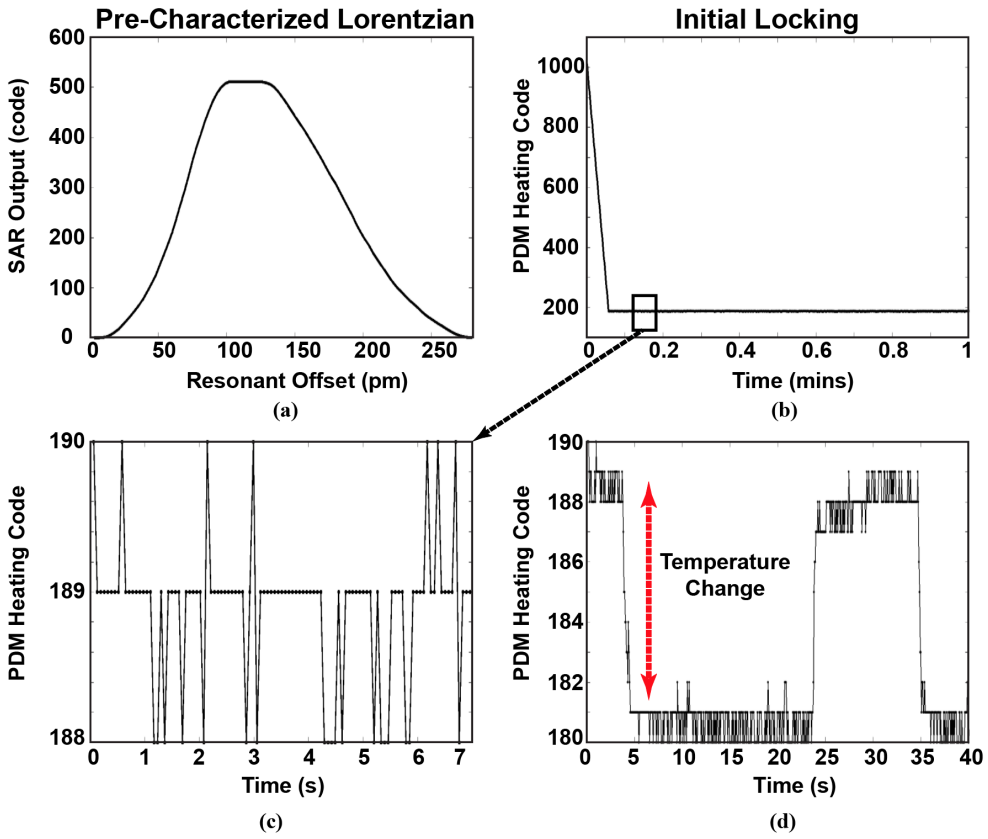

Figure 6.5: On chip tuning controller operation. (a) Pre-characterized Lorentzian Spectrum of the MRR. (b) Locking of the MRR. Starting from off-resonance the PDM heating decreases and blue-shifts the ring until the bias point is detected. (c) Locking resolution. (d) On-chip re-locking of the MRR at its nominal bias point, cancelling any temperature fluctuations.

6.1.6 Differential Readout Demonstration

We suppress the environmental common-mode drift and non-specific binding interference by using a differential scheme of a sensing and reference ring located 425µm apart. To characterize the effectiveness of this architecture, the MRRs – not exposed to any biosamples – are monitored in real-time at a fixed wavelength and heating code, and the differential shift is calculated by subtracting the reference shift from the sensing response.

First, the Lorentzian spectra of the sensing and reference rings are pre-characterized, as shown in Fig. 6.6a,b. By monitoring the ADC responses of the sensing and reference receiver at a fixed wavelength (Fig. 6.6c) and dividing the relative changes by the slope of the sensing and reference MRR spectrum – defined in eq. (6.1) – around the region of operation (Fig. 6.6a,b), the electronic responses are converted into resonant shifts. Subtracting the reference from the sensing signal results in an effective differential shift, as illustrated in

Fig. 6.6d. As can be observed from the post-averaged differential shift (moving average with 1 minute window) in Fig. 6.6e, the ambient temperature variations result in a peak sensing

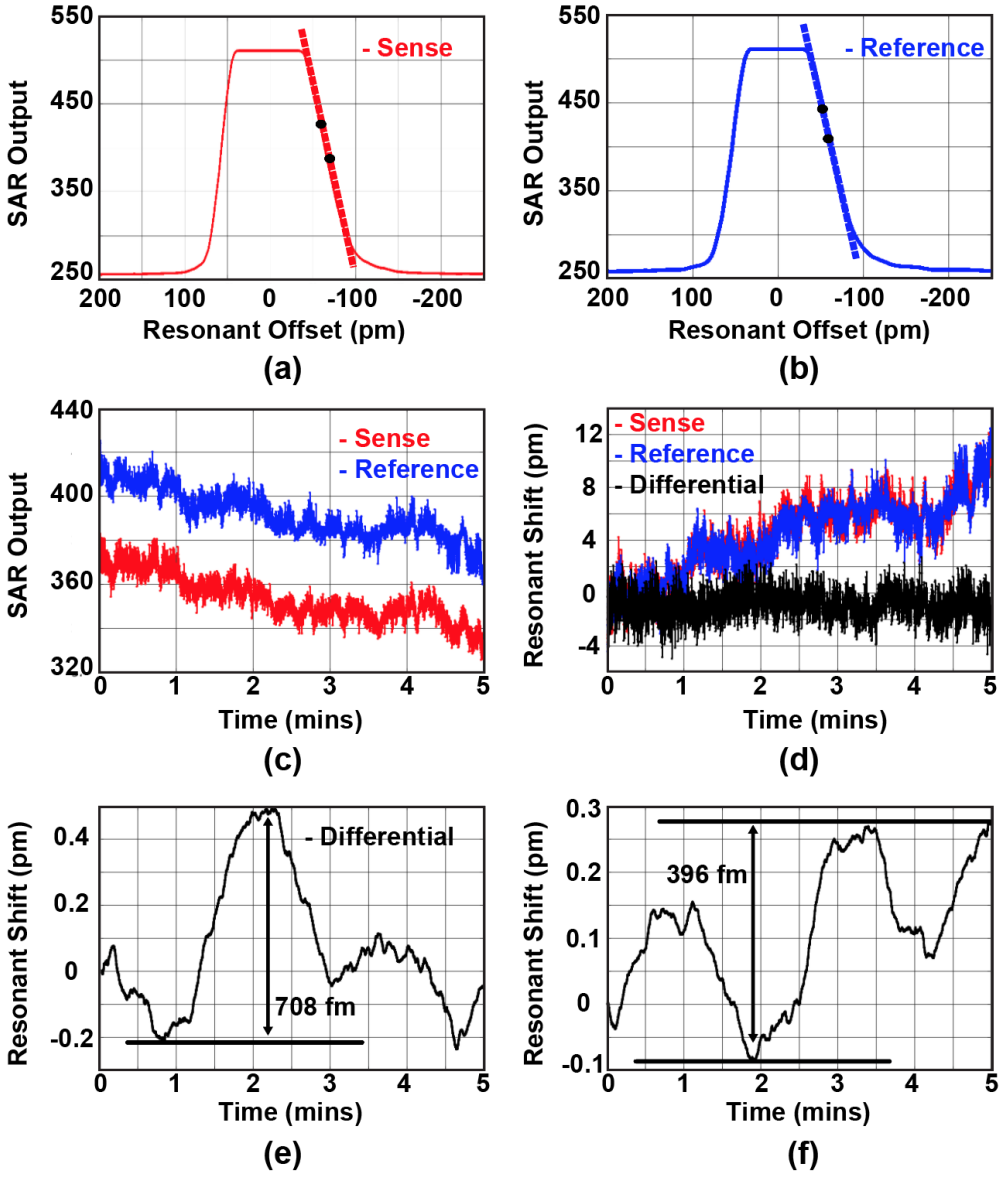

Figure 6.6: On-chip differential scheme for ambient common mode error cancellation. (a),(b) Characterization of the Lorentzian spectrum of the sensing and reference ring. (c) Monitoring of the sensing and reference ADC responses. (d) Sensing, reference and effective differential resonant shift. (e) Post-averaged differential shift. (f) Post-averaged differential shift at increased input optical power. The peak to peak differential signal corresponds to the detection of approximately 2 140nm particles, similar to the size of a viral particle.

and reference resonant shift of ≈9pm, while the effective differential response is <1pm, thus suppressing the ambient common mode fluctuations by ≈$x10$. The same experiment is repeated at an increased optical power and more stable temperature conditions. After subtracting the effect of the reference ring, the differential shift is obtained, as shown in Fig. 6.6f. The standard deviation and peak to peak value of the effective differential signal are 100fm and 396fm respectively, thus approaching the detection of a single nanoparticle of 140nm size and 1.6 RI, similar to the characteristics of a viral particle, which induces a 170fm shift. Additionally, based on the $2\frac{nm}{RIU}$ intrinsic sensitivity of the platform, characterized in [63], the peak-to-peak differential shift corresponds to 1.98*10^{-4} RIU. The LoD can be further improved by $x3.7$, leveraging the sensitivity enhancement offered by the dual-ring phase detection scheme, thus resulting in a sub-nanoparticle resolution. By combining the minimum detectable shift with the ≈7nm maximum tuning range at a heater supply voltage of 1.8V [63], a system dynamic range of 79dB is achieved.

In clinical applications, the LoD of a bio-assay is often found in Molar concentration units. Therefore, the minimum detectable number of particles needs to be converted in a molecular concentration. From first order kinetic equations and assuming a linear initial response of the reaction, the number of target molecules binding on the surface of the ring can be given by:

$$N_{mol} = k_a[A_{target}]A_{area}[B_{max}]t_{sense}, \tag{6.2}$$

where k_a is the association constant, A_{area} is the area of the ring, $[A_{target}]$ is the target analyte concentration $[B_{max}]$ is the receptor concentration. As observed, the target analytes binding on the surface increase linearly with the assay time t_{sense}. In order to express the LoD in a Molar concentration unit, we can write:

$$[A_{target}]_{LoD} = \frac{N_{mol-MDS}}{k_a A_{area}[B_{max}]t_{sense}} = \frac{\frac{V_{out-MDS}}{S_{tot}}}{k_a A_{area}[B_{max}]t_{sense}} = \frac{\frac{V_{out-MDS}}{S_{int}S_{phot}R_{PD}Gain_{RX}}}{k_a A_{area}[B_{max}]t_{sense}}, \tag{6.3}$$

where $N_{mol\text{-}MDS} = \frac{V_{out-MDS}}{S_{tot}}$ is the minimum detectable number of molecules, $V_{out\text{-}MDS}$ is the minimum detectable output voltage signal and $S_{tot} = S_{int}S_{eff}$ is the total sensitivity, as defined in eq. (2.10), eq. (6.1). The intrinsic sensitivity term S_{int} depends on the specific type of target molecule, since a large particle interacts within a larger volume with the evanescent field compared to smaller proteins. For a 140nm particle of 1.6 RI the simulated intrinsic sensitivity is ≈170fm, whereas for 5nm proteins of 1.45 RI, S_{int} scales down to ≈0.03fm. In order to improve the limit of detection, the dominating noise source needs to be identified. Assuming the input referred noise current of the receiver is dominated by circuit elements connected at the input, the tuning knobs to lower $N_{mol-MDS}$ would be increasing the intrinsic sensitivity S_{int}, obtaining a sharper MRR spectrum through an enhanced S_{phot} and increasing the responsivity of the photodetector R_{PD}. For an ambient-noise dominated performance, strengthening the interaction of the evanescent field with molecules and increasing S_{int} lowers $N_{mol-MDS}$.

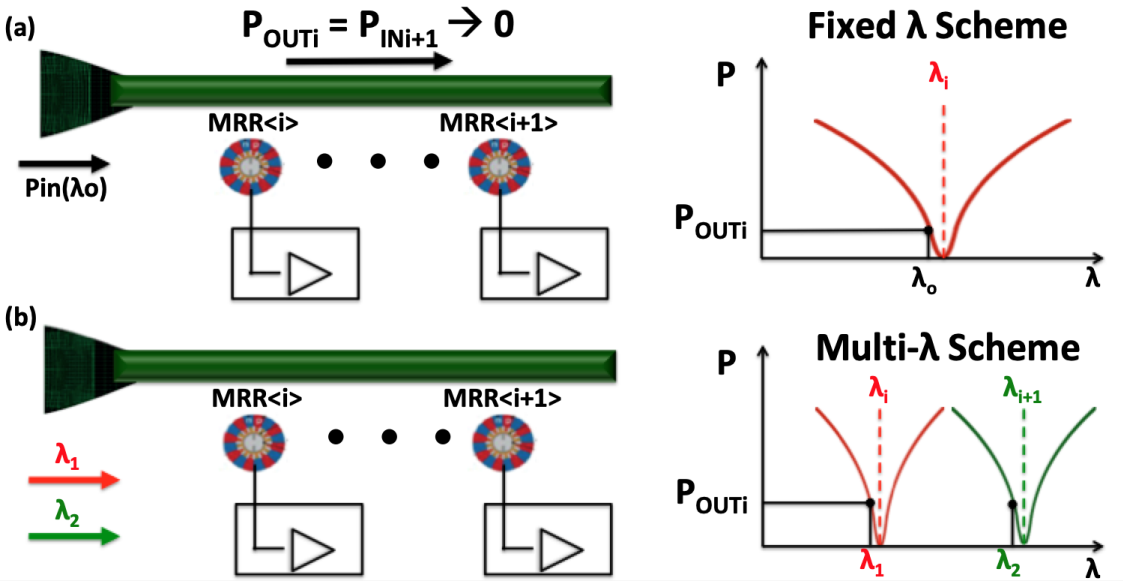

Figure 6.7: (a) A single wavelength sensing scheme results in significant cross-ring interference. (b) A comb laser allows simultaneous interrogation of multiple rings at different fixed wavelengths.

6.1.7 Multiplexed Sensing Scheme

The ability to integrate multiple ring resonators into highly scalable arrays allows us to interrogate in parallel more than one MRR in a ring row. This, however, cannot be possible in a fixed wavelength scheme, as illustrated in Fig. 6.7a. Having two rings, $MRR < i >$ and $MRR < i+1 >$ parked at the same wavelength results in minimizing the optical power incident to $MRR < i+1 >$, since most of the power circulates inside the ring waveguide of $MRR < i >$. Additionally, any power fluctuations monitored in $MRR < i >$ could result from resonant shifts of both rings, thus complicating the detection of the fluctuation.

In order to address this challenge and leverage simultaneous interrogation of multiple rings, a comb laser diode with multiple fixed wavelengths can be utilized. This multiplexed sensing scheme is shown in Fig. 6.7b. Each MRR can be biased at a different wavelength of the laser, therefore eliminating any cross-channel interference. We have demonstrated this with a row of 4 rings, as illustrated in Fig. 6.8a. Each MRR has a radius increment of 2nm which facilitates the nominal spreading of the resonances to match the wavelength pitch of the comb laser. Leveraging the active resonant tuning mechanism with integrated heaters, each ring is locked at a specific wavelength of the laser. Therefore, in parallel monitoring of multiple rings can be accomplished in which the shift fluctuations of one ring do not affect the rest of the MRRs in the row.

Figure 6.8b shows the Lorentzian spectrum of 4 rings captures using a fixed comb wavelength laser diode. In this experiment, an Innolume comb laser was used and wavelength

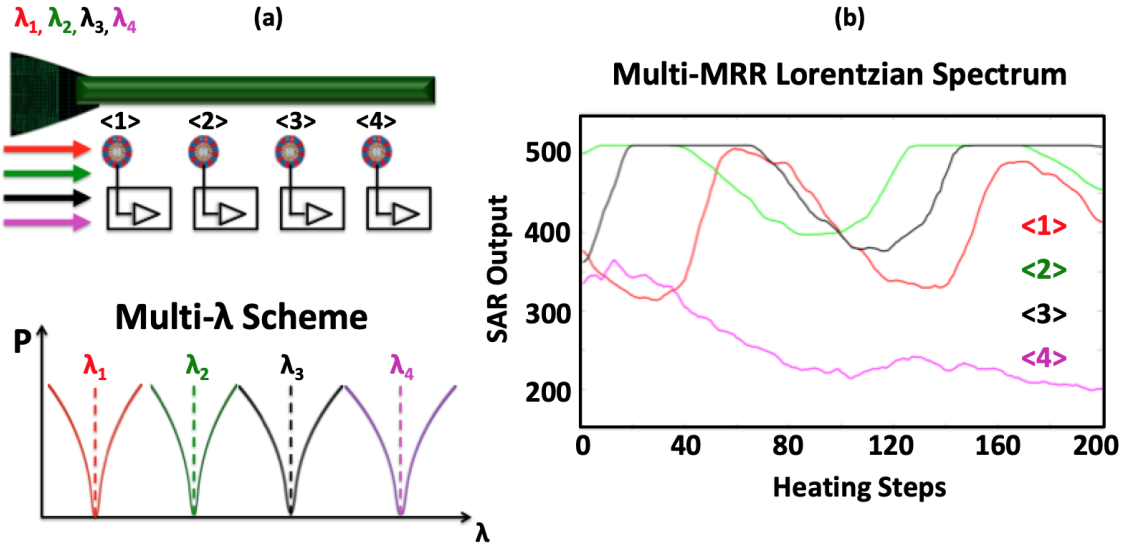

Figure 6.8: (a) A row of 4 MRRs is interrogated using a comb laser of multiple fixed wavelengths. (b) Simultaneous capture of the Lorentzian spectrum of the rings using a comb laser.

region of interest was in the range of ≈1315nm to 1320nm. As a first step, the nominal resonances of the MRRs were initially characterized to ensure their close proximity to the wavelength region of the laser. The input heating codes of the rings were then swept simultaneously, therefore tuning their resonances at a step of ≈3pm, similar to the methodology described in Section 6.1.2.

6.2 Biosensing Measurements

6.2.1 Experimental Setup and Initial Testing Procedure

Developing a fully integrated electronic-photonic SoC for label-free molecular sensing requires simultaneous electronic photonic and fluidic coupling. Therefore as first proof of concept we expose the complete LoC package to a water-based fluidic solution and examine its performance.

Fig. 6.9 shows the experimental setup used for performing fluidic sensing experiments. The chipboard with the co-packaged microfluidics is plugged on a socket of the hostboard which is mounted on an optical stage. A single mode fiber attached to a holder is passed through glass and PDMS openings and accesses the chip to couple light. Next, input needles are connected to the inlet PDMS gaskets to enable delivery of fluidic solutions. As illustrated in Fig. 6.9, the needles are connected to macro-scale tubing which is attached to a syringe

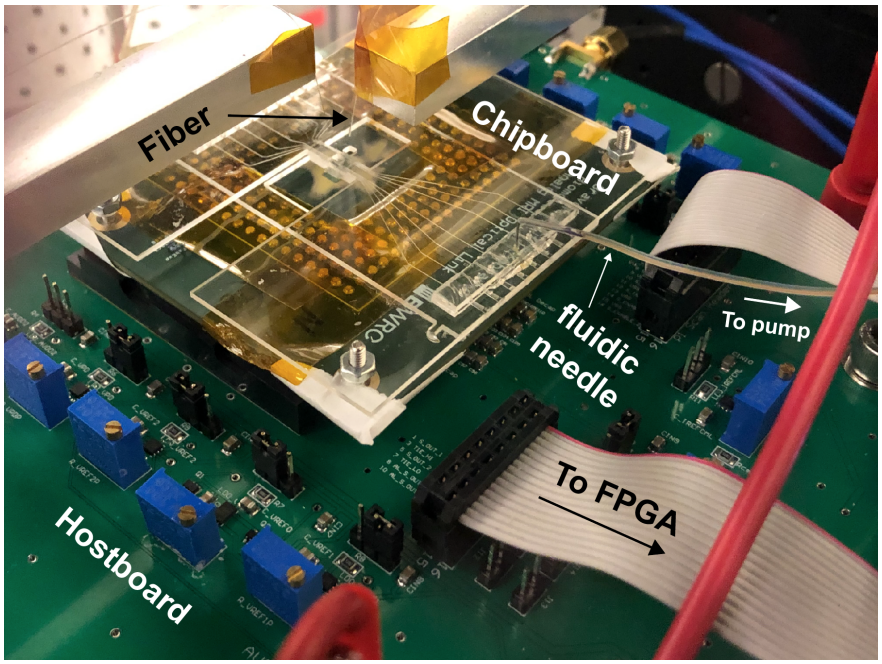

Figure 6.9: Experimental Setup.

placed in a syringe pump. By activating the pump and setting a fixed flow rate, we ensure a continuous delivery of the fluidic solution.

After plugging the chipboard with co-packaged microfluidics in the socket of the hostboard and coupling light, the chip is powered and the scan-chain test is run to ensure functionality after fluidic attach. Next, a single ring-PD is selected for characterization while all other rings of the same row are tuned off-resonance so that interference from ring to ring is negligible. We achieve this by shifting the rings by >2nm using their integrated heaters. Once we isolate the ring of interest in the region of the fixed wavelength laser, the receiver is biased and we sweep the heating code of the PDM driver at a step of 3pm, similar to the procedure described in Section 6.1.2. The initial Lorentzian spectrum of the MRR when exposed to air is characterized. After the syringe pump turns on and fluid arrives on the ring, the Lorentzian spectrum is captured again using the on-chip receiver. Figure 6.10 illustrates the ring spectrum before and after the ring is exposed to water.

As can observed, a resonant red shift of ≈230pm is found, which is lower compared to the expected shift of ≈600pm. This can be explained by the cooling of the ring sensor when the fluid contacts the chip for the first time, especially when the MRR is operated along with its receiver.

6.2.2 Bulk RI Characterization

The RI sensing capability of the fully integrated electronic-photonic sensor is first evaluated with different NaCl-water concentrations which introduce uniform changes in the RI of the platform's cladding environment. By sweeping the on-chip heater at a 1.1V supply and capturing the ring spectrum before and after flowing the salt solution, a change in resonance is determined [63]. Fig. 6.11 shows the static shifts from three different NaCl concentrations. By characterizing the RI of each of the solutions using an ATC refractometer, a bulk sensitivity of $\approx 2\frac{nm}{RIU}$ is extracted. This detection method provides a coarse evaluation of large signals, however it is limited by the step resolution and speed of the heating sweep.

6.2.3 Label-Free Real-Time Molecular Kinetics

Next, we demonstrate real-time molecular kinetics using the well known pair of biotin and streptavidin binding. In order to suppress common-mode temperature and pressure changes, a sensing and a reference ring in two channels are measured.

After functionalizing the sensing MRR with biotin, the Lorentzian spectra of the sensing and reference rings are characterized (Fig. 6.12a), and an initial bias point is selected for both MRRs. A 16µM streptavidin solution is flown through the sensing microfluidic channel and the ADC responses of both MRRs are monitored in real-time at a fixed heating code (Fig. 6.12b) [63]. The electronic responses captured at a 50kΩ TIA gain are then converted

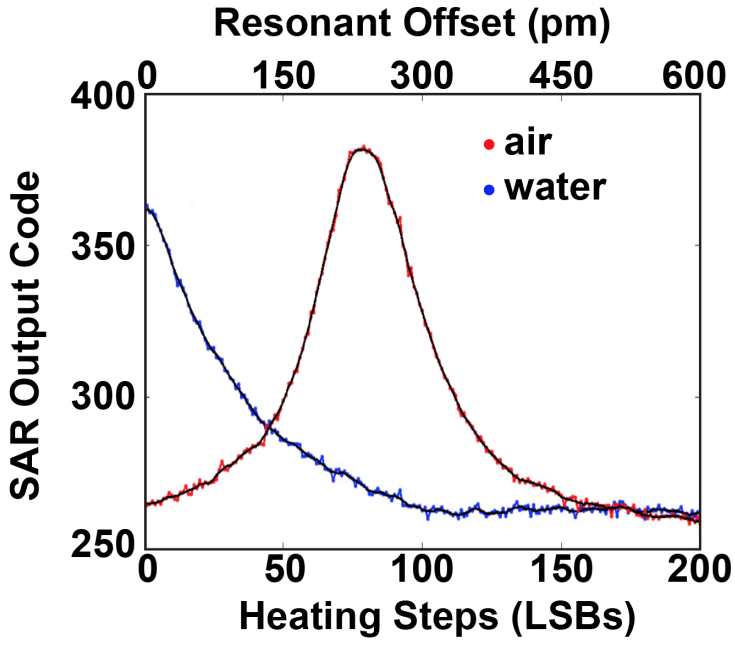

Figure 6.10: Shifted Lorentzian spectrum after exposure to water.

into resonant shifts by dividing the relative SAR changes over the averaged Lorentzian slopes (Fig. 6.12c) and an effective differential shift is established after subtracting the reference from the sensing signal, as illustrated in Fig. 6.12d. The binding curve is characterized by an initial slope of $\approx 12 \frac{pm}{min}$ which depends on the target analyte concentration and describes the binding rate of the reaction. Kinetics are then followed by an equilibrium between association and dissociation of molecules, resulting in a steady-state response of ≈46pm.

Using a similar methodology, kinetics of a 100nM streptavidin solution are detected at a 200kΩ TIA gain and a lower initial slope is recorded (Fig. 6.13a-d) as expected [64]. As can be observed, the reference MRR cancels the temperature and pressure ambient shift, isolating the kinetics from the sensing MRR.

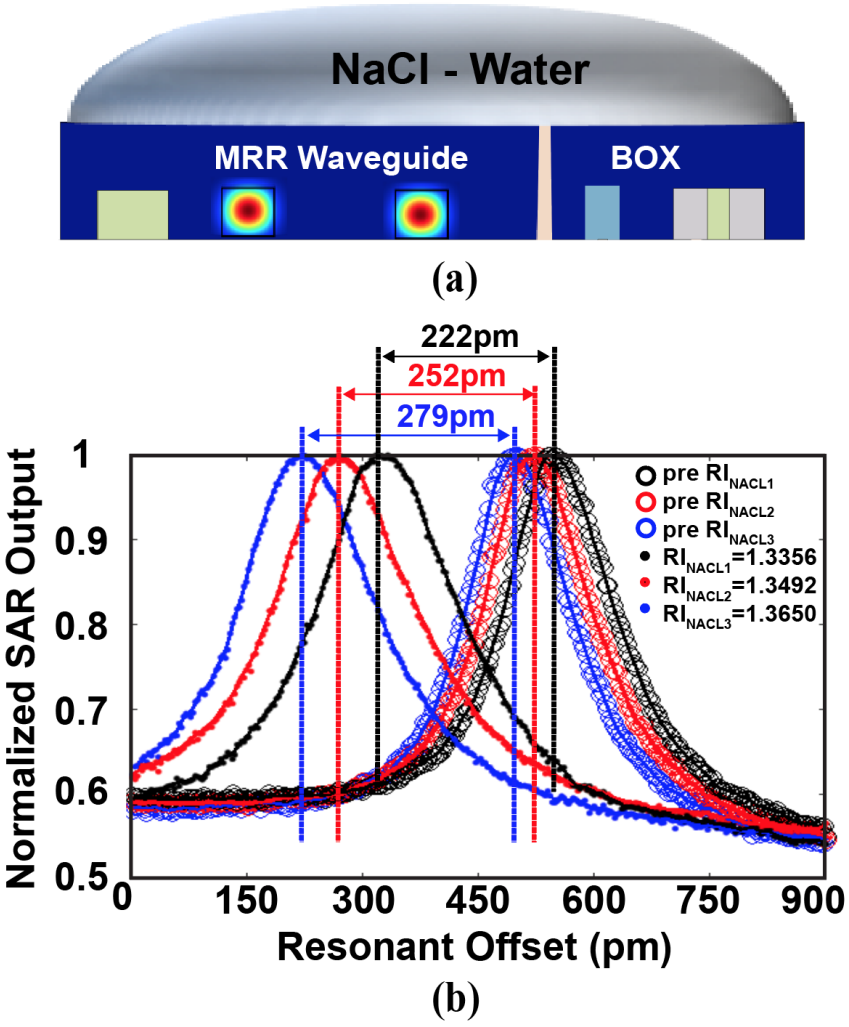

Figure 6.11: Static bulk RI shift characterization for different NaCl solutions.

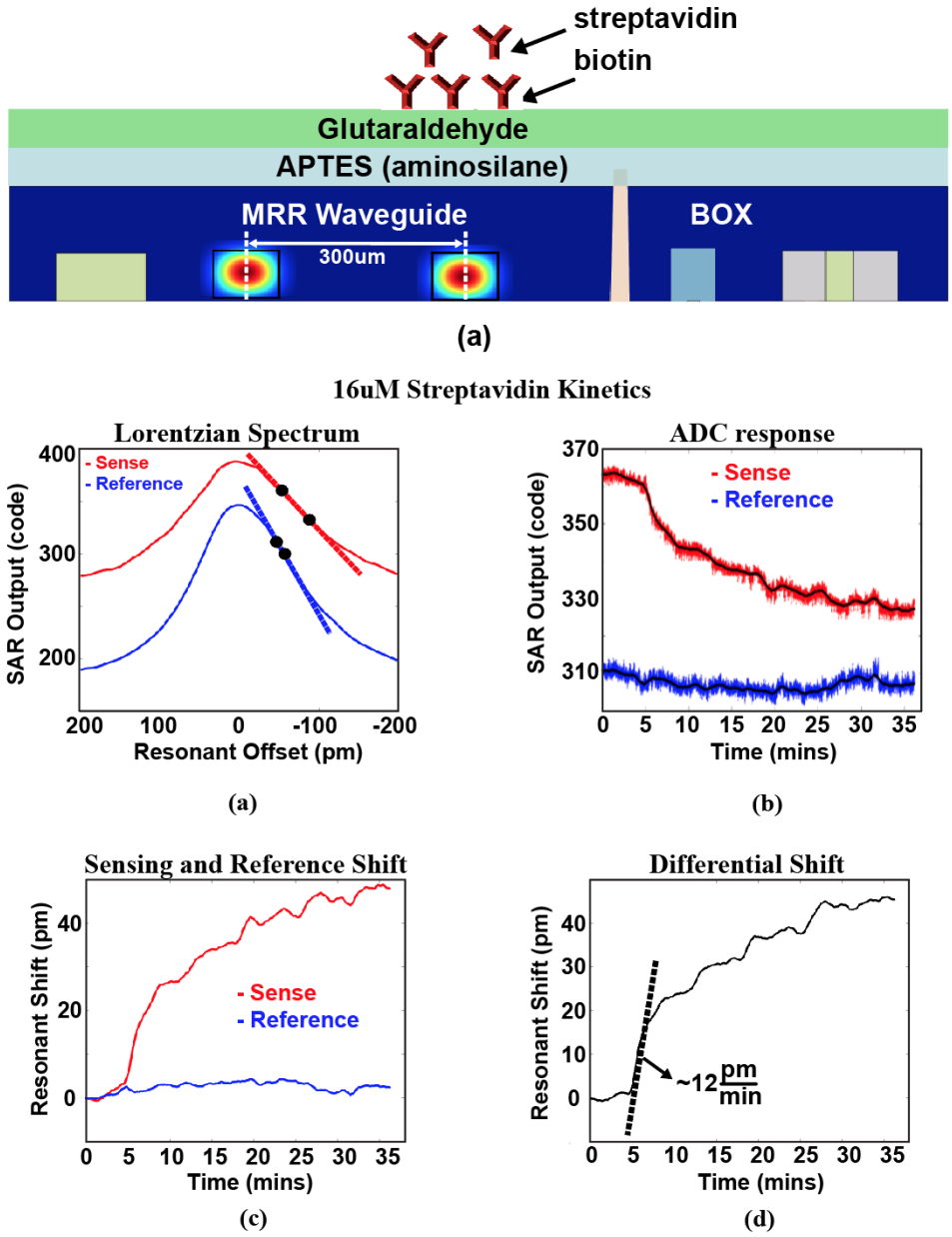

Figure 6.12: (a)-(d) Real-time streptavidin kinetics of a 16µM solution. The Lorentzian spectrum of the sensing and reference MRR is characterized (a) and the individual sensing and reference ADC outputs are monitored (b). After subtracting the post-averaged reference signal from the sensing shift (c), a differential shift is established (d). The initial binding rate of the reaction is followed by an equilibrium phase.

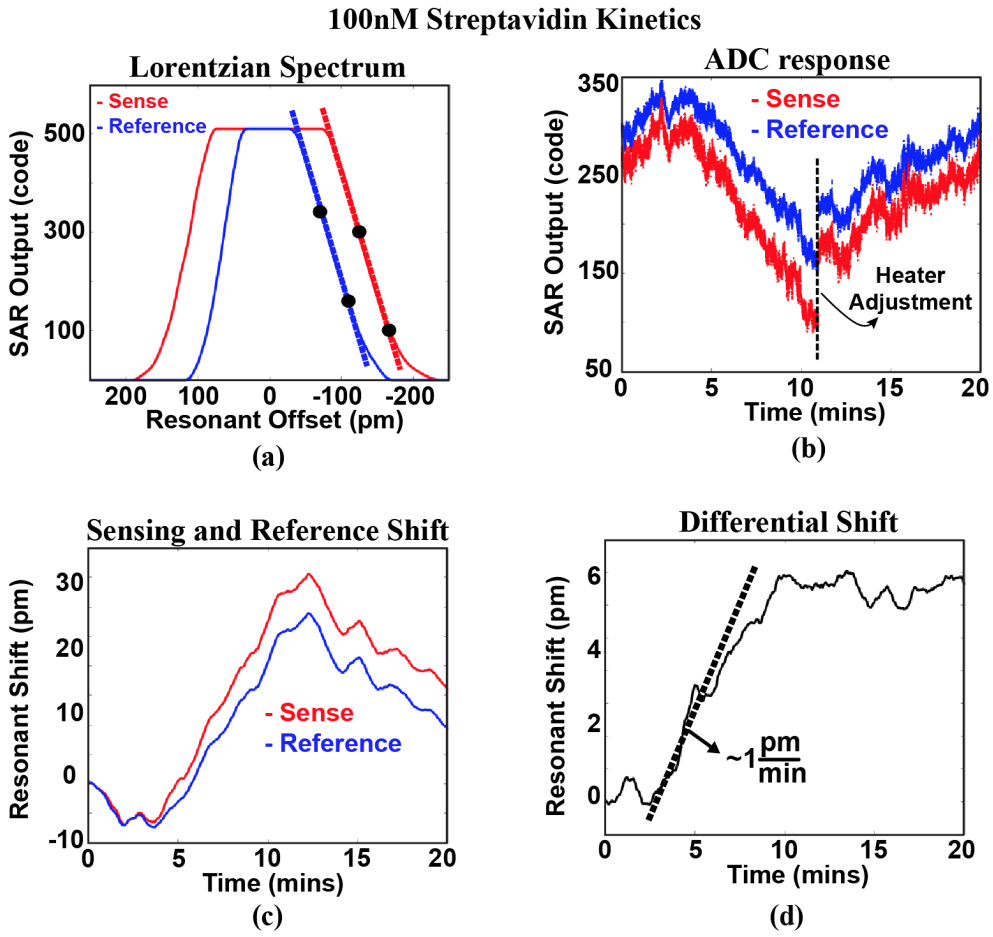

Figure 6.13: (a)-(d) Real-time streptavidin kinetics of a 100nM solution. The Lorentzian spectrum of the sensing and reference MRR is characterized (a) and the individual sensing and reference ADC outputs are monitored (b). After subtracting the post-averaged reference signal from the sensing shift (c), a differential shift is established (d). The initial binding rate of the reaction is followed by an equilibrium phase.

In [63] we demonstrated for the first time real-time molecular kinetics in a fully integrated electronic-photonic platform using crosslinker-labeled biotin molecules and streptavidin. Here we modify the coating chemistry and activate the surface of the chip instead of the receptors, in order to directly immobilize molecules, not conjugated with any crosslinkers. To verify the modified chemistry, we present real-time kinetics of anti-BSA and BSA binding without using conjugated receptors.

After uniformly coating the surface of the chip with an aminosilane layer of APTES, the die was immersed in 2.5% glutaraldehyde solution and incubated for 1hr at RT. This results in the formation of a crosslinker layer that allows direct immobilization of non-conjugated

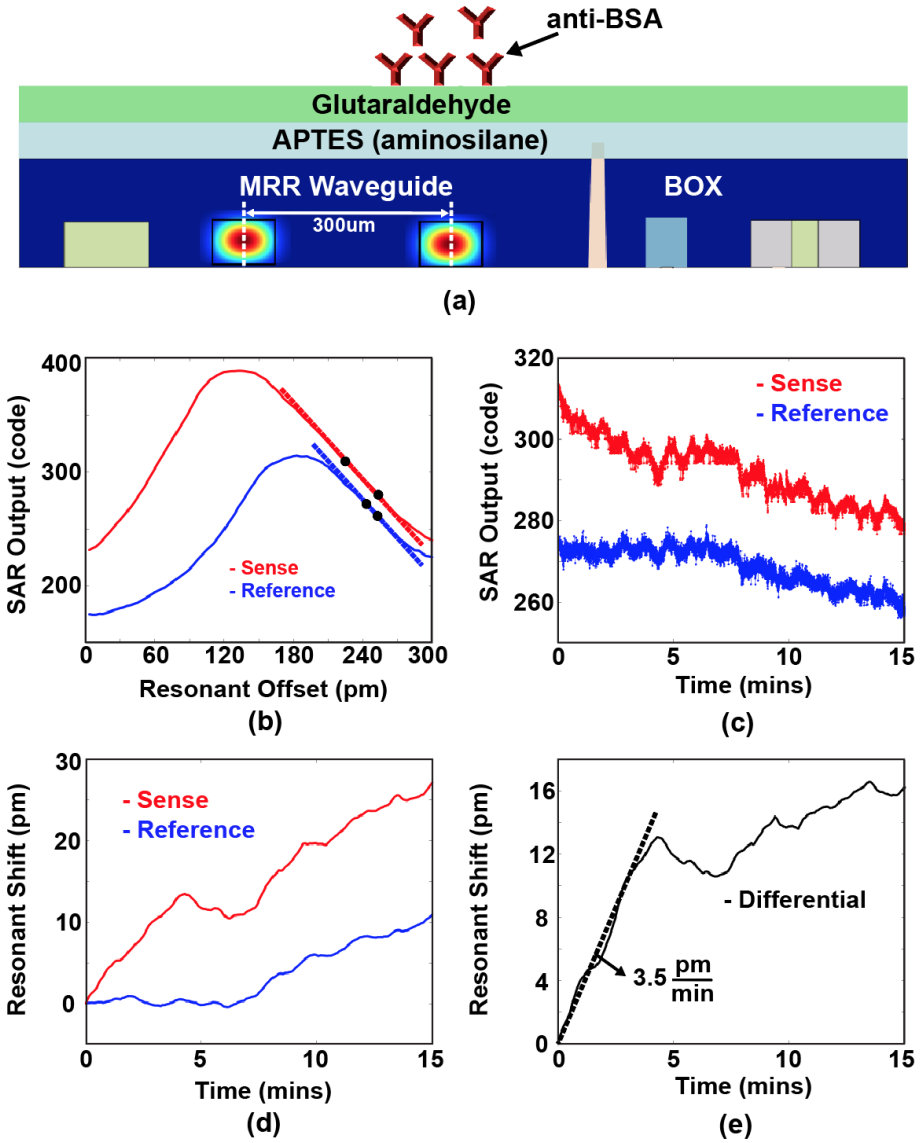

Figure 6.14: (a)-(e) Real-time molecular kinetics of a 3.3µM anti-BSA solution. The SiO_2 BOX surface is coated with an aminosilane layer and functionalized with a glutaraldehyde crosslinker layer that allows direct immobilization of non-conjugated anti-BSA on the surface (a). The Lorentzian spectrum of the sensing and reference MRR is characterized (b) and the sensing and reference ADC responses are monitored (c). After subtracting the reference from the sensing shift (d), an effective differential signal is obtained (e), representing anti-BSA kinetics.

antibodies [65]. The sensing ring was functionalized in-channel with anti-BSA molecules in order to detect the specific binding events of BSA of ≈5nm size (Fig. 6.14a). After the coating

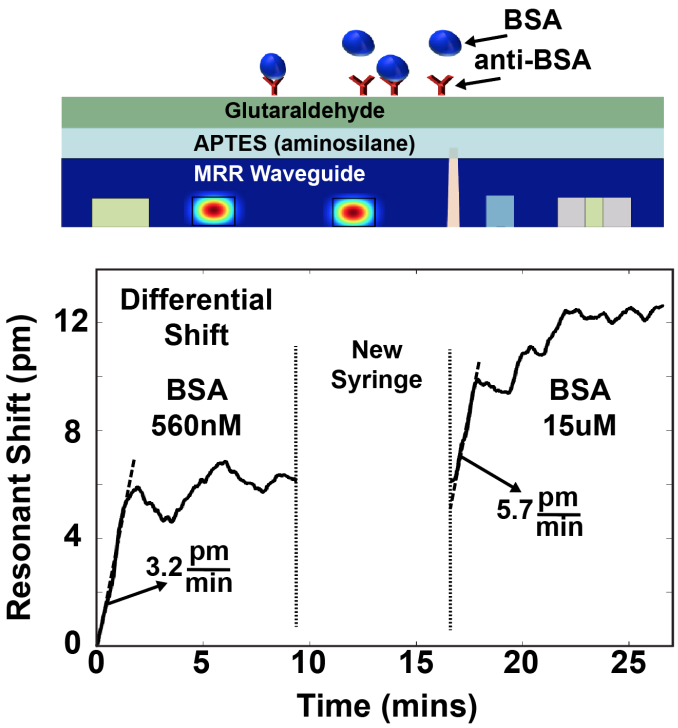

Figure 6.15: Differential shift from 560nM and 15µM BSA kinetics.

with glutaraldehyde, the Lorentzian spectrum of the sensing and reference ring is first characterized, as shown in Fig. 6.14b and an initial bias point is selected for both rings. The sensing ring is then functionalized in-channel with anti-BSA molecules. A 3.3µM anti-BSA solution is flown through the sensing microfluidic channel at a $5\frac{\mu L}{min}$ flow rate while PBS is flown over the reference ring. The ADC responses of both MRRs are monitored in real-time at a fixed wavelength and heating code, as shown in Fig. 6.14c. After converting the electronic responses into resonant shifts (Fig. 6.14d) and subtracting the reference from the sensing response, an effective differential shift is established, as illustrated in Fig. 6.14e. The binding curve is characterized by an initial slope of $3.5\frac{pm}{min}$ which depends on the analyte concentration and describes the binding rate of the reaction. Kinetics are then followed by an equilibrium between association and dissociation of anti-BSA molecules which results in a steady state of ≈15pm.

The specific binding of BSA-antiBSA is then monitored for 560nM and 15µM BSA solutions, as shown in Fig. 6.15. An overall steady-state shift of ≈12pm is measured. The reduced increase of the initial binding slope at 15µM concentration can be attributed to the partial coverage of the anti-BSA receptor sites from the previous 560nM BSA solution.

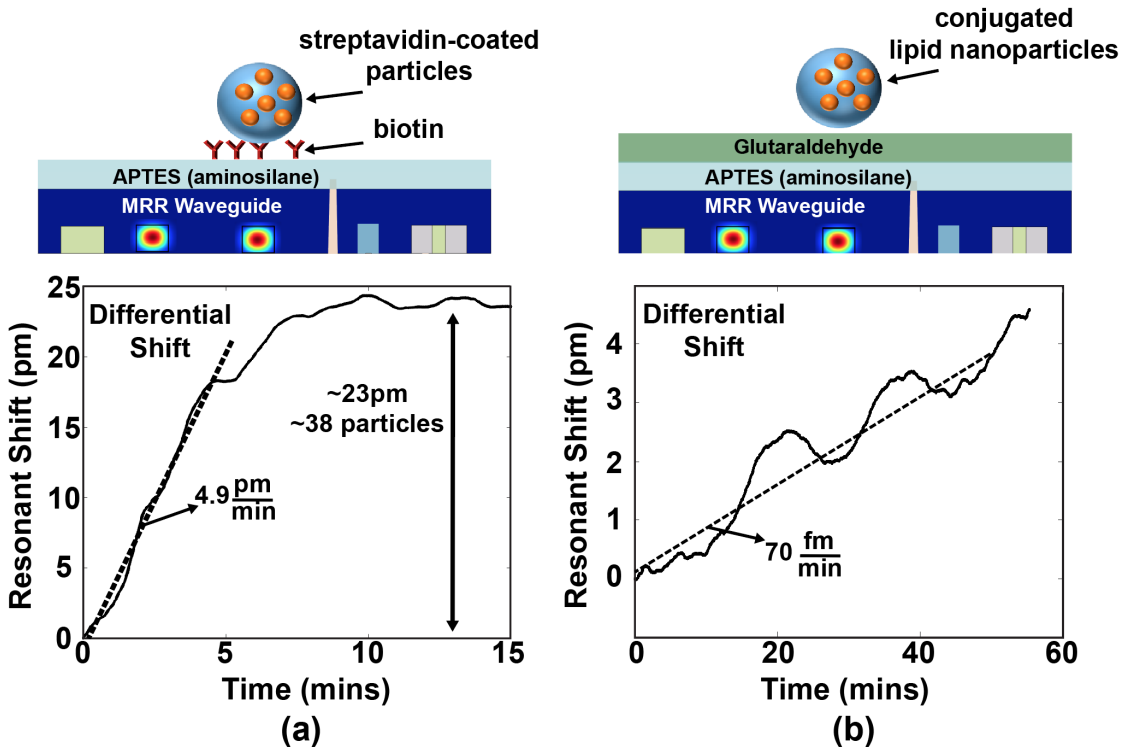

Figure 6.16: (a) Differential shift from 150nm streptavidin-coated nanoparticle binding. (b) Differential shift from 100nm active lipid nanoparticles.

6.2.4 Nanoparticle detection

After establishing a first proof of concept for real-time molecular sensing, we investigated the detection of streptavidin coated 150nm nanoparticles with biotin. Nanoparticles conjugated with target analytes have been used in label-free sensing for amplifying the detected binding signal [66]. Additionally, their >100nm size is similar to the size of viral particles, therefore making them good candidates for mimicking viruses. We demonstrate real-time kinetics of streptavidin coated nanoparticles (Ocean NanoTech) at a 50pM concentration ($3*10^{10}\frac{particles}{ml}$), establishing the versatility of the platform in detecting various types of molecules, ranging from proteins to nanoparticles. A sensing ring is first functionalized with biotin molecules that act as receptors for the specific detection of streptavidin (Fig. 6.16a). After flowing the conjugated particle solution through the sensing fluidic channel and using a similar detection methodology of subtracting the reference from the sensing ring response, an overall effective differential shift is monitored (Fig. 6.16a). Based on the simulated resonant shift of ≈600fm induced from a single 150nm particle binding event with RI≈2.2, the overall measured shift of ≈23pm corresponds to the detection of ≈38 nanoparticles. As a further step, the specific binding events between active lipid nanoparticles and ACE2 protein

Table 6.1: Real-time Molecular Kinetic Experiments

Molecular Concentration	Target Molecule	Receptor Molecule	Initial Slope
16µM	Streptavidin (≈5nm)	Biotin	$12\frac{pm}{min}$
100nM	Streptavidin (≈5nm)	Biotin	$1\frac{pm}{min}$
3.3µM	Anti-BSA (≈5nm)	- (Aminosilane layer)	$3.5\frac{pm}{min}$
560nM	BSA (≈5nm)	Anti-BSA	$3.2\frac{pm}{min}$
15µM	BSA (≈5nm)	Anti-BSA	$5.7\frac{pm}{min}$
$3*10^{10}\frac{\text{particles}}{\text{mL}}$	Streptavidin-coated nanoparticles (≈150nm)	Biotin	$4.9\frac{pm}{min}$
$\frac{10^9\text{particles}}{400\mu\text{L}}$	Active lipid nanoparticles (≈100nm)	ACE2	$70\frac{fm}{min}$

	This work			Zhu [7] Nature '10	Iqbal [13] IEEE Quant. El. '10	Flueckinger [30] Optics Express '16	Leuermann [23] Sensors '19
Sensor	MRR			Micro-Toroid	MRR	MRR	MZI
Photonic Technology	**CMOS RFSOI 45nm**			Passive	Passive	Passive	Passive
On-Chip Readout Processing	**Yes**			No	No	No	No
Single Wavelength Laser	**Yes**			No	No	No	Yes
Limit of Detection	Single MRR-PD	RAMZI	Etched BOX				
Equivalent to RIU	$1.98*10^{-4}$	$5.35*10^{-5}$	$7.6*10^{-6}$	N/A	$7.6*10^{-7}$	$2*10^{-6}$	$\sim10^{-8}$
Equivalent to # of 140nm particles	**~2**	sub 1		sub 1	sub 1	sub 1	sub 1
Transducer Area (um²)	**78** (5um radius)			3D (15um radius)	707 (15um radius)	707 (15um radius)	~400 (folded 6mm wguide)

Figure 6.17: Comparison Table with State-of-the-Art.

was also investigated [67]. The 100nm size of the nanoparticle acts as a mimic of a SARS-CoV-2 particle (Lydia Sohn Research Lab, [68]). The surface chemistry included the initial functionalization of the sensing and reference ring with biotin and streptavidin followed by a biotinylated-PBS ACE2 solution (ACRO Biosystems) which acts as the receptor molecule. Two different 400µL solutions of 10^9 active and non active nanoparticles (≈4pM) were flown through the sensing and reference channel respectively. By following the same detection method of subtracting the reference from the sensing ring response, an overall effective differential shift is monitored (fig. 6.16b) which mostly represents the specific binding between active lipid nanoparticles and ACE2.

Table 6.1 summarizes the real-time kinetic experiments performed with our first-generation biosensing EPSoC. Real-time monitoring of both proteins and nanoparticles is demonstrated, establishing the versatility of the platform in detecting various types of molecules.

Figure 6.17 summarizes the performance of the EPSoC and compares it with other state-of-the-art label-free photonic platforms. This work is the world's first fully integrated biophotonic sensor, enabling nanophotonic label-free sensing and readout processing on the same die of a high volume commercial process. The measured *LoD* corresponds to the physical presence of ≈2 140nm viral particles of $RI = 1.6$ and can be further lowered to a sub-nanoparticle resolution using phase detection. It should also be noted that partial etching of the SiO_2-BOX layer by 100nm can further boost sensitivity by $x7$ [30].

6.3 Summary

We demonstrated the world's first monolithic electronic-photonic LoC system and established the label-free sensing capabilities of the SoC for the first time in a fully integrated platform. First, we characterized the electronic response of the receiver by obtaining the *dc* characteristic and measuring the noise performance. Next, we evaluated the electronic-photonic performance by exploring various photonic sensing architectures.

Starting from the intensity-based detection, we first demonstrated results from the simple scheme of a single ring-based PD, which can act both as a sensor and as a photodetector. After obtaining the Lorentzian spectrum of the MRR-PD and characterizing its sensitivity, we introduced a dual-ring scheme. Leveraging the higher quality factor of the sensing ring which is interrogated by a separate MRR-PD, we verified the improved performance of the scheme. However, this occurs at the cost of higher complexity due to the need to thermally control two rings instead of one.

Additionally, phase detection structures were also implemented in this work. The superior performance of phase-based sensing compared to intensity detection, as predicted from theoretical analysis [33], was demonstrated using a RAMZI architecture. This scheme offers the two-fold advantage of using higher Q rings as the biosensors and detecting phase instead of amplitude changes.

In order to address the sensitivity of rings towards environmental fluctuations, results from the on-chip differential readout scheme were presented. By subtracting the signal of a reference MRR structure from the shift of a sensing ring, both exposed to air, a differential shift was measured. Environmental variations can also be cancelled using an on-chip tuning controller which locks the ring at the desired point bias point and resets its spectrum back to its initial position, thus providing a wide DR.

We demonstrated the label-free biosensing performance of the monolithic EPSoC by characterizing the bulk sensitivity of the platform and presenting real-time molecular kinetics. First, the bulk sensing performance was evaluated by exposing a ring to different salt-water concentration solutions which introduce a different RI in the cladding environment. By detecting the relative shift before and after exposing the ring to the samples, the bulk sensitivity can be extracted Moving towards the goal application of monitoring molecular dynamics, we demonstrated the label-free biosensing performance of the EPSoC by presenting binding events of proteins and nanoparticles. First, real-time kinetics of streptavidin binding

to biotin were presented using a pair of sensing and reference rings to subtract common-mode variations. By adding an additional layer of glutaraldehyde cross-linkers we enable direct immobilization of receptor antibodies and verified the functionality of the chemistry by detecting real-time kinetics of anti-BSA and BSA. Additionally, we presented binding events from 150nm streptavidin coated particles and 100nm active lipid nanoparticles, mimicking viral particles. These experiments highlight the versatility of our system in detecting various types of molecules, unlocking the path towards highly miniaturized and compact electronic-photonic LoC systems for PoC applications.

Chapter 7

Conclusion

7.1 Summary

Over the last decades evanescent field photonic sensors have shown increasing promise in monitoring real-time label-free molecular kinetics. However, despite the significant progress achieved in optimizing the transducer's sensitivity, the main bottleneck towards the large scale commercialization of these photonic systems towards PoC applications has been the need to complex optics, a tunable laser and external readout equipment. This hinders the development of miniaturized LoC systems, thus confining them in well-regulated clinical laboratories. In this research, we introduced a first of its class fully integrated electronic-photonic SoC for real-time label-free molecular sensing. By leveraging co-integration of 5µm radius MRRs with on-chip electronics into highly scalable sensing arrays, we demonstrate label-free nanophotonic biosensing and readout processing on the same die and unlock the path towards miniaturized self-contained photonic LoC sensors.

In this thesis, we first provided an overview of prior work on label-free photonic transducers which are divided intro interferometric and resonant-based sensors. Despite the promising *LoDs* reported from MZI structures, the dependence of sensitivity on the length of the waveguide arms complicates the design of densely packed arrays for multiplexed sensing. This challenge is addressed with the use of highly miniaturized resonant transducers, which instead rely on the the large quality factor resulting in a sharp resonant spectrum. In this work, we focused on Micro-Ring Resonators (MRRs) which are ideal candidates for multi-analyte sensing using highly scalable arrays. We first analyzed the key characteristics of the MRR sensor and described two main categories of MRR-based photonic architectures: Amplitude and Phase detection structures. In Chapter 2, we analyzed and optimized the sensitivity of each scheme and suggested two modulation techniques that could be used to further improve the sensing performance by leveraging both phase detection and mitigating low frequency noise.

Next, we introduced the monolithic high volume 45nm process which allows co-integration of MRRs with advanced electronics. In Chapter 3, we first described the key characteristics of

the platform and provided simulation results characterizing the intrinsic sensing performance: bulk and surface sensitivity. By demonstrating preliminary molecular kinetic results in a passive chip, we established a first proof of concept that demonstrated the label-free sensing capability of the monolithic process. In these experiments, an external powermeter and a tunable laser were used limiting the measurement speed, while single channel microfluidic could only allow single ring testing.

Moving towards multi-analyte molecular sensing, an efficient way of delivering multiple fluidic solutions on µm-scale sensors located in mm-scale chips is strongly desired. In Chapter 4, we proposed an efficient way of prototyping and packaging multi-channel and multi-layer fluidic packages that could-interface with mm-scale chips. Using 3D printed molds of high resolution channels and multiple pillar-via structures, multi-channel and multi-layer fluidic devices can be easily fabricated, avoiding the complexity of photolithography processing techniques. Additionally, large opening in PDMS can be patterned to provide enough space for single fibers or fiber arrays to access the chip and couple light. The ability to deliver multiple solutions on µm-scale ring sensors also facilitates in-channel functionalization of rings with different receptors, avoiding expensive micro-array spotters.

Co-integration of µm-scale MRRs with on-chip electronics on the same die will create a new path towards miniaturized photonic biosensors for PoC. In Chapter 5, we introduced a fully integrated electronic-photonic SoC for molecular sensing. We first provided an overview of the critical architectural features needed to enable key sensing capabilities and identified the main noise sources of the system. We then described the structure of the ring sensor in 45nm process and highlighted the active resonance tuning mechanism which eliminates the need for a tunable laser. The readout sensing circuitry was then analyzed and we discussed the design challenges to meet the noise requirements and support a wide input current Dynamic Range originating from the strong background photocurrent of the MRR. The system architecture was then presented, analyzing different photonic sensing schemes which rely on amplitude and phase detection. In order to suppress the inherent variabilities of rings due to environmental fluctuations, we demonstrated a differential readout scheme, comprised of sensing and reference ring structures. Finally, we described the packaging strategy to provide simultaneous electronic, photonic and fluidic coupling and presented the design methodology to develop this chip.

In Chapter 6, we demonstrated the experimental results of the monolithic EPSoC. We first characterized the electronic response of the on-chip receiver and determined the noise performance without any light signal. After establishing the functionality of electronic sensing interface, we evaluated the electronic-photonic performance. Results from different photonic sensing architectures were presented, detecting the amplitude and phase changes of the MRR's electric field. Additionally the functionality of the on-chip tuning controller locking the MRR was demonstrated by inducing ambient temperature changes. In this thesis, we presented for the first time using a monolithic electronic-photonic SoC real-time molecular kinetics. By detecting binding events of proteins such as streptavidin, anti-BSA and BSA and monitoring kinetics from conjugated large nanoparticles, we highlighted the versatility of our platform and paved the path towards highly miniaturized and fully integrated LoC

photonic sensors for PoC applications.

7.2 Improving the Limit of Detection

In this thesis, we demonstrate a first of its class monolithic electronic-photonic LoC. In this first generation SoC, we establish the label-free sensing capabilities of the platform, by demonstrating in real-time molecular kinetics of both proteins and nanoparticles mimicking viral particles. In order to further lower the LoD, future chip generations will aim to improve the sensitivity of the biosensing EPSoC at the platform, device, architectural and packaging levels. This can be accomplished by the following thrusts:

- First, the intrinsic sensitivity of the fully integrated process can be significantly increased by partially etching the SiO_2 BOX layer, resulting in an SNR enhancement of 7× [30]. This can be explained by the lower confinement of the optical mode as the BOX thickness decreases, resulting in stronger interactions between the evanescent field and the target molecules. An RIE etching process can be implemented in order to selectively etch the SiO_2-based BOX layer.

- In addition to optimizing the confinement of the optical mode, higher Q rings, previously shown in this platform, can enhance the photonic sensitivity by almost an order of magnitude. Combining the rings with RAMZI structures, we can lower the LoD by almost 2 orders of magnitude, leading to ultra-sensitive biosensing LoC systems

- By applying one of the phase modulation techniques, described in Section 2.4.3, the low frequency sensing signal induced by the slow molecular kinetics is modulated and therefore, the effect of flicker noise from the receiver front-end can be mitigated. This "chopping" scheme in the optical domain can replace upconversion of the sensing photocurrent in the electronic domain and therefore we can avoid any non-idealities from electronic chopping or correlated double sampling. Eliminating the effect of 1/f noise results in a white noise-dominated performance which can be improved by on-chip averaging allowed by the slow molecular kinetics.

- The fully differential readout scheme comprised of sensing and reference rings allows the suppression of ambient common mode errors induced by environmental fluctuations. However, fabrication errors between identical rings result in different ring sensitivities towards temperature fluctuations [69]. In order to precisely correct these temperature fluctuations, mK temperature sensors can be designed at close proximity to the ring cavities in order to monitor the micro-environment of each ring. Given the thermo-optic coefficient of rings and the output of the temperature sensor, the temperature induced resonant shift can be calculated and precisely subtracted from the overall ring response.

- Moving towards wafer-scale surface chemistry, advanced micro-array spotters can selectively functionalize simultaneously multiple rings. This ensures higher quality surface chemistry for multiple dies at once without the need for in-channel functionalization using microfluidics, which is limited to only ring-columns functionalization. By functionalizing each ring with a different receptor, the requirement for multi-channel fluidic packages can be significantly relaxed, since a single wide channel can now flow the testing solution to multiple rings, each specific to a different target analyte. This enables a uniform microfluidic environment by exposing the ring sensors to the same pressure variations induced by the syringe pump.

7.3 Moving Towards an Implantable Vision

Monitoring real-time physiologic and molecular tumor response to targeted molecular agents and radiation, within the complex in situ host environment - in effect a wireless biopsy - provides an unseen window into cancer biology, guiding optimal, personalized patient care. Building on the world's first monolithic electronic photonic LoC system, presented in this thesis, future research aims to develop a versatile platform for protein, and DNA sensing directly within the patient's tumor micro-environment. Our vision for a fully implantable, wireless, microfabricated electronic-photonic platform for real-time in vivo tumor monitoring is illustrated in Fig. 7.1.

The platform will provide label-free molecular response unveiling early indicators of tumor response. This is achieved using nanophotonic ring banks selectively coated with complementary antibodies, fully integrated with sensing circuitry. We will detect and explore the role of circulating tumor DNA (ctDNA) at the site of disease, dramatically increasing sensitivity while providing spatial localization for the source of DNA. Key to mitigating biofouling, enabling long term device use, is a releasable protective cap over each sensor block - allowing long-term sensing by revealing a new sensor block on demand. Made possible by ultrasound-based power and data transfer, and building on the unprecedented integration of circuits with photonics, these advances will unlock an entirely new paradigm of real-time response assessment, enabling effective application of novel therapeutics and immunotherapy, customized to patient's tumor biology.

The wireless biopsy platform, illustrated in Fig. 7.1, enables a small form-factor implant, directly embedded into a tumor and powered on demand, using clinically compatible ultrasound – as demonstrated in [70] to power neural implants – to perform a variety of sensing operations. The implant chip is flip-chip mounted on a piezocrystal block stacked on a micro supercapacitor, creating a single mm^3-scale monolithic implant. The power and commands are transmitted to the implant via ultrasound and the measurements are received through back-scattering, building on recent demonstrations [71,72]. The sensor elements are exposed to the environment via a backside-etch, functionalized and capped with an electrically disolvable membrane enabling controlled sensing over months to years. Integrating this platform into a monolithic mm^3 implant, we can provide large bursts of power necessary for periodic

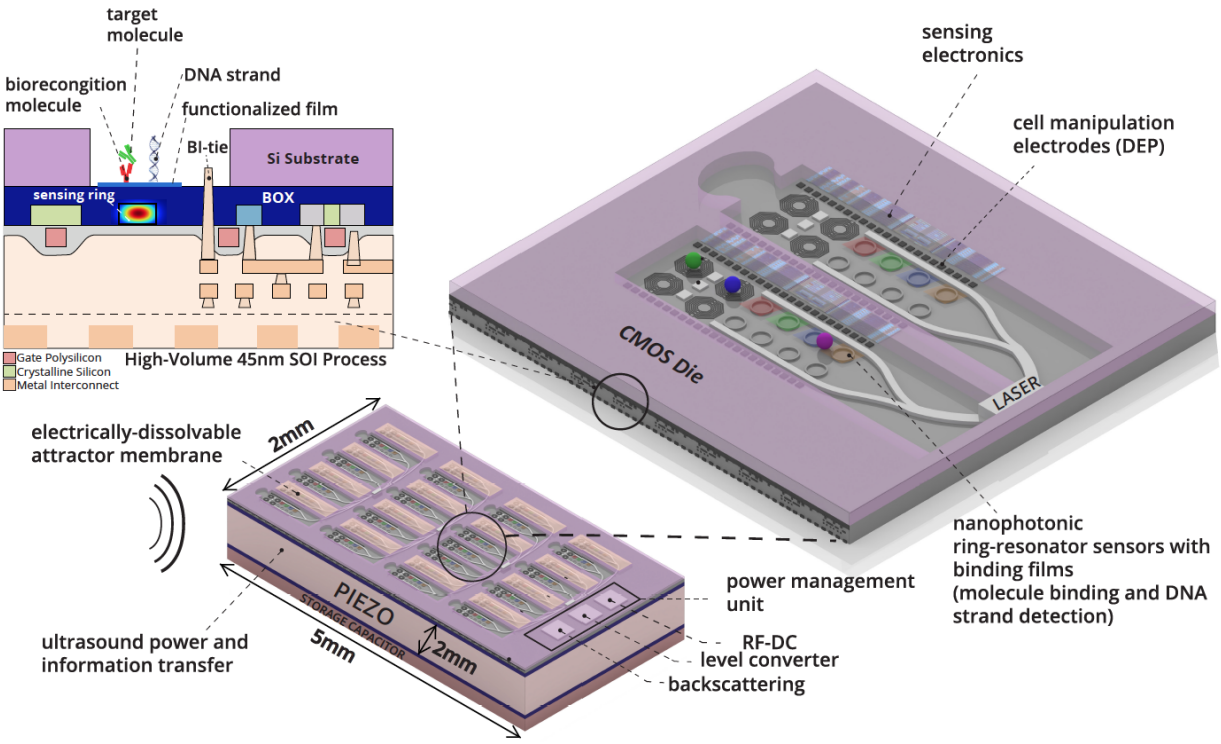

Figure 7.1: Wireless Biopsy Platform

laser and sensing electronics to measure arrays of proteins and circulating DNA at the tumor site. A releasable protective cap can be used to mitigate biofouling to enable chronic implantation and measurement.

Upon the activation command, the implant would dissolve the protective membrane over the selected sensing chamber, attracting cells through release of a trapped chemotactic agent. Once in the vicinity of the sensor, on-chip DEP (Dielectrophoresis) electrodes manipulate cells to the appropriate sites. The exposed surface allows intratumoral molecules and DNA to diffuse to the functionalized nanophotonic sites for testing of molecular responses.

The operation of the platform implant is constrained by several factors: allowable thermal dissipation limit in tissue, power-delivery limit, high on-chip voltage requirements for DEP, laser operation, energy-storage, power consumption of various subsystems, and measurement/excitation times required for various sensing and actuation modalities. Operating at ≈2% of the FDA limit of 7.2mW/mm^2, the implant's piezocrystal block with area of 5mm x 2mm will be able to harvest up to ≈1.5mW of power from ultrasound. Assuming storage of 60µJ on a 60µF micro supercapacitor, well within the technological limits of 3mF/mm^2 [73], this will adequately address our sensors. With a 2.5% duty cycle, molecular sensing snapshots of 1ms can be performed at 40ms intervals allowing real-time kinetics to be observed well within the tissue thermal limit of 0.4mW/mm^2 [74]. Further circuit optimization will re-

duce the density below 0.04mW/mm^2, thus paving the path towards low power implantable photonic LoC sensors for real-time in vivo monitoring.

Bibliography

[1] N. Bhalla, Y. Pan, Z. Yang, and A. F. Payam, "Opportunities and challenges for biosensors and nanoscale analytical tools for pandemics: Covid-19," *ACS nano*, vol. 14, no. 7, pp. 7783–7807, 2020.

[2] E. Morales-Narváez and C. Dincer, "The impact of biosensing in a pandemic outbreak: Covid-19," *Biosensors and Bioelectronics*, vol. 163, p. 112274, 2020.

[3] M. Musiani, S. Venturoli, G. Gallinella, and M. Zerbini, "Qualitative PCR-ELISA protocol for the detection and typing of viral genomes," *Nat Protoc*, vol. 2, no. 10, pp. 2502–2510, 2007.

[4] C. Klumpp-Thomas, H. Kalish, M. Drew, S. Hunsberger, K. Snead, M. P. Fay, J. Mehalko, A. Shunmugavel, V. Wall, P. Frank *et al.*, "Standardization of elisa protocols for serosurveys of the sars-cov-2 pandemic using clinical and at-home blood sampling," *Nature communications*, vol. 12, no. 1, pp. 1–13, 2021.

[5] B. Sepúlveda, J. S. Del Rio, M. Moreno, F. J. Blanco, K. Mayora, C. Domínguez, and L. M. Lechuga, "Optical biosensor microsystems based on the integration of highly sensitive mach–zehnder interferometer devices," *Journal of Optics A: Pure and Applied Optics*, vol. 8, no. 7, p. S561, 2006.

[6] S. Dante, D. Duval, B. Sepúlveda, A. B. González-Guerrero, J. R. Sendra, and L. M. Lechuga, "All-optical phase modulation for integrated interferometric biosensors," *Optics express*, vol. 20, no. 7, pp. 7195–7205, 2012.

[7] T. Chalyan, R. Guider, L. Pasquardini, M. Zanetti, F. Falke, E. Schreuder, R. G. Heideman, C. Pederzolli, and L. Pavesi, "Asymmetric mach–zehnder interferometer based biosensors for aflatoxin m1 detection," *Biosensors*, vol. 6, no. 1, p. 1, 2016.

[8] D. Martens and P. Bienstman, "Comparison between vernier-cascade and mzi as transducer for biosensing with on-chip spectral filter," *Nanophotonics*, vol. 6, no. 4, pp. 703–712, 2017.

[9] Q. Liu, X. Tu, K. W. Kim, J. S. Kee, Y. Shin, K. Han, Y.-J. Yoon, G.-Q. Lo, and M. K. Park, "Highly sensitive mach–zehnder interferometer biosensor based on silicon nitride slot waveguide," *Sensors and Actuators B: Chemical*, vol. 188, pp. 681–688, 2013.

[10] J. Leuermann, A. Fernández-Gavela, A. Torres-Cubillo, S. Postigo, A. Sánchez-Postigo, L. M. Lechuga, R. Halir, and Í. Molina-Fernández, "Optimizing the limit of detection of waveguide-based interferometric biosensor devices," *Sensors*, vol. 19, no. 17, p. 3671, 2019.

[11] M. Iqbal, M. A. Gleeson, B. Spaugh, F. Tybor, W. G. Gunn, M. Hochberg, T. Baehr-Jones, R. C. Bailey, and L. C. Gunn, "Label-free biosensor arrays based on silicon ring resonators and high-speed optical scanning instrumentation," *IEEE Journal of selected topics in quantum electronics*, vol. 16, no. 3, pp. 654–661, 2010.

[12] A. L. Washburn, L. C. Gunn, and R. C. Bailey, "Label-free quantitation of a cancer biomarker in complex media using silicon photonic microring resonators," *Analytical chemistry*, vol. 81, no. 22, pp. 9499–9506, 2009.

[13] H. Yan, L. Huang, X. Xu, S. Chakravarty, N. Tang, H. Tian, and R. T. Chen, "Unique surface sensing property and enhanced sensitivity in microring resonator biosensors based on subwavelength grating waveguides," *Optics express*, vol. 24, no. 26, pp. 29 724–29 733, 2016.

[14] J. Flueckiger, S. Schmidt, V. Donzella, A. Sherwali, D. M. Ratner, L. Chrostowski, and K. C. Cheung, "Sub-wavelength grating for enhanced ring resonator biosensor," *Optics express*, vol. 24, no. 14, pp. 15 672–15 686, 2016.

[15] S. Mudumba, S. de Alba, R. Romero, C. Cherwien, A. Wu, J. Wang, M. A. Gleeson, M. Iqbal, and R. W. Burlingame, "Photonic ring resonance is a versatile platform for performing multiplex immunoassays in real time," *Journal of immunological methods*, vol. 448, pp. 34–43, 2017.

[16] A. J. Qavi and R. C. Bailey, "Multiplexed detection and label-free quantitation of microRNAs using arrays of silicon photonic microring resonators," *Angew Chem Int Ed Engl*, vol. 49, no. 27, pp. 4608–4611, Jun 2010.

[17] P. Steglich, M. Hülsemann, B. Dietzel, and A. Mai, "Optical biosensors based on silicon-on-insulator ring resonators: A review," *Molecules*, vol. 24, no. 3, p. 519, 2019.

[18] E. Luan, H. Shoman, D. M. Ratner, K. C. Cheung, and L. Chrostowski, "Silicon photonic biosensors using label-free detection," *Sensors*, vol. 18, no. 10, p. 3519, 2018.

[19] A. Fernández Gavela, D. Grajales García, J. C. Ramirez, and L. M. Lechuga, "Last advances in silicon-based optical biosensors," *sensors*, vol. 16, no. 3, p. 285, 2016.

[20] A. Densmore, D.-X. Xu, P. Waldron, S. Janz, P. Cheben, J. Lapointe, A. Delâge, B. Lamontagne, J. Schmid, and E. Post, "A silicon-on-insulator photonic wire based evanescent field sensor," *IEEE Photonics Technology Letters*, vol. 18, no. 23, pp. 2520–2522, 2006.

[21] S. Janz, A. Densmore, D. Xu, W. Sinclair, J. Schmid, R. Ma, M. Vachon, J. Lapointe, A. Delâge, E. Post *et al.*, "Silicon photonic wire evanescent field sensors: From sensor to biochip array," in *2009 6th IEEE International Conference on Group IV Photonics*. IEEE, 2009, pp. 89–91.

[22] X. Wang, S. Grist, J. Flueckiger, N. A. Jaeger, and L. Chrostowski, "Silicon photonic slot waveguide bragg gratings and resonators," *Optics express*, vol. 21, no. 16, pp. 19 029–19 039, 2013.

[23] P. Ramirez-Priego, D. Martens, A. A. Elamin, P. Soetaert, W. Van Roy, R. Vos, B. Anton, R. Bockstaele, H. Becker, M. Singh *et al.*, "Label-free and real-time detection of tuberculosis in human urine samples using a nanophotonic point-of-care platform," *ACS sensors*, vol. 3, no. 10, pp. 2079–2086, 2018.

[24] J. Leuermann, V. Stamenkovic, P. Ramirez-Priego, A. Sánchez-Postigo, A. Fernández-Gavela, C. A. Chapman, R. C. Bailey, L. M. Lechuga, E. Perez-Inestrosa, D. Collado *et al.*, "Coherent silicon photonic interferometric biosensor with an inexpensive laser source for sensitive label-free immunoassays," *Optics Letters*, vol. 45, no. 24, pp. 6595–6598, 2020.

[25] W. Bogaerts, P. De Heyn, T. Van Vaerenbergh, K. De Vos, S. Kumar Selvaraja, T. Claes, P. Dumon, P. Bienstman, D. Van Thourhout, and R. Baets, "Silicon microring resonators," *Laser & Photonics Reviews*, vol. 6, no. 1, pp. 47–73, 2012.

[26] J. Zhu, S. K. Ozdemir, Y.-F. Xiao, L. Li, L. He, D.-R. Chen, and L. Yang, "On-chip single nanoparticle detection and sizing by mode splitting in an ultrahigh-q microresonator," *Nature photonics*, vol. 4, no. 1, p. 46, 2010.

[27] L. Huang, H. Yan, X. Xu, S. Chakravarty, N. Tang, H. Tian, and R. T. Chen, "Improving the detection limit for on-chip photonic sensors based on subwavelength grating racetrack resonators," *Optics express*, vol. 25, no. 9, pp. 10 527–10 535, 2017.

[28] E. Luan, H. Yun, L. Laplatine, Y. Dattner, D. M. Ratner, K. C. Cheung, and L. Chrostowski, "Enhanced sensitivity of subwavelength multibox waveguide microring resonator label-free biosensors," *IEEE Journal of Selected Topics in Quantum Electronics*, vol. 25, no. 3, pp. 1–11, 2018.

[29] K. De Vos, "Label-free silicon photonics biosensor platform withmicroring resonators." Ph.D. dissertation, Ghent University, 2010.

[30] C. Adamopoulos, A. Gharia, A. Niknejad, M. Anwar, and V. Stojanović, "Electronic-photonic platform for label-free biophotonic sensing in advanced zero-change cmos-soi process," in *CLEO: QELS_Fundamental Science*. Optical Society of America, 2019, pp. JW2A–81.

[31] D. M. Gill, S. S. Patel, M. Rasras, K.-Y. Tu, A. E. White, Y.-K. Chen, A. Pomerene, D. Carothers, R. L. Kamocsai, C. M. Hill *et al.*, "Cmos-compatible si-ring-assisted mach–zehnder interferometer with internal bandwidth equalization," *IEEE Journal of Selected Topics in Quantum Electronics*, vol. 16, no. 1, pp. 45–52, 2009.

[32] N. Mehta, S. Lin, B. Yin, S. Moazeni, and V. Stojanović, "A laser-forwarded coherent transceiver in 45-nm soi cmos using monolithic microring resonators," *IEEE Journal of Solid-State Circuits*, vol. 55, no. 4, pp. 1096–1107, 2020.

[33] M. Terrel, M. J. Digonnet, and S. Fan, "Ring-coupled mach-zehnder interferometer optimized for sensing," *Applied optics*, vol. 48, no. 26, pp. 4874–4879, 2009.

[34] R. Soref and B. Bennett, "Electrooptical effects in silicon," *IEEE journal of quantum electronics*, vol. 23, no. 1, pp. 123–129, 1987.

[35] C. Sun, M. T. Wade, Y. Lee, J. S. Orcutt, L. Alloatti, M. S. Georgas, A. S. Waterman, J. M. Shainline, R. R. Avizienis, S. Lin *et al.*, "Single-chip microprocessor that communicates directly using light," *Nature*, vol. 528, no. 7583, pp. 534–538, 2015.

[36] A. L. Washburn, M. S. Luchansky, A. L. Bowman, and R. C. Bailey, "Quantitative, label-free detection of five protein biomarkers using multiplexed arrays of silicon photonic microring resonators," *Analytical chemistry*, vol. 82, no. 1, pp. 69–72, 2010.

[37] A. L. Washburn, L. C. Gunn, and R. C. Bailey, "Label-free quantitation of a cancer biomarker in complex media using silicon photonic microring resonators," *Analytical chemistry*, vol. 81, no. 22, pp. 9499–9506, 2009.

[38] M. Iqbal, M. A. Gleeson, B. Spaugh, F. Tybor, W. G. Gunn, M. Hochberg, T. Baehr-Jones, R. C. Bailey, and L. C. Gunn, "Label-free biosensor arrays based on silicon ring resonators and high-speed optical scanning instrumentation," *IEEE Journal of selected topics in quantum electronics*, vol. 16, no. 3, pp. 654–661, 2010.

[39] M. S. Luchansky, A. L. Washburn, M. S. McClellan, and R. C. Bailey, "Sensitive on-chip detection of a protein biomarker in human serum and plasma over an extended dynamic range using silicon photonic microring resonators and sub-micron beads," *Lab on a Chip*, vol. 11, no. 12, pp. 2042–2044, 2011.

[40] A. J. Qavi, J. T. Kindt, M. A. Gleeson, and R. C. Bailey, "Anti-dna: Rna antibodies and silicon photonic microring resonators: increased sensitivity for multiplexed microrna detection," *Analytical chemistry*, vol. 83, no. 15, pp. 5949–5956, 2011.

[41] J. Flueckiger, S. Schmidt, V. Donzella, A. Sherwali, D. M. Ratner, L. Chrostowski, and K. C. Cheung, "Sub-wavelength grating for enhanced ring resonator biosensor," *Optics express*, vol. 24, no. 14, pp. 15 672–15 686, 2016.

[42] H. Yan, L. Huang, X. Xu, S. Chakravarty, N. Tang, H. Tian, and R. T. Chen, "Unique surface sensing property and enhanced sensitivity in microring resonator biosensors based on subwavelength grating waveguides," *Optics express*, vol. 24, no. 26, pp. 29 724–29 733, 2016.

[43] T. Claes, J. G. Molera, K. De Vos, E. Schacht, R. Baets, and P. Bienstman, "Label-free biosensing with a slot-waveguide-based ring resonator in silicon on insulator," *IEEE Photonics journal*, vol. 1, no. 3, pp. 197–204, 2009.

[44] K. De Vos, J. Girones, T. Claes, Y. De Koninck, S. Popelka, E. Schacht, R. Baets, and P. Bienstman, "Multiplexed antibody detection with an array of silicon-on-insulator microring resonators," *IEEE Photonics Journal*, vol. 1, no. 4, pp. 225–235, 2009.

[45] S. M. Khan, A. Gumus, J. M. Nassar, and M. M. Hussain, "Cmos enabled microfluidic systems for healthcare based applications," *Advanced Materials*, vol. 30, no. 16, p. 1705759, 2018.

[46] M. Muluneh and D. Issadore, "A multi-scale pdms fabrication strategy to bridge the size mismatch between integrated circuits and microfluidics," *Lab on a Chip*, vol. 14, no. 23, pp. 4552–4558, 2014.

[47] H. Wu, T. W. Odom, D. T. Chiu, and G. M. Whitesides, "Fabrication of complex three-dimensional microchannel systems in pdms," *Journal of the American Chemical Society*, vol. 125, no. 2, pp. 554–559, 2003.

[48] G. Comina, A. Suska, and D. Filippini, "Pdms lab-on-a-chip fabrication using 3d printed templates," *Lab on a Chip*, vol. 14, no. 2, pp. 424–430, 2014.

[49] D. Qin, Y. Xia, and G. M. Whitesides, "Soft lithography for micro-and nanoscale patterning," *Nature protocols*, vol. 5, no. 3, p. 491, 2010.

[50] M. Zhang, J. Wu, L. Wang, K. Xiao, and W. Wen, "A simple method for fabricating multi-layer pdms structures for 3d microfluidic chips," *Lab on a Chip*, vol. 10, no. 9, pp. 1199–1203, 2010.

[51] J. Friend and L. Yeo, "Fabrication of microfluidic devices using polydimethylsiloxane," *Biomicrofluidics*, vol. 4, no. 2, p. 026502, 2010.

[52] S. Bhattacharya, A. Datta, J. M. Berg, and S. Gangopadhyay, "Studies on surface wettability of poly (dimethyl) siloxane (pdms) and glass under oxygen-plasma treatment and correlation with bond strength," *Journal of microelectromechanical systems*, vol. 14, no. 3, pp. 590–597, 2005.

[53] C. Adamopoulos, P. Zarkos, S. Buchbinder, P. Bhargava, A. Niknejad, M. Anwar, and V. Stojanović, "Lab-on-chip for everyone: Introducing an electronic-photonic platform

for multiparametric biosensing using standard cmos processes," *IEEE Open Journal of the Solid-State Circuits Society*, 2021.

[54] M. Wade, E. Andersson, and S. Artalan, "An error-free 1 tbps wdm optical i/o chiplet and multi-wavelength multi-port laser," in *OFC*. Optical Society of America, 2021, p. in press.

[55] P. A. Morton and M. J. Morton, "High-power, ultra-low noise hybrid lasers for microwave photonics and optical sensing," *Journal of Lightwave Technology*, vol. 36, no. 21, pp. 5048–5057, 2018.

[56] N. Mehta, S. Buchbinder, and V. Stojanović, "Design and characterization of monolithic microring resonator based photodetector in 45nm soi cmos," in *ESSDERC 2019-49th European Solid-State Device Research Conference (ESSDERC)*. IEEE, 2019, pp. 206–209.

[57] C. Sun, M. Wade, M. Georgas, S. Lin, L. Alloatti, B. Moss, R. Kumar, A. H. Atabaki, F. Pavanello, J. M. Shainline, J. S. Orcutt, R. J. Ram, M. Popović, and V. Stojanović, "A 45 nm cmos-soi monolithic photonics platform with bit-statistics-based resonant microring thermal tuning," *IEEE Journal of Solid-State Circuits*, vol. 51, no. 4, pp. 893–907, 2016.

[58] J. S. Orcutt, B. Moss, C. Sun, J. Leu, M. Georgas, J. Shainline, E. Zgraggen, H. Li, J. Sun, M. Weaver *et al.*, "Open foundry platform for high-performance electronic-photonic integration," *Optics express*, vol. 20, no. 11, pp. 12 222–12 232, 2012.

[59] P. Zarkos, O. Hsu, and V. Stojanović, "Ring resonator based ultrasound detection in a zero-change advanced cmos-soi process," in *CLEO: QELS_Fundamental Science*. Optical Society of America, 2019, pp. JW2A–78.

[60] M. Muluneh and D. Issadore, "A multi-scale pdms fabrication strategy to bridge the size mismatch between integrated circuits and microfluidics," *Lab on a Chip*, vol. 14, no. 23, pp. 4552–4558, 2014.

[61] C. Adamopoulos, A. Gharia, A. Niknejad, V. Stojanović, and M. Anwar, "Microfluidic packaging integration with electronic-photonic biosensors using 3d printed transfer molding," *Biosensors*, vol. 10, no. 11, p. 177, 2020.

[62] J. Crossley, A. Puggelli, H.-P. Le, B. Yang, R. Nancollas, K. Jung, L. Kong, N. Narevsky, Y. Lu, N. Sutardja *et al.*, "Bag: A designer-oriented integrated framework for the development of ams circuit generators," in *2013 IEEE/ACM International Conference on Computer-Aided Design (ICCAD)*. IEEE, 2013, pp. 74–81.

[63] C. Adamopoulos, S. Buchbinder, P. Zarkos, P. Bhargava, A. Gharia, A. Ninkejad, M. Anwar, and V. Stojanovic, "Fully integrated electronic-photonic sensor for label-free refractive index sensing in advanced zero-change cmos-soi process," in *2021 IEEE Custom Integrated Circuits Conference (CICC)*. IEEE, 2021, pp. 1–2.

[64] C. Adamopoulos, S. Buchbinder, P. Zarkos, P. Bhargava, A. Gharia, A. Niknejad, M. Anwar, and V. Stojanović, "Fully integrated electronic–photonic biosensor for label-free real-time molecular sensing in advanced zero-change cmos-soi process," *IEEE Solid-State Circuits Letters*, vol. 4, pp. 198–201, 2021.

[65] N. B. Arnfinnsdottir, C. A. Chapman, R. C. Bailey, A. Aksnes, and B. T. Stokke, "Impact of silanization parameters and antibody immobilization strategy on binding capacity of photonic ring resonators," *Sensors*, vol. 20, no. 11, p. 3163, 2020.

[66] M. S. Luchansky, A. L. Washburn, M. S. McClellan, and R. C. Bailey, "Sensitive on-chip detection of a protein biomarker in human serum and plasma over an extended dynamic range using silicon photonic microring resonators and sub-micron beads," *Lab on a Chip*, vol. 11, no. 12, pp. 2042–2044, 2011.

[67] C. Adamopoulos, S. Buchbinder, P. Zarkos, P. Bhargava, A. Gharia, A. Niknejad, and V. Stojanović, "Fully integrated electronic-photonic biosensor for label-free molecular sensing in advanced zero-change cmos-soi process," in *CLEO: Science and Innovations*. Optical Society of America, 2021, p. JM4D.3.

[68] M. Kozminsky, T. Carey, and L. L. Sohn, "Dna-directed patterning for versatile validation and characterization of a lipid-based nanoparticle model of sars-cov-2," 2021.

[69] P. F. Popescu, "An optofluidic ring resonator platform for rapid and robust sensing," Ph.D. dissertation, California Institute of Technology, 2017.

[70] D. Seo, R. M. Neely, K. Shen, U. Singhal, E. Alon, J. M. Rabaey, J. M. Carmena, and M. M. Maharbiz, "Wireless recording in the peripheral nervous system with ultrasonic neural dust," *Neuron*, vol. 91, no. 3, pp. 529–539, 2016.

[71] M. M. Maharbiz, "Recent developments in wireless recording from the nervous system with ultrasonic neural dust (conference presentation)," in *Micro-and Nanotechnology Sensors, Systems, and Applications IX*, vol. 10194. International Society for Optics and Photonics, 2017, p. 101942F.

[72] M. J. Weber, Y. Yoshihara, A. Sawaby, J. Charthad, T. C. Chang, and A. Arbabian, "A miniaturized single-transducer implantable pressure sensor with time-multiplexed ultrasonic data and power links," *IEEE Journal of Solid-State Circuits*, vol. 53, no. 4, pp. 1089–1101, 2018.

[73] C. Shen, S. Xu, Y. Xie, M. Sanghadasa, X. Wang, and L. Lin, "A review of on-chip micro supercapacitors for integrated self-powering systems," *Journal of Microelectromechanical Systems*, vol. 26, no. 5, pp. 949–965, 2017.

[74] P. D. Wolf and W. Reichert, "Thermal considerations for the design of an implanted cortical brain–machine interface (bmi)," *Indwelling Neural Implants: Strategies for Contending with the In Vivo Environment*, pp. 33–38, 2008.